

AD-A063 953

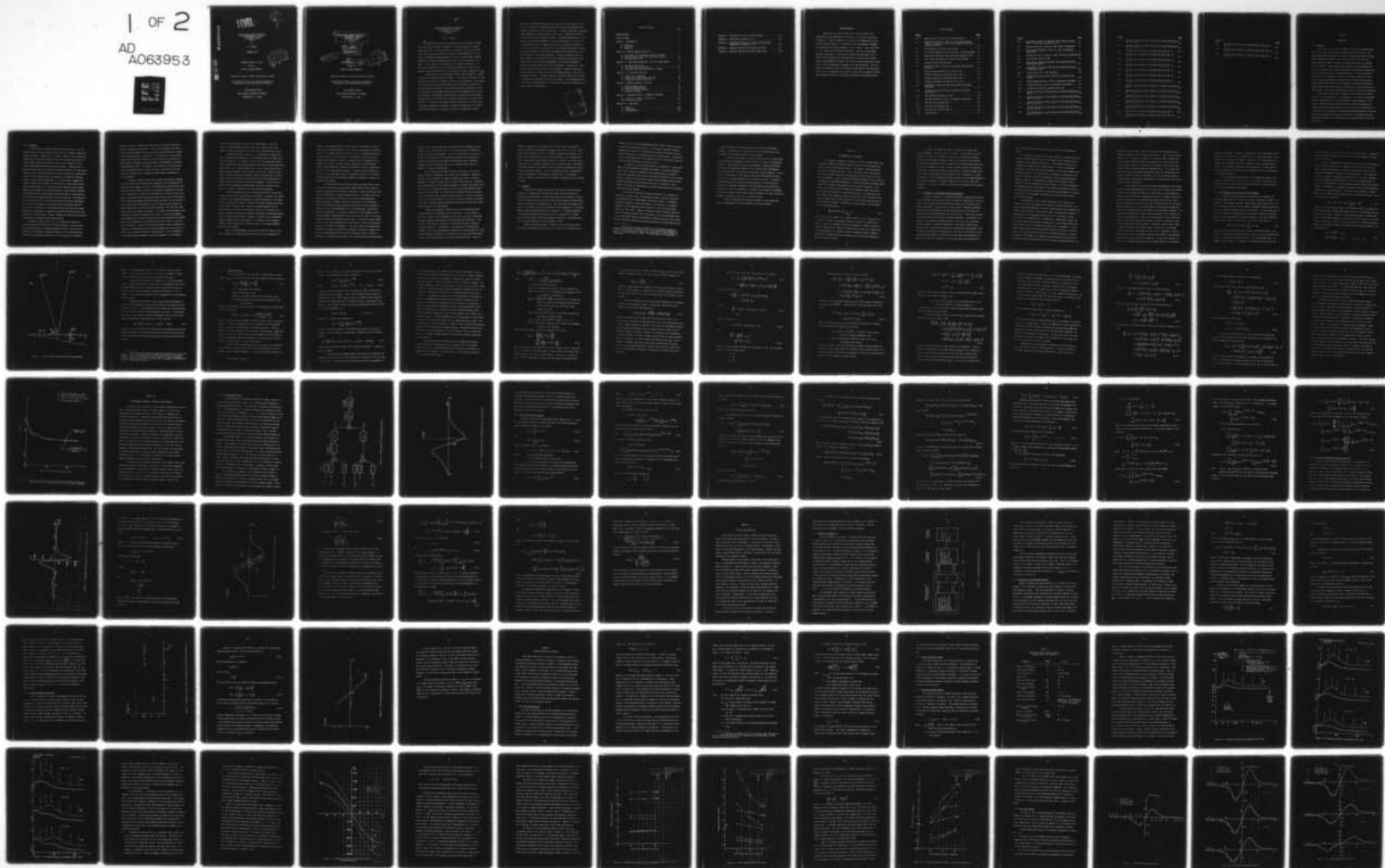
CATHOLIC UNIV OF AMERICA WASHINGTON D C ACOUSTICS GROUP F/G 17/1
PASSIVE SONAR BEARING ESTIMATION IN THE PRESENCE OF HIGHLY ANIS--ETC(U)
DEC 78 L R HOWELL N00014-77-C-0530

NL

UNCLASSIFIED

1 OF 2

AD
A063953



AD A063953

LEVEL

C
SC

PASSIVE SONAR BEARING ESTIMATION
IN THE PRESENCE OF HIGHLY
ANISOTROPIC NOISE
FIELDS

by

L. R. HOWELL

DECEMBER 1978

CONTRACT N00014-77-C-0530

CODE 431

OFFICE OF NAVAL RESEARCH

DDC
RECEIVED
JAN 30 1979
C

DDC FILE COPY

Approved for public release; distribution unlimited

Reproduction in whole or in part is permitted for
any purpose of the United States Government

THE ACOUSTICS GROUP
THE CATHOLIC UNIVERSITY OF AMERICA
WASHINGTON, D.C. 20064

79 01 30 085

6 PASSIVE SONAR BEARING ESTIMATION
IN THE PRESENCE OF HIGHLY
ANISOTROPIC NOISE
FIELDS

by

10 L. R. HOWELL

11 DECEMBER 1978

12 178 P.

15
CONTRACT N00014-77-C-0530
CODE 431



OFFICE OF NAVAL RESEARCH

Approved for public release; distribution unlimited

Reproduction in whole or in part is permitted for
any purpose of the United States Government

408 214

THE ACOUSTICS GROUP

THE CATHOLIC UNIVERSITY OF AMERICA

WASHINGTON, D.C. 20064

408 214

elt

-A-

PASSIVE SONAR BEARING ESTIMATION
IN THE PRESENCE OF HIGHLY
ANISOTROPIC NOISE
FIELDS

By L. R. Howell

↓ The problem of sonar bearing estimation in the presence of highly anisotropic noise fields is examined for both conventional and optimal array processors. In some situations, the presence of one or more (high level) interfering noise source precludes bearing estimation by conventional, non-adaptive array processors. However, in some target tracking problems (e.g. TMA) the performance loss due to noise anisotropy is not total. In the context of such problems, the effects of multiple, unidirectional interferers on the conventional, split-beam tracker and the maximum likelihood estimator are investigated for linear receiving arrays. ↗

The performance of the maximum likelihood (ML) estimator is characterized by the Cramer-Rao variance bound. A new result is obtained for this bound which is valid for arbitrary spatial noise distributions. Expressions for the split-beam tracker (SBT) output mean and variance are derived for the noise model of interest. From these expressions, approximate theoretical measures of the bearing estimation bias and standard deviation errors are developed. Further statistical measures of the SBT bias and standard deviation errors are obtained from a digital simulation of the split-beam tracker. The effects of the degree of noise anisotropy on the ML and SBT performance measures are assessed for parametric variations in the anisotropic noise component. The numerical results illustrate the complex

behavior of random and bias errors with variations in the number, separation, and position of interfering noise sources when such interferers are neither coincident nor totally resolvable. As might be expected, anisotropic noise components at remote target-to-interference separations are shown to have little effect on either estimator. For mean separations less than about two resolution beamwidths, the standard deviation of error for the ML and SBT processors is primarily dependent on the spatial distribution of interference power in the vicinity of one beamwidth separation from the true source bearing. The relative degradation of the SBT processor over the ML estimator is similarly dependent. Multiple interferers bias the SBT estimates in the direction of the mean interference bearing with the peak bias error occurring for approximately one resolution beamwidth separation between target and closest interference. Variations in signal-to-noise ratio and array size are also examined. Multiple interfering noise sources do not affect the functional SNR dependence of the selected performance metrics. A dramatic decrease in SBT bias error for all levels of anisotropy is observed as array size increases. The standard deviation of error also decreases with array size with the rate of decrease lower for larger numbers of interferers.

ACCESSION for	
NTIS	WFO Section <input checked="" type="checkbox"/>
DOC	ELW Section <input type="checkbox"/>
UNCLASSIFIED	
JAN 1 1984	
BY	
DISTRIBUTION/AVAILABILITY CODES	
SPECIAL	
A	

TABLE OF CONTENTS

	<u>Page</u>
ACKNOWLEDGEMENTS	iv
LIST OF FIGURES	v
CHAPTER I - INTRODUCTION	1
1.1 Objective	1
1.2 Background	2
1.3 Approach	7
CHAPTER II - OPTIMUM BEARING ESTIMATION	10
2.1 Performance of the Maximum Likelihood Estimator	11
2.2 Received Signal, Noise and Interference Models	14
2.3 The Cramer-Rao Bound	18
CHAPTER III - SUB-OPTIMUM ESTIMATION: THE SPLIT-BEAM TRACKER	31
3.1 The Split-Beam Tracker	32
3.2 SBT Output Mean and Variance	35
3.3 Theoretical SBT Bearing Estimation Variance	43
CHAPTER IV - DIGITAL SBT SIMULATION	51
4.1 Digital SBT Simulation	52
4.2 Generation of Input Random Deviates	54
4.3 Simulated Estimation Algorithm	58
CHAPTER V - NUMERICAL RESULTS - BASELINE	63
5.1 SBT Performance Metrics	63
5.2 Baseline Parameter Values	67
5.3 Standard Deviation Results	67
5.4 Bias Error Results	82
CHAPTER VI - NUMERICAL RESULTS - PARAMETER EXTENSIONS	88
6.1 Extension of Signal-to-Noise Ratio	88
6.2 Extended Array Size	100
CHAPTER VII - CONCLUSIONS	115
7.1 Summary	115
7.2 Conclusions	118
7.3 Recommendations	120

APPENDIX A - DERIVATION OF THE LOG-LIKELIHOOD RATIO	123
APPENDIX B - DERIVATION OF EQUATION (2-21)	131
APPENDIX C - DERIVATION OF CLOSED FORM EXPRESSION FOR DOUBLE SUMMATIONS IN EQUATION (4-28)	134
APPENDIX D - NUMERICAL RESULTS FOR EXTENDED SNR VALUES	137
APPENDIX E - NUMERICAL RESULTS FOR EXTENDED ARRAY SIZES	153

ACKNOWLEDGEMENTS

This report will also form the basis for the author's Ph.D dissertation to be submitted to the faculty of the Catholic University of America. I wish to thank Mr. C. M. Bennett for suggesting the topic of this research and Dr. F. A. Andrews for his encouragement throughout the research and the entire graduate course of study. I must also thank Dr. Y. C. Whang and the Catholic University of America for providing financial assistance. I would like to express my appreciation to the Office of Naval Research for the opportunity to conduct this research under contract N00014-77-C-0530. Mrs. Carolyn Turner deserves much credit for her skill and patience in preparing the final manuscript. My wife, Sarah, also deserves credit for typing the rough draft of this manuscript. Most of all, I am grateful for her moral support and the numerous personal and professional sacrifices she has made throughout my graduate career.

LIST OF FIGURES

<u>Figure</u>	<u>Page</u>
2.1	Signal, Noise, Interference and Array Geometry 16
2.2	Comparative Behavior of Equation (2-30) and MacDonald's Graphical Presentation [18] of the Cramer-Rao Bound for a Single Interferer 30
3.1	Block Diagram of the Split-Beam Tracker 33
3.2	Functional Dependence of Mean SBT Output on Steering Angle . 34
3.3	Approximate Theoretical Mean SBT Output (Equation 3-22) . . 44
3.4	Linear Mean SBT Output and Constant Variance Model 46
4.1	Frequency Domain SBT Simulation 53
4.2	Normalized Signal, Noise and Interference Power Spectral Densities 59
4.3	Discrete Bearing Estimation by LSE Line Fit 61
5.1	Standard Deviation of Estimation Error, $MM = 1$ 70
5.2	Standard Deviation of Estimation Error, $MM = 2$ 71
5.3	Standard Deviation of Estimation Error, $MM = 4$ 72
5.4	Approximate, Theoretical SBT Output Mean and Standard Deviation 75
5.5	Standard Deviation of Error for Remotely Positioned Interferers 78
5.6	Peak Standard Deviation of Error 79
5.7	Standard Deviation of Error - Coincident Interference . . . 81
5.8	SBT Bias Error Results, $MM = 1$ 83
5.9	SBT Bias Error Results, $MM = 2$ 84
5.10	SBT Bias Error Results, $MM = 4$ 85
5.11	Peak SBT Bias 87

<u>Figure</u>		<u>Page</u>
6.1	Approximate, Theoretical SBT Mean and Standard Deviation; SNR = 0.5 with Four Interferers at 76°	91
6.2	Standard Deviation of Error vs. SNR; Remote Interference . .	94
6.3	Peak Standard Deviation of Error vs. SNR; Intermediate Separations	97
6.4	Standard Deviation of Error vs. SNR; Coincident Interference	98
6.5	Peak SBT Bias Error vs. SNR	99
6.6	Approximate, Theoretical SBT Mean and Standard Deviation; 20 Hydrophone Array	101
6.7	Approximate, Theoretical SBT Mean and Standard Deviation; 40 Hydrophone Array	102
6.8	Computational Costs - SBT Simulation	104
6.9	Standard Deviation of Error; Remotely Positioned Inter- ference	109
6.10	Peak Standard Deviation of Error; Intermediate Separation	111
6.11	Standard Deviation of Error; Coincident Interference . . .	113
6.12	SBT Bias Error Metrics; Absolute Peak Value	114
D.1	Standard Deviation of Error Results for Extended SNR Values; MM = 1	139
D.2	Standard Deviation of Error Results for Extended SNR Values; MM = 2, $\Delta\theta = 3^\circ$	140
D.3	Standard Deviation of Error Results for Extended SNR Values; MM = 2, $\Delta\theta = 6^\circ$	141
D.4	Standard Deviation of Error Results for Extended SNR Values; MM = 2, $\Delta\theta = 9^\circ$	142
D.5	Standard Deviation of Error Results for Extended SNR Values; MM = 4, $\Delta\theta = 3^\circ$	143

<u>Figure</u>	<u>Page</u>
D.6	Standard Deviation of Error Results for Extended SNR Values; MM = 4, $\Delta\theta = 6^\circ$144
D.7	Standard Deviation of Error Results for Extended SNR Values; MM = 4, $\Delta\theta = 9^\circ$145
D.8	SBT Bias Error Results for Extended SNR Values; MM = 1 . . .146
D.9	SBT Bias Error Results for Extended SNR Values; MM = 2, $\Delta\theta = 3^\circ$147
D.10	SBT Bias Error Results for Extended SNR Values; MM = 2, $\Delta\theta = 6^\circ$148
D.11	SBT Bias Error Results for Extended SNR Values; MM = 2, $\Delta\theta = 9^\circ$149
D.12	SBT Bias Error Results for Extended SNR Values; MM = 4, $\Delta\theta = 3^\circ$150
D.13	SBT Bias Error Results for Extended SNR Values; MM = 4, $\Delta\theta = 6^\circ$151
D.14	SBT Bias Error Results for Extended SNR Values; MM = 4, $\Delta\theta = 9^\circ$152
E.1	Standard Deviation of Error Results for Extended Array Sizes; MM = 1155
E.2	Standard Deviation of Error Results for Extended Array Sizes; MM = 2, $\Delta\theta = 3^\circ$156
E.3	Standard Deviation of Error Results for Extended Array Sizes; MM = 2, $\Delta\theta = 6^\circ$157
E.4	Standard Deviation of Error Results for Extended Array Sizes; MM = 4, $\Delta\theta = 3^\circ$158
E.5	Standard Deviation of Error Results for Extended Array Sizes; MM = 4, $\Delta\theta = 6^\circ$159
E.6	SBT Bias Error Results for Extended Array Sizes; MM = 1 . .160
E.7	SBT Bias Error Results for Extended Array Sizes; MM = 2, $\Delta\theta = 3^\circ$161

<u>Figure</u>		<u>Page</u>
E.8	SBT Bias Error Results for Extended Array Sizes; MM = 2 $\Delta\theta = 6^\circ$162
E.9	SBT Bias Error Results for Extended Array Sizes; MM = 4, $\Delta\theta = 3^\circ$163
E.10	SBT Bias Error Results for Extended Array Sizes; MM = 4, $\Delta\theta = 6^\circ$164

CHAPTER I

INTRODUCTION

1.1 - Objective

Due to its crucial role in "target" localization, bearing estimation is the primary post-detection, sonar-array processing task. The bearing estimation performance of optimum and sub-optimum array processors is well known (see references [19], [27], and [32]) for the case of a random plane wave signal corrupted by Gaussian noise which is isotropic and uncorrelated. In many applications, however, it is inevitable that the array processor will encounter anisotropic noise fields containing one or more directional sources of interfering noise. It is the purpose of this research to investigate the effects of a highly anisotropic noise field on bearing estimation by optimum and sub-optimum array processors. A highly anisotropic noise field is defined as containing both multiple, unidirectional noise sources which are target-like in nature and an additive isotropic noise component which may or may not be spatially correlated.

The scope of this study is limited to sonar processor structures which are of a frozen design, i.e. non-adaptive. In essence we are assuming that target bearing is the only pertinent, unknown parameter. This limitation sidesteps the problem of defining a suitable methodology for estimating the noise field parameters (e.g. the Widrow [35] Griffiths [11] or Kelliher [10] algorithms for optimum processing and MacDonald's [18] sub-optimum processors) and the associated problems of convergence rates and sensitivity to mismatch of assumed and actual parameters (see Cox [7] and Kooij [17]).

1.2 - Background

Early studies of bearing estimation performance [4], [14], [31] addressed cases of signals known exactly except for random or unknown non-random parameters. Brennan [4], for example, assumed a known signal with random phase, obtained the Cramer-Rao bound on the mean square error of any unbiased estimator and compared it with the performance of a sub-optimal, amplitude-comparison, monopulse processor. Significantly, he demonstrated the efficiency of this sub-optimal estimator for large signal-to-noise ratios. The applicability of these and other early investigations is limited to environments that can adequately be modeled as isotropic, spatially uncorrelated Gaussian noise. In a later study, Seidman [27] examines several error bounds on the performance of known signal-random phase bearing estimators. In addition to the Cramer-Rao bound, Seidman obtains the Ziv-Zakai bound on the performance of any arbitrary estimator and a modified form of the Ziv-Zakai bound which offers a larger performance bound on the maximum-likelihood class of estimators. He provides an excellent analysis of the source bearing regions over which these bounds are and are not the greatest lower bounds and those regions where they are invalid. Additionally, the low SNR threshold below which the Cramer-Rao bound is inapplicable is presented along with some effects that array geometry has on these bounds. However, Seidman also restricts his analysis to independent, homogeneous white Gaussian noise.

MacDonald and Schultheiss [19], in a comparative analysis of optimum (maximum likelihood) and sub-optimum processors, extend the bearing estimation problem to broadband signals and noise. They bound the performance of the maximum likelihood estimator by the Cramer-Rao bound and derive an approximate expression for the rms error of an idealized

split-beam tracker. MacDonald and Schultheiss also invoke a spatially incoherent background noise model. These authors emphasize the effects of array size and geometry on the split-beam tracker performance relative to the Cramer-Rao bound. Specifically, it is shown that the split-beam tracker achieves the lower bound for a two hydrophone array while for a large number of uniformly spaced hydrophones its performance is degraded by approximately $\sqrt{4/3}$. Furthermore, the performance of a multi-sensor array whose geometry places $\frac{1}{2}$ of the elements at each end of the array achieves the bound exactly, assuming the noise remains independent at every hydrophone.

In reality, isotropic noise fields exhibit some degree of spatial correlation, not only for special array geometries such as MacDonald and Schultheiss [19] suggest, but also for uniformly spaced arrays whose hydrophone separation is small relative to the smallest wavelength of interest (e.g. Jacobson [15]). Miller [22] investigates the effects of noise correlation on correlator and delay-sum processors for the case of known signal. Miller obtains the maximum-likelihood bearing estimates from the outputs of these two processors and concludes that the delay-and-sum processor performs slightly better over most broadside bearings. Witt [36] also examines the effects of spatial correlation. He assumes the interelement noise correlation is linear and extends over at most two adjacent hydrophones. The performance of two types of multiplicative array processors is analyzed from several theoretical error measures and from the results of two computer simulations. Each of the performance measures analyzed indicates an increase in standard deviation of bearing estimation error and a shift, or bias, in the direction of the array steering angle. Witt concludes that the sum-and-correlate estimator is generally superior to the monopulse

estimator over the range of noise correlations examined. Wirt also references some additional studies which compare optimal and/or sub-optimal processor performances in isotropic but correlated noise fields.

In many operational situations, it is impossible to describe the noise cross-covariance properties at the hydrophone array as simply correlated and isotropic. For example, a noise field containing many unidirectional, interfering noise sources appropriately describes some high shipping density areas (e.g. the Mediterranean Sea). Also, transiting merchant or military vessels present a sonar observer with multiple, tightly grouped interfering noise sources of, possibly, similar characteristics. Similar highly anisotropic noise models are appropriate for sonar observation of controlled-access areas such as harbors and channels. One can also envision several geophysical problems wherein multiple directional noise sources are likely to interfere with source bearing estimation.

Such highly anisotropic noise fields have naturally received much attention in the area of adaptive array processing. In general, the design of adaptive array processors begins with limited assumptions of the signal and noise statistics and seeks to estimate the unknown parameters and track any subsequent changes in them. When the estimated parameter set is sufficiently "close" to the true parameter values, one is assured that a chosen estimation criterion (e.g. maximum likelihood or minimum-mean-square-error) is essentially satisfied. Questions of adaptive array performance commonly address the rate and integrity of convergence of the parameter estimates and the sensitivity to mismatch between the assumed parameters and their actual values.

Static, or fixed design, array processors which are based on exact a priori knowledge of signal and anisotropic noise, while impossible to

implement, do provide insight into the asymptotic performance of successfully adaptive implementations. Hence, there is a motivation to determine the effects of highly anisotropic noise on static, "optimum" bearing estimator structures. On the other hand, sub-optimum processors are often intentionally designed to operate in isotropic noise environments and are commonly of a static, or fixed, design. Operational situations which violate these assumptions of isotropicity motivate analyses of anisotropic noise effects on sub-optimal processors. In spite of these motivations, there are, to our knowledge, only a few analytical studies of the effects of anisotropic noise on the bearing estimation performance of optimal and sub-optimal processors.

In a broad study of the maximum likelihood estimator (ML) and two interference-nulling split-beam trackers (SBT) MacDonald [26] conducts a performance analysis of noise fields containing a single, directional interference in addition to isotropic background noise. The signal, noise and interference processes are defined by a set of non-random parameters. MacDonald presents a lengthy, theoretical derivation of the Cramer-Rao bound on ML performance and approximate expressions of bearing estimation variance for one pre-beamforming and one post-beamforming, interference-nulling, SBT processor. To facilitate analysis of these somewhat complicated expressions, MacDonald restricts his attention to cases of low signal-to-noise and high interference-to-noise ratios. He shows that these assumptions lead to a strong dependence of the CR bound on target-to-interference separation and number of hydrophones. The input-nulling (pre-beamforming) sub-optimal processor can effectively eliminate interference effects except for very small separations (less than one beamwidth) where it loses all capability to estimate source bearing. The output-nulling (post-beamforming)

79 01 30 085

processor, on the other hand, provides satisfactory performance at small separations but performs much worse than the input-nuller at separations greater than about one-beamwidth. There is no discussion of the nature of the bias error from these two sub-optimal processors which would quite possibly be significant at the SNR and INR levels studied. MacDonald recommends that the problem of multiple, directional noise sources be addressed in future investigations.

Cox [7] treats the problem of angular resolution of two closely spaced sources by conventional and optimal array processors. Resolution problems seek to determine the angular separation at which an observed phenomenon is known to result from two sources rather than one. Cox shows the resolution power of the optimal processor to be about three times better than that of the conventional processor for the classical Rayleigh resolution limit and high SNR. Cox indicates that high SNR levels are required for the resolution of two closely spaced interferers. This is a reasonable result since one would expect to be able to accurately estimate the bearing of a single, low-level source long before being able to resolve two closely spaced sources at the same bearing.

McGarty [21] considers a special case of noise anisotropy which includes multiple, directional noise interferences. In the context of air-traffic control, he investigates the effects of multiple, narrow-band, zero-mean Gaussian interferences on maximum likelihood estimation. This problem allows McGarty to describe the unknown interference parameters as random variables. In particular, he assumes that the interference bearings are uniformly distributed in azimuth over the interval $\left[-\frac{\pi}{2}, \frac{\pi}{2}\right]$ around broadside, and shows the resulting spatial noise correlation matrix to be a real, Toeplitz matrix of zero-order Bessel functions. Hence, he

addresses a special case of noise anisotropy which reduces to the well known "flatland" or cylindrically isotropic noise model [15], [17]. McGarty derives the Cramer-Rao bound for narrowband, isotropic but spatially correlated, white Gaussian noise which is then applicable to his assumed noise model. Although the bound requires numerical inversion of the noise correlation matrix, it is greatly simplified for this special case. The maximum likelihood estimation performance is seen to rapidly deteriorate for target bearings away from broadside. Even at broadside bearings, the performance is heavily dependent on interference-to-signal power. It is shown in chapter 2, however, that errors exist in McGarty's expression for the Cramer-Rao bound.

1.3 - Approach

The effects of highly anisotropic noise fields on source bearing estimation by optimal (ML) and sub-optimal (SBT) array processors are assessed from the behavior of several performance metrics subject to parametric variations in the directional-interference component of the acoustic field at the face of a hydrophone array. The directional interference component of the total noise field is defined by three parameters -- the number, mutual separation and bearings of the interferers. The detailed behavior of the bearing estimation performance metrics is examined for a fixed, baseline set of signal and array parameters followed by a restricted analysis for extended SNR and array size parameter values.

Chapter 2 discusses optimal or maximum likelihood bearing estimation and its performance characterization in terms of lower bounds on the

estimation error. The Fisher-Dugué-Cramer-Rao (FDCR)¹ bound is chosen as an appropriate performance measure of the maximum likelihood estimator. A mathematical model of the signal-plus-noise-plus-interference acoustic field-of-interest at the hydrophone array is then presented. Subsequently, a theoretical expression for the Cramer-Rao bound is derived as a function of the inverse, total-noise, covariance matrix.

In chapter 3, the split-beam tracker is presented as a conventional sonar processor designed for maximum performance in spatially incoherent noise fields. Given the signal-noise-interference model of chapter 2, theoretical expressions for the mean and standard deviation of the processor output are derived as functions of the array steering angle and the method of extracting source bearing from the SBT output is discussed. This chapter also derives an approximate, theoretical expression for the variance of the SBT bearing estimate.

As is often the case with analytical studies, it is difficult or impossible to obtain, under the necessary controls, pertinent field data for comparison with the approximate, theoretical results. A successful, alternative approach to field experiments is the exercise of a computer simulation of the appropriate array processor and its received acoustic fields (e.g. Witt [36]). Chapter 4 describes a digital computer simulation of the SBT bearing estimator which is developed to provide additional measures of sub-optimal processor performance in highly anisotropic noise fields. The SBT simulation algorithm is discussed along with the methodology employed

¹This bound is usually referred to as the Cramer-Rao bound although, as pointed out by Van Trees [33], it was originally formulated by R. A. Fisher and proven by D. Dugué. With due respect to Messrs Fisher and Dugué, we too shall hereafter refer to the FDCR bound as the Cramer-Rao or CR bound.

to generate samples of the input signal-plus-noise-plus-interference processes. An algorithm for estimating the source bearing from a zero-crossing in the simulation output is also developed.

The effects of multiple, directional noise sources on passive bearing estimation are examined in chapters 5 and 6 in terms of the parametric behavior of the Cramer-Rao bound, the approximate, theoretical SBT error metrics and the statistical measures of the simulated SBT performances. The total directional interference is defined by three parameters -- 1) the number of interferers, 2) the angular separation between adjacent interferers and 3) the mean bearing of the interference cluster. In chapter 5, a fixed baseline set of signal and array parameters is defined and the results of an extensive evaluation of the performance metrics derived in chapters 2, 3, and 4 is conducted. In chapter 6, the effects of extending the baseline values of SNR and array size are examined for a more restricted parametric variation of the total interference field.

Chapter 7 summarizes the research, presents its conclusions and offers recommendations for future research on related problems.

CHAPTER II

OPTIMUM BEARING ESTIMATION

As applied to parameter estimation, the term "optimum" implies that a properly formulated parameter estimate results in the satisfaction of some pre-selected performance criteria. For example, consider Bayesian estimation of random parameters. Here, one selects a cost function and defines the optimum estimate as that parameter value for which the total risk is minimized. In source bearing estimation problems, we are interested in unknown but non-random parameters. In such non-Bayesian estimation tasks, the method of maximum likelihood (ML) is an attractive approach. Very simply, one selects as the ML estimate that parameter value which would most likely have resulted in the observed data set. In other words, the ML estimate is the parametric location of the peak of the conditional probability density function $p(\vec{R} | b)$ where \vec{R} is the observed data set and b is the parameter-of-interest. Specifically, the ML estimate is the solution of the likelihood equation

$$\left. \frac{\partial}{\partial b} \{ \ln p(\vec{R} | b) \} \right|_{b=b_{ML}} = 0 \quad (2-1)$$

which occurs at the largest local maxima of $p(\vec{R} | b)$ [33]. Equation (2-1) is similar in form to the maximum a posteriori equation in Bayesian estimation. Indeed, the maximum a posteriori probability estimate is equal to the ML estimate when the amount of information known about the random parameter is negligible (i.e. infinite variance; completely unknown parameter). Consequently, maximum likelihood estimation has an intuitive foundation in Bayesian estimation theory.

The appeal of maximum likelihood estimation lies largely with several asymptotic properties that it possesses. These properties, which apply in the limit as the number of independent observations increases, state that the maximum likelihood estimate is 1) asymptotically unbiased, 2) asymptotically efficient and 3) asymptotically Gaussian distributed [33]. An efficient estimate is simply one whose variance achieves the Cramer-Rao lower bound. One can also show that any arbitrary, unbiased estimate which is efficient is identically the ML estimate [33]. Consequently, it seems reasonable to refer to maximum likelihood estimation of non-random parameters as "optimal" estimation. We shall subsequently use the two terms interchangeably. It is now of interest to address the performance of the optimal estimator.

2.1 - Performance of the Maximum Likelihood Estimator

The direct approach to a performance analysis of any arbitrary array processor requires that one first obtain theoretical expressions of the processor output in terms of the assumed input signal plus noise plus interference parameters. One can then, in theory, apply a parameter estimation algorithm (e.g. the bearing of the peak processor output) and obtain expressions for the estimation bias and variance errors. This direct approach is somewhat naive for all but the simplest processors. In particular, the solution of the maximum likelihood equation (2-1) is all but intractable. For ML estimation, alternative approaches to performance analysis have included use of simplifying assumptions and theoretical approximations [13] [5], numerical solutions of equation (2-1) [9], and the fortuitous, a priori selection and analysis of a processor structure which can subsequently be proven efficient [12]. However, even these approaches have addressed the

more tractable isotropic noise problem and/or small (two hydrophone) arrays.

An indirect approach to performance analysis of bearing estimators develops mathematically tractable lower bounds on the estimation error achievable by the processor of interest. This approach provides a performance metric which can be evaluated and, of course, for efficient estimators it reflects the actual performance. Two primary considerations govern the choice of an error bound in a processor's performance in any particular problem. The first consideration involves problem dependent questions such as: Is the parameter estimate to-be-bounded biased or unbiased? Will the estimation error be confined to a localized region of the parameter space or must global errors also be considered? Secondly, one obtains the best indication of actual processor performance by studying the behavior of the greatest, applicable lower bound and hence seeks to define such a measure.

Unfortunately, the most widely applicable error bounds do not usually prove to be the largest lower bounds for specific problems. In a study of narrowband signals in isotropic, white Gaussian noise, Seidman [27] evaluates such a bound -- the Ziv-Zakai bound. He defines this bound as a lower bound on the average mean square error for any estimator without restrictions on estimation bias or ambiguities. Seidman also presents the well known Cramer-Rao bound and a modification of the Ziv-Zakai bound which is applicable only to the maximum likelihood class of estimators. For the bounds Seidman analyzes, one can see that there are trade-offs to be made prior to selecting a particular bound as the performance metric of optimal estimation. For example, at broadside source bearings the Ziv-Zakai bound may be unnecessarily conservative while for bearings approaching endfire the

ML Ziv-Zakai bound becomes ineffective and the CR bound asymptotically approaches infinity. Since the CR bound applies to local or small-variance errors it is also shown to be inapplicable for small SNR. Although much is to be gained computationally from analyzing error bounds rather than actual processor error, it is apparent from Seidman's work that one must carefully select the most appropriate bounding metric. It is also noted that other bounds with attractive properties (e.g. the Bhattacharyya and Barankin bounds [33] and the J-divergence [25], an information-theoretic distance measure) seem almost as impractical to manipulate as true, bearing-estimation error expressions.

In this research, the bearing estimation performance of the optimal processor under varying degrees of anisotropic noise corruption is evaluated in terms of the parametric behavior of the CR bound. As mentioned above, the advantages of employing a bounding-type metric, in general, and the CR bound in particular are its computational simplicity and even its mathematical tractability relative to both other bounding metrics and the actual ML error expression. It is also believed that the CR bound is especially reflective of the ML estimator performance for the problem of interest. We are primarily interested in source bearing estimation errors arising from target tracking situations. Hence, we are interested in true source bearings at or near array broadside and expect to avoid the asymptotic growth of the CR bound near endfire bearings. Furthermore, since we have chosen to study the effects of anisotropic noise on operational, sub-optimum processors as well as the optimum structure, it is reasonable to restrict our attention to low, interference-to-noise ratios ($\text{INR}=0.1$) and moderate-to-high signal-to-noise ratios ($0.5 \leq \text{SNR} \leq 2.0$). We have some assurance in this case of avoiding problems with the low-SNR threshold of the CR bound

[27] and, according to El-Behrey and MacPhie [9], might even expect the ML estimate to be efficient in this application. We shall also assume in this research that the optimal estimator is unbiased. As a final motivation for selecting the CR bound as the sole, optimum-processor performance metric, we recall the asymptotic efficiency and unbiasedness of the ML estimate. We can thus expect the CR bound to very adequately reflect the performance of the optimal estimator.

In the following section, we develop a mathematical model of the acoustic field at the face of the array. In section 2.3 we derive a new expression for the CR bound on the bearing estimation variance applicable to arbitrary, anisotropic noise fields.

2.2 - Received Signal, Noise and Interference Models

In target tracking applications of sonar array processors, the received acoustic field at the face of the array is generally assumed to be the sum of a stationary, Gaussian, unidirectional signal process, $s(t, \theta_T)$, and a corrupting (e.g. self noise, ambient, shipping), Gaussian noise process, $n_a(t)$, which is possibly spatially anisotropic. In this study $n_a(t)$ is the sum of M mutually independent, unidirectional, Gaussian interferences, $i_m(t, \theta_m)$, and an independent, isotropic component, $n(t)$, also a Gaussian noise process. Hence, the total field at the face of the array is

$$x(t) = s(t, \theta_T) + n(t) + \sum_{m=1}^M i_m(t, \theta_m) \quad (2-2)$$

where θ_T is the source bearing and θ_m the m th interference bearing. Generally, a distant, interfering noise source $i_m(t, \theta_m)$ will be non-stationary due to its relative motion and/or effects of the propagating medium. Although in certain cases it is feasible to mathematically model such noise

processes [29], it is beyond the scope of the present study. Consequently, all of the Gaussian processes in the model (2-2) are assumed to be temporally stationary.

Several simplifications of equation (2-2) arise from the assumption that all directional processes originate in the far field of the array. With the possible exception of tow-ship radiated noise, this is a quite reasonable assumption for target tracking applications. This assumption allows us to neglect all amplitude gradients across the array resulting from the propagating components and thus reflect the directionality of target and interferences by relative propagation-time delays between hydrophones. Furthermore, we can model an equi-phase contour of the propagating components as a plane wavefront. The output of each element of a hydrophone array is simply a phase delayed version of equation (2-2) and, for the ℓ th sensor, can be written as

$$x_{\ell}(t) = s(t - \Delta_{\ell}) + n_{\ell}(t) + \sum_{m=1}^M i_m(t - \delta_{\ell}^m) \quad (2-3)$$

where Δ_{ℓ} is the source delay time at the ℓ th phone and δ_{ℓ}^m is the m th interference delay time at the ℓ th phone, both relative to an arbitrary reference point along the array. Figure 2.1 illustrates the acoustic situation modeled by the hydrophone outputs in equation (2-3) for the case of a uniformly-spaced, linear array. Without loss of generality, we can define hydrophone number 1 as the phase reference and obtain the following phase delays at the ℓ th hydrophone:

$$\begin{aligned} \Delta_{\ell} &= \frac{(\ell - 1)d}{c} \cdot \cos \theta_T \\ \delta_{\ell}^m &= \frac{(\ell - 1)d}{c} \cdot \cos \theta_m \quad m = 1, 2, \dots, M \end{aligned} \quad (2-4)$$

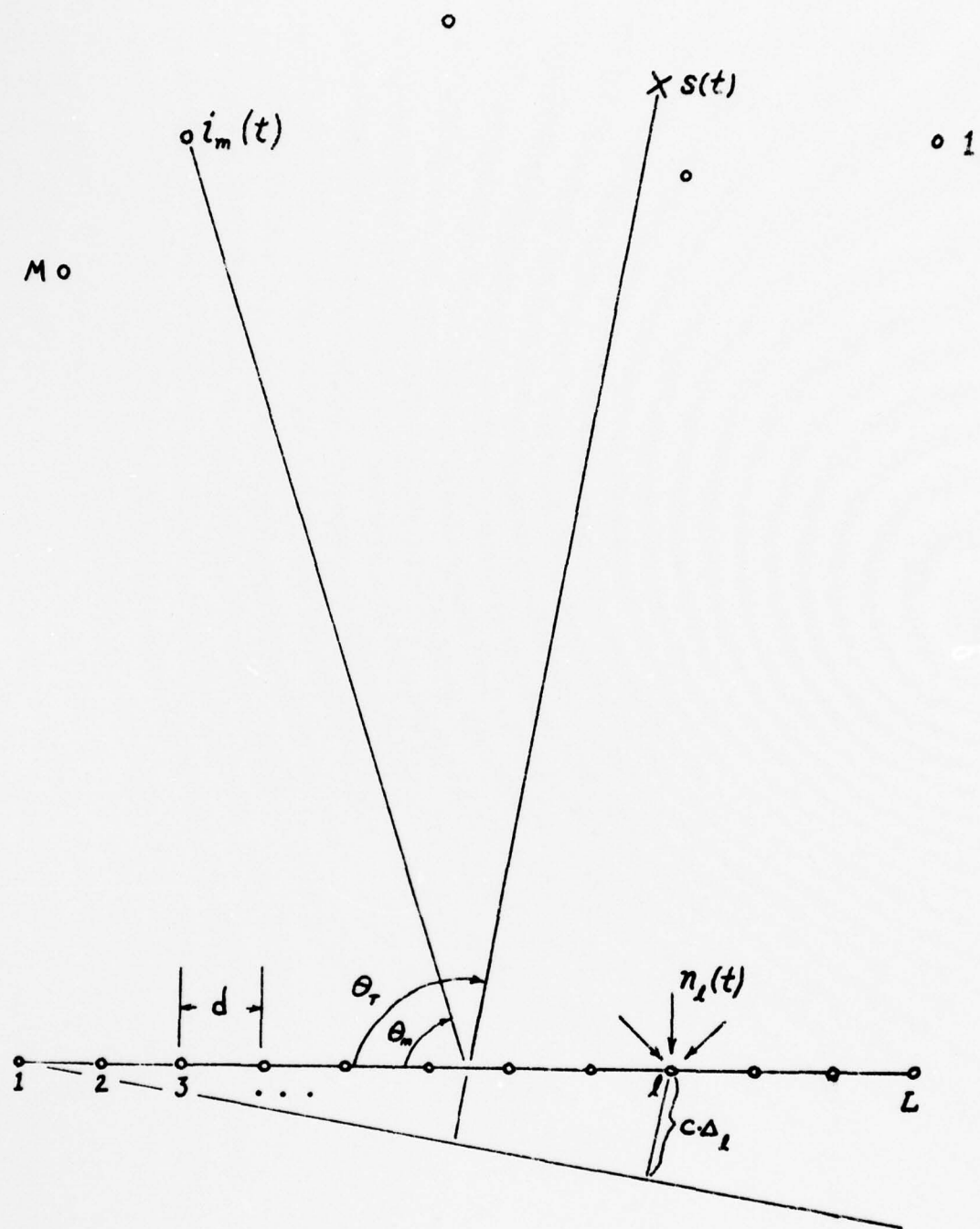


Figure 2.1 - Signal, Noise, Interference and Array Geometry

where d is the hydrophone spacing, c is the speed of sound in the sea (5000 ft/sec), θ_p is the true target bearing, M is the number of directional interferences, and θ_m is the m th interference bearing.

In general, the isotropic noise component at the ℓ th hydrophone, $n_\ell(t)$, is spatially correlated. Since previous investigations [22], [36] have addressed the effects of isotropic noise correlation and since our main interest lies in the effects of multiple interferences, $n(t)$ is assumed to be spatially uncorrelated and also homogeneous for the remainder of this research.

The signal-plus-total-noise field output from each hydrophone is observed by either optimal or sub-optimal processor only during the finite time-interval $[0, T]$. Each hydrophone output assumes the characterization of equation (2-3) over the T -second observation interval.² If one allows the uniform, linear array to contain L hydrophones, then the total array output waveform can be simply expressed in vector form as:

$$\vec{x}(t) = [x_1(t), x_2(t), \dots, x_L(t)] \quad (0 \leq t \leq T) \quad (2-5)$$

Equations (2-3), (2-4), and (2-5) along with the aforementioned simplifying assumptions define the observed signal-plus-total-noise process for which the optimal and sub-optimal bearing estimation performance metrics will be developed.

²Although we shall assume the hydrophone outputs, $x_\ell(t)$ to be continuous for all time regardless of observation interval size in order to facilitate Fourier Series representations, Bangs [2] notes that precise, alternate representations also exist when $x_\ell(t)$ is assumed to vanish outside the $[0, T]$ observation interval.

2.3 - The Cramer-Rao Bound³

It is well known [33], [21], [18] that the Cramer-Rao (CR) lower bound, σ_{CR, θ_T}^2 , on the variance of any unbiased estimate of source bearing is

$$\sigma_{CR, \theta_T}^2 \triangleq - \left\{ E \left[\frac{\partial^2}{\partial \theta_T^2} \ell(\vec{x} | \theta_T) \right] \right\}^{-1} \quad (2-6)$$

where

θ_T is the unknown source bearing,

\vec{x} is the observation vector,

$\ell(\vec{x} | \theta_T)$ is the log-likelihood ratio of \vec{x} given θ_T and,

$E[\cdot]$ denotes statistical expectation with respect to the data vector \vec{x} .

Evaluation of equation (2-6) first requires the generation of $\ell(\vec{x} | \theta_T)$ which in turn is defined as

$$\ell(\vec{x} | \theta_T) = \log \Lambda(\vec{x} | \theta_T) = \log \left\{ \frac{p(\vec{x} | S + N, \theta_T)}{p(\vec{x} | N)} \right\} \quad (2-7)$$

where $p(\vec{x} | S + N, \theta_T)$ is the probability density function (pdf) of the data given that a signal at bearing θ_T occurs in addition to the noise while $p(\vec{x} | N)$ is the pdf of the data given that only noise occurs. Since the components of \vec{x} (see equation (2-3)) are sums of real Gaussian, random noise processes, \vec{x} will be a real vector Gaussian random process and $\ell(\vec{x} | \theta_T)$ in (2-7) follows directly upon the determination of the mean vector, \vec{m} , and covariance function, $K(t - u)$, of the data vector.

Generation of the log-likelihood ratio is, however, facilitated by a reformulation of the data vector $\vec{x}(t)$ into a characterization that is orthogonal in the temporal dimension. For time-stationary processes, the

³See footnote 1, page 8.

Fourier series of $\hat{x}(t)$ over the finite interval $[0, T]$ is such a characterization. The ℓ th component of $\hat{x}(t)$ is defined as

$$x_\ell(t) \triangleq \frac{1}{T} \sum_{k=-\infty}^{\infty} X_\ell(j\omega_k) e^{+j\omega_k t} \quad (2-8a)$$

where
$$X_\ell(j\omega_k) = \int_0^T x_\ell(t) e^{-j\omega_k t} dt \quad k = \dots, -1, 0, +1, \dots \quad (2-8b)$$

are the Fourier coefficients of $x_\ell(t)$ and where $\omega_k = \frac{2\pi}{T} k$ is the Fourier conjugate frequency variable. If the signal-plus-total-noise process is bandlimited to $\omega_B = \pm \frac{2\pi}{T} N$, then the series in equation (2-8a) spans only those discrete frequencies $(2N + 1)$ within $[-\omega_N, +\omega_N]$. Furthermore, since $x_\ell(t)$ is a real function of time, the Fourier coefficients defined by (2-8b) are conjugate symmetric, i.e.

$$X_\ell(j\omega_k) = X_\ell^c(-j\omega_k) \quad k = 0, 1, \dots, N$$

Consequently, (2-8a) can be rewritten as

$$x_\ell(t) = \frac{2}{T} \sum_{k=0}^N \operatorname{Re} \left\{ X_\ell(j\omega_k) e^{+j\omega_k t} \right\}$$

The Fourier characterization of the observed data vector can now be expressed as the following $N \times L$ dimensional, complex vector in the Fourier domain:

$$\vec{X}_D \triangleq \left[X_1(j\omega_0), \dots, X_L(j\omega_0), X_1(j\omega_1), \dots, X_L(j\omega_1), \dots, X_L(j\omega_N) \right]' \quad (2-9)$$

where $X_\ell(j\omega_k)$ is given by (2-8b) and the "prime" superscript, $'$, denotes the vector transpose.

It is conceptually straightforward to evaluate the CR bound for the observation vector in (2-9) by the substitution of equations (2-3) and (2-8b).

The end result is a theoretical expression which reflects the dependence of

the CR bound on the signal, noise, and interference parameters. Such an approach was followed by MacDonald [18] for the case of a single, broadband, plane wave interference. The algebraic manipulations required to effect this approach for a single interference are quite complex and lengthy. Preliminary attempts to follow this approach for the case of an arbitrary number of multiple interferences have confirmed MacDonald's predictions that such a theoretical derivation is essentially intractable (even for two interferences). Consequently, we have chosen to follow McGarty's [21] approach which is a mathematically feasible one but obscures the explicit roles played by the interference parameters since it requires the numerical inversion of the noise-plus-interference spatial correlation matrix at each and every frequency, ω_k . In other words, the isotropic and anisotropic noise components in equation (2-3) are lumped together into a single noise component $n_{a,\ell}(t)$. The log-likelihood ratio and, subsequently, the CR bound are derived in terms of the inverse of the covariance matrix of $\vec{n}_a(t)$. The evaluation of the bound, discussed in chapters 5 and 6, requires the numerical inversion of this total noise covariance matrix. Although numerical matrix inversion is a costly operation, it will be seen that the noise covariance matrix is a complex, Toeplitz matrix for which faster inversion algorithms (e.g. [30]) exist.

The derivation of the log-likelihood ratio $\ell(\vec{X}_D | \theta_T)$ for Fourier characterizations of stationary data (e.g. equation (2-7)) is straightforward [21], [32]. Such a derivation using our notation is presented in appendix A for convenience. The final result is the following expression for the log-likelihood ratio:

$$\ell(\vec{X}_D | 0_T) = \sum_{k=0}^N \left\{ \ell_n \left(\frac{\sigma_T^2(\omega_k)}{TS(\omega_k)} \right) + \sigma_T^2(\omega_k) \vec{X}(\omega_k) \underline{K}_N^{-1}(\omega_k) \vec{a}(\omega_k) \vec{a}^*(\omega_k) \underline{K}_N^{-1}(\omega_k) \vec{X}^*(\omega_k) \right\} \quad (2-10)$$

where

$$\sigma_T^2(\omega_k) = \frac{TS(\omega_k)}{1 + TS(\omega_k) \vec{a}^*(\omega_k) \underline{K}_N^{-1}(\omega_k) \vec{a}(\omega_k)},$$

T is the total observation time,

$S(\omega_k)$ is the signal power spectral level at frequency ω_k ,

$\vec{X}(\omega_k)$ is a vector of the L components of \vec{X} , (equation (2-9))

corresponding to frequency ω_k ,

$\underline{K}_N^{-1}(\omega_k) = \left[E \left\{ \vec{N}(\omega_k) \vec{N}^*(\omega_k) \right\} \right]^{-1}$ is the inverse of the correlation matrix (zero-mean noise processes) of the Fourier characterization (at ω_k) of the total-noise component $n_{a,\ell}(t)$,

$\vec{a}(\omega_k)$ is the phase delay vector of the signal process with ℓ th component of $\vec{a}(\omega_k)$ being,

$$a_\ell(\omega_k) = \exp \left\{ -j\omega_k \frac{(\ell-1)d}{c} \cos \theta_T \right\}, \quad \ell = 1, 2, \dots, L,$$

$\ell n(\cdot)$ is the natural logarithm, and $*$ denotes the conjugate,

transpose vector operation.

Substitution of equation (2-10) into equation (2-6) yields,

$$\begin{aligned} \sigma_{CR, \theta_T}^2 &= - \left\{ E \left[\frac{\partial^2}{\partial \theta_T^2} \ell(\vec{X}_D | \theta_T) \right] \right\}^{-1} \\ &= - \left\{ \sum_{i=0}^N E \left[\frac{\partial^2}{\partial \theta_T^2} \ell_i(\vec{X}(\omega_i) | \theta_T) \right] \right\}^{-1} \end{aligned} \quad (2-11)$$

where $\ell_i(\vec{X}(\omega_i) | \theta_T)$ is the quantity in braces in equation (2-10). Note that θ_T enters equation (2-10) only through the signal phase delay vector, $\vec{a}(\omega_i)$, and always appears as $\cos(\theta_T)$ rather than θ_T . If we let $\mu = \cos(\theta_T)$ it can be shown [5], [20] that a relation exists between the variance bound

on $\hat{\theta}_T$ given by (2-11) and a variance bound on $\mu(\sigma_{CR,\mu}^2)$ which for the approximately broadside bearings, ($\theta_T \approx 90$) involved in target tracking, is

$$\sigma_{CR,\theta_T}^2 = \frac{\sigma_{CR,\mu}^2}{\sin^2 \theta_T} \quad (2-12)$$

Since the partial derivatives required by (2-11) are much easier to obtain when taken with respect to μ rather than θ_T , we shall develop an expression for $\sigma_{CR,\mu}^2$ and invoke (2-12) to obtain the CR bound on the variance of source bearings.

We can, for simplicity, drop the explicit reference to the frequency dependence of the component terms of $\ell_1(\hat{X}(\omega_1)|\theta_T)$, and write the log-likelihood ratio for the i th frequency as

$$\ell_i = \ell_1(X(\omega_1)|\theta_T) = \ln\left(\frac{\sigma_T^2}{TS}\right) + \sigma_T^2 \hat{X}^* \underline{K}_N^{-1} \underline{a} \underline{a}^* \underline{K}_N^{-1} \hat{X} \quad (2-13)$$

where the definitions of the RHS terms of (2-13) follow (2-10). It is interesting to note that the likelihood ratio for the i th frequency given by (2-13) is almost identical to McGarty's [21] result for narrowband processes. His narrowband result differs from our single-frequency result in that he assumes the number, amplitude, frequency, and bearing of each interferer to be random variables. He further assumes specific pdf's for these parameters which in turn result in a real, Toeplitz correlation matrix (\underline{K}_N in (2-13), however, is complex) comprised of zero-order, modified Bessel functions. In essence, his assumptions define a special anisotropic noise model equivalent to the well-known "flatland" or cylindrically isotropic noise model [15], [17].

Differentiating (2-13) once with respect to μ , we obtain

$$\begin{aligned} \frac{\partial \ell_i}{\partial \mu} &= \frac{\partial}{\partial \mu} \ell_n \left(\frac{\sigma_T^2}{TS} \right) + \frac{\partial \sigma_T^2}{\partial \mu} \frac{\vec{a}^*}{\underline{K}_N^{-1} \vec{X} \vec{X}^* \underline{K}_N^{-1} \vec{a}} \\ &+ \sigma_T^2 \frac{\partial \vec{a}^*}{\partial \mu} \underline{K}_N^{-1} \vec{X} \vec{X}^* \underline{K}_N^{-1} \vec{a} + \sigma_T^2 \frac{\vec{a}^*}{\underline{K}_N^{-1} \vec{X} \vec{X}^* \underline{K}_N^{-1}} \frac{\partial \vec{a}}{\partial \mu}. \end{aligned} \quad (2-14)$$

From the definition of \vec{a} ,

$$\begin{aligned} \left(\frac{\partial \vec{a}}{\partial \mu} \right)_\ell &= -j\omega \frac{(\ell-1)d}{c} \exp \left\{ -j\omega \frac{(\ell-1)d}{c} \mu \right\} \\ &= -j\omega \frac{(\ell-1)d}{d} (\vec{a})_\ell \end{aligned}$$

so that

$$\begin{aligned} \frac{\partial \vec{a}}{\partial \mu} &= (-j\omega \frac{d}{c}) \cdot \text{diag} (0, 1, 2, \dots, L-1) \vec{a} \\ &= \underline{A} \vec{a} \end{aligned} \quad (2-15)$$

where the matrix \underline{A} is

$$\underline{A} = (-j\omega \frac{d}{c}) \cdot \text{diag} (0, 1, 2, \dots, L-1) \quad (2-16)$$

Also

$$\begin{aligned} \frac{\partial \vec{a}^*}{\partial \mu} &= \left(\frac{\partial \vec{a}}{\partial \mu} \right)^* = (\underline{A} \vec{a})^* \\ &= \left(\underline{A}^c \vec{a}^c \right)' = \vec{a}^* \underline{A}^* \end{aligned} \quad (2-17)$$

where \underline{A}^* is the conjugate transpose of \underline{A} defined in (2-16). The following properties exist for the matrix \underline{A} :

$$\underline{A} = -\underline{A}^c$$

$$\underline{A} = \underline{A}'$$

$$\underline{A} = -\underline{A}^*$$

Differentiating (2-14) with respect to μ yields,

$$\begin{aligned}
 \frac{\partial^2 \ell_1}{\partial \mu^2} = & \frac{\partial^2}{\partial \mu^2} \ell_n \left(\frac{\sigma_T^2}{TS} \right) + \frac{\partial^2 \sigma_T^2}{\partial \mu^2} \vec{a} * \underline{K}_N^{-1} \vec{X} \vec{X} * \underline{K}_N^{-1} \vec{a} \\
 & + 2 \frac{\partial \sigma_T^2}{\partial \mu} \vec{a} * \underline{A} \underline{A} * \underline{K}_N^{-1} \vec{X} \vec{X} * \underline{K}_N^{-1} \vec{a} + 2 \frac{\partial \sigma_T^2}{\partial \mu} \vec{a} * \underline{K}_N^{-1} \vec{X} \vec{X} * \underline{K}_N^{-1} \underline{A} \underline{A} \vec{a} \\
 & + \sigma_T^2 \vec{a} * \underline{A} \underline{A} * \underline{K}_N^{-1} \vec{X} \vec{X} * \underline{K}_N^{-1} \vec{a} + \sigma_T^2 \vec{a} * \underline{K}_N^{-1} \vec{X} \vec{X} * \underline{K}_N^{-1} \underline{A} \underline{A} \vec{a} \\
 & + 2 \sigma_T^2 \vec{a} * \underline{A} \underline{K}_N^{-1} \vec{X} \vec{X} * \underline{K}_N^{-1} \underline{A} \vec{a} \quad (2-18)
 \end{aligned}$$

Evaluation of the statistical expectation of (2-18) requires knowledge of the expectation $E \{ \vec{X} \vec{X}^* \}$. Substitution of (2-3) and (2-8b) into (2-9) yields

$$\begin{aligned}
 \vec{X} = \vec{X}(j\omega_i) &= s(j\omega_i) \vec{a} + \vec{n}(j\omega_i) + \sum_{m=1}^M i_m(j\omega_i) \vec{b}_m \\
 &= s(j\omega_i) \vec{a} + \vec{n}_a(j\omega_i) \quad (2-19)
 \end{aligned}$$

where $s(j\omega_i)$, $\vec{n}(j\omega_i)$ and $i_m(j\omega_i)$ are Fourier transforms of the signal, noise, and interference processes respectively,

$$\vec{b}_m = \exp \left\{ -j\omega_i \frac{(\ell-1)d}{c} \cdot \cos \theta_m \right\} \text{ is the phase delay vector of the } m\text{th interference, and}$$

$\vec{n}_a(j\omega)$ is the Fourier transform vector of the total corrupting noise process.

Assuming the signal, noise and interference processes are bandlimited and assuming T is much larger than the correlation time of these processes, the expectation required by (2-18) is expressible in terms of the power spectral densities of the component processes [3] as:

$$\begin{aligned}
E \{ \vec{X} \vec{X}^* \} &= E \left\{ \left[\vec{s} \frac{1}{a} + \vec{n} + \sum_{m=1}^M \vec{i}_m \frac{1}{b_m} \right] \left[\vec{s}^* \frac{1}{a}^* + \vec{n}^* + \sum_{m=1}^M \vec{i}_m^* \frac{1}{b_m}^* \right] \right\} \\
&= TS \frac{1}{a} \frac{1}{a}^* + T N \underline{I} + T \sum_{m=1}^M \vec{i}_m \frac{1}{b_m} \frac{1}{b_m}^* \\
&= TS \frac{1}{a} \frac{1}{a}^* + \underline{K}_N
\end{aligned} \tag{2-20}$$

where S , N , and \vec{i}_m are the signal, noise, and m th interference power spectral densities at the implied frequency, and

$$\underline{K}_N = T N \underline{I} + T \sum_{m=1}^M \vec{i}_m \frac{1}{b_m} \frac{1}{b_m}^* \text{ is the covariance matrix of the total noise field at the implied frequency.}$$

The matrix \underline{K}_N is the covariance matrix whose inverse must be computed numerically in evaluating the CR bound.

The straightforward, although quite tedious, substitution of equation (2-20) into equation (2-18), yields

$$\begin{aligned}
E \left\{ \frac{\partial^2 \ell_i}{\partial \mu^2} \right\} &= \frac{\partial^2}{\partial \mu^2} \left(\ell_n - \frac{\sigma_T^2}{TS} \right) + \left(\frac{\partial^2}{\partial \mu^2} \sigma_T^2 \right) \frac{1}{a}^* \underline{K}_N^{-1} \frac{1}{a} \frac{TS}{\sigma_T^2} \\
&\quad + 2TS \sigma_T^2 \left\{ \operatorname{Re} \left[\left(\frac{1}{a}^* \underline{K}_N^{-1} \frac{1}{a} \right) \cdot \left(\frac{1}{a}^* \underline{K}_N^{-1} \underline{A} \underline{A} \frac{1}{a} \right) \right] + \left| \frac{1}{a}^* \underline{A} \underline{K}_N^{-1} \frac{1}{a} \right|^2 \right\} \\
&\quad + \frac{1}{a}^* \left[\underline{A}^* \underline{K}_N^{-1} + \underline{K}_N^{-1} \underline{A} \right] \frac{1}{a} \cdot \left(\frac{2TS}{\sigma_T^2} \frac{\partial \sigma_T^2}{\partial \mu} \right) \\
&\quad + \sigma_T^2 \left\{ \frac{1}{a}^* \underline{A}^* \left[\underline{A}^* \underline{K}_N^{-1} + \underline{K}_N^{-1} \underline{A} \right] \frac{1}{a} + \frac{1}{a}^* \left[\underline{A}^* \underline{K}_N^{-1} + \underline{K}_N^{-1} \underline{A} \right] \underline{A} \frac{1}{a} \right\}
\end{aligned} \tag{2-21}$$

Details of the above derivation are carried out in appendix B. Equation (2-21) is an expression for the i th additive component of the negative inverse of the CR bound and is valid for any plane wave, unidirectional, Gaussian signal and any corrupting Gaussian noise field with arbitrary spatial power-distribution defined by \underline{K}_N^{-1} . Since (2-21) is valid for any

arbitrary, complex covariance matrix it is, to our knowledge, an original result. McGarty's comparable, narrowband result [21, eqn. 38] which is valid only for real inverse covariance matrices, is equivalent to the first four terms of (2-21). Not only is equation (2-21) more general than his result, it can be shown that, under his assumptions, McGarty's result is in error. Since his \underline{K}_N^{-1} is a real, symmetric matrix and $\underline{A} = -\underline{A}^*$, McGarty's result requires that the last three terms of our equation (2-21) vanish as a consequence of the following equality:

$$\underline{A}^* \underline{K}_N^{-1} + \underline{K}_N^{-1} \underline{A} = \underline{0} \quad (2-22)$$

where $\underline{0}$ denotes the null matrix. However, observe that

$$\underline{A}^* \underline{K}_N = (\underline{A}^*)' (\underline{K}_N^{-1})' = (\underline{K}_N^{-1} \underline{A}^*)' = -(\underline{K}_N^{-1} \underline{A})' .$$

It is easy to show that the matrix product $\underline{K}_N^{-1} \underline{A}$ is symmetric if and only if \underline{K}_N^{-1} is a diagonal matrix. Hence, the inequality in (2-22) and McGarty's expression for the CR bound are invalid under the governing assumptions. However, if the sole source of noise is the uncorrelated component, the equality (2-22) would, of course, hold. In cases where (2-22) does hold, not only do the last three terms of (2-21) vanish, but, as we shall see, the first two terms of (2-21) also vanish.

Equation (2-21) still requires evaluation of the derivatives of σ_T^2 . Using the chain rule of differentiation, it is easy to obtain the following expression for the first derivative of σ_T^2 with respect to μ :

$$\begin{aligned}\frac{\partial \sigma_T^2}{\partial \mu} &= \frac{\partial}{\partial \mu} \left(\frac{TS}{1 + TS \frac{\vec{a}}{a} \star \frac{\underline{A} \star \underline{K}_N^{-1} \vec{a}}{a}} \right) \\ &= -(\sigma_T^2)^2 \frac{\vec{a}}{a} \star \left[\frac{\underline{A} \star \underline{K}_N^{-1}}{a} + \frac{\underline{K}_N^{-1} \underline{A}}{a} \right] \frac{\vec{a}}{a}\end{aligned}\quad (2-23)$$

Likewise, it is straightforward to obtain the second derivative:

$$\begin{aligned}\frac{\partial^2}{\partial \mu^2} \sigma_T^2 &= -(\sigma_T^2)^2 \left\{ \frac{\vec{a}}{a} \star \frac{\underline{A} \star \underline{K}_N^{-1}}{a} + \frac{\underline{K}_N^{-1} \underline{A}}{a} \right\} \frac{\vec{a}}{a} + \frac{\vec{a}}{a} \star \left[\frac{\underline{A} \star \underline{K}_N^{-1}}{a} + \frac{\underline{K}_N^{-1} \underline{A}}{a} \right] \frac{\underline{A} \star \vec{a}}{a} \Bigg\} \\ &\quad + 2(\sigma_T^2)^3 \left\{ \frac{\vec{a}}{a} \star \left[\frac{\underline{A} \star \underline{K}_N^{-1}}{a} + \frac{\underline{K}_N^{-1} \underline{A}}{a} \right] \frac{\vec{a}}{a} \right\}^2\end{aligned}\quad (2-24)$$

Now, observe that the first two terms in (2-21) can be written as:

$$\begin{aligned}\frac{\partial^2}{\partial \mu^2} \left(\ell_n \frac{\sigma_T^2}{TS} \right) &+ \frac{\partial^2 \sigma_T^2}{\partial \mu^2} \frac{\vec{a}}{a} \star \frac{\underline{K}_N^{-1}}{a} \frac{\vec{a}}{a} \frac{TS}{\sigma_T^2} \\ &= \frac{1}{\sigma_T^2} \frac{\partial^2 \sigma_T^2}{\partial \mu^2} - \frac{1}{(\sigma_T^2)^2} \left(\frac{\partial \sigma_T^2}{\partial \mu} \right)^2 + \left(TS \frac{\vec{a}}{a} \star \frac{\underline{K}_N^{-1}}{a} \frac{\vec{a}}{a} \right) \cdot \frac{1}{\sigma_T^2} \frac{\partial^2 \sigma_T^2}{\partial \mu^2} \\ &= \frac{1}{(\sigma_T^2)^2} \left\{ TS \frac{\partial^2 \sigma_T^2}{\partial \mu^2} - \left(\frac{\partial \sigma_T^2}{\partial \mu} \right)^2 \right\}\end{aligned}\quad (2-25)$$

The substitution of equations (2-23), (2-24), and (2-25) into equation (2-21) yields,

$$\begin{aligned}E \left\{ \frac{\partial^2}{\partial \mu^2} \ell_i \right\} &= -TS \left\{ \frac{\vec{a}}{a} \star \frac{\underline{A} \star \underline{K}_N^{-1}}{a} + \frac{\underline{K}_N^{-1} \underline{A}}{a} \right\} \frac{\vec{a}}{a} + \frac{\vec{a}}{a} \star \left[\frac{\underline{A} \star \underline{K}_N^{-1}}{a} + \frac{\underline{K}_N^{-1} \underline{A}}{a} \right] \frac{\underline{A} \star \vec{a}}{a} \Bigg\} \\ &\quad + 2TS\sigma_T^2 \left\{ \frac{\vec{a}}{a} \star \left[\frac{\underline{A} \star \underline{K}_N^{-1}}{a} + \frac{\underline{K}_N^{-1} \underline{A}}{a} \right] \frac{\vec{a}}{a} \right\}^2 - (\sigma_T^2)^2 \left\{ \frac{\vec{a}}{a} \star \left[\frac{\underline{A} \star \underline{K}_N^{-1}}{a} + \frac{\underline{K}_N^{-1} \underline{A}}{a} \right] \frac{\vec{a}}{a} \right\}^2 \\ &\quad + 2TS\sigma_T^2 \left\{ \text{Re} \left[\left(\frac{\vec{a}}{a} \star \underline{K}_N^{-1} \frac{\vec{a}}{a} \right) \cdot \left(\frac{\vec{a}}{a} \star \underline{K}_N^{-1} \frac{\underline{A} \star \vec{a}}{a} \right) \right] + \left| \frac{\vec{a}}{a} \star \frac{\underline{A} \star \underline{K}_N^{-1}}{a} \frac{\vec{a}}{a} \right|^2 \right\} \\ &\quad - 2TS\sigma_T^2 \left\{ \frac{\vec{a}}{a} \star \left[\frac{\underline{A} \star \underline{K}_N^{-1}}{a} + \frac{\underline{K}_N^{-1} \underline{A}}{a} \right] \frac{\vec{a}}{a} \right\}^2 + \sigma_T^2 \left\{ \frac{\vec{a}}{a} \star \left[\frac{\underline{A} \star \underline{K}_N^{-1}}{a} + \frac{\underline{K}_N^{-1} \underline{A}}{a} \right] \frac{\underline{A} \star \vec{a}}{a} \right. \\ &\quad \left. + \frac{\vec{a}}{a} \star \left[\frac{\underline{A} \star \underline{K}_N^{-1}}{a} + \frac{\underline{K}_N^{-1} \underline{A}}{a} \right] \frac{\underline{A} \star \vec{a}}{a} \right\}\end{aligned}\quad (2-26)$$

For notational simplicity, define an $L \times L$ matrix \underline{G} as:

$$\underline{G} = \underline{A}^* \underline{K}_N^{-1} + \underline{K}_N^{-1} \underline{A} \quad (2-27)$$

Substituting (2-27) into (2-26) and combining terms yields,

$$\begin{aligned} E \left\{ \frac{\partial^2}{\partial \mu^2} \ell_1 \right\} &= (\sigma_T^2 - TS) \left\{ \underline{a}^* \underline{A}^* \underline{G} \underline{a} + \underline{a}^* \underline{G} \underline{A} \underline{a} \right\} \\ &\quad - (\sigma_T^2)^2 \left\{ \underline{a}^* \underline{G} \underline{a} \right\}^2 + 2TS\sigma_T^2 \left\{ \text{Re} \left[(\underline{a}^* \underline{K}_N^{-1} \underline{a}) \cdot (\underline{a} \underline{K}_N^{-1} \underline{A} \underline{A} \underline{a}) \right] \right. \\ &\quad \left. + \left| \underline{a}^* \underline{A} \underline{K}_N^{-1} \underline{a} \right|^2 \right\} \\ &= 2TS\sigma_T^2 \left\{ (\underline{a}^* \underline{K}_N^{-1} \underline{a}) \cdot \text{Re} \left[\underline{a}^* \underline{K}_N^{-1} \underline{A} \underline{A} \underline{a} - \underline{a}^* \underline{G} \underline{A} \underline{a} \right] \right. \\ &\quad \left. + \left| \underline{a}^* \underline{A} \underline{K}_N^{-1} \underline{a} \right|^2 \right\} - \left\{ \sigma_T^2 \underline{a}^* \underline{G} \underline{a} \right\}^2 \end{aligned} \quad (2-28)$$

where we have used the facts that

$$\underline{a}^* \underline{A}^* \underline{G} \underline{a} = (\underline{a}^* \underline{G} \underline{A} \underline{a})^c$$

$$\text{and} \quad (\sigma_T^2 - S) = -\sigma_T^2 TS \underline{a}^* \underline{K}_N^{-1} \underline{a} \quad (2-29)$$

We can now use equations (2-11), (2-12) and (2-28) to obtain the following final expression for the Cramer-Rao bound on the variance of any unbiased estimator of source bearing:

$$\begin{aligned} \sigma_{CR, \theta_T}^2 &= - \left\{ \sin^2 \theta_T \sum_{i=0}^N \left[2 TS\sigma_T^2 \left\{ (\underline{a}^* \underline{K}_N^{-1} \underline{a}) \cdot \text{Re} \left[\underline{a}^* \underline{K}_N^{-1} \underline{A} \underline{A} \underline{a} - \underline{a}^* \underline{G} \underline{A} \underline{a} \right] \right. \right. \right. \\ &\quad \left. \left. + \left| \underline{a}^* \underline{A} \underline{K}_N^{-1} \underline{a} \right|^2 \right\} - \left\{ \sigma_T^2 \underline{a}^* \underline{G} \underline{a} \right\}^2 \right] \right\}^{-1} \end{aligned} \quad (2-30)$$

where each variable within the summation is dependent on the implied frequency ω_i , and where \underline{G} is defined by equation (2-27) and the definitions of the remaining quantities follow equation (2-10). Recall from the previous

discussion that the tractability of (2-30) arises from our willingness to numerically invert the noise covariance matrix, \underline{K}_N , at each of the N component frequencies. The explicit definition of \underline{K}_N^{-1} in terms of our noise model follows equation (2-20) above. It is again mentioned that "fast" inversion algorithms exist which exploit the Toeplitz property of \underline{K}_N . In particular, when numerical inversion of \underline{K}_N is required in this investigation, we shall employ the algorithm developed by Trench [30].

MacDonald [18] was able to derive a theoretical expression for the CR bound when the degree of anisotropy is limited to a single plane wave interferer. MacDonald's interest, though, is in the effects of a single, dominant interference on a weak source. Since our result in equation (2-30) is entirely general, it is of interest to compare its behavior with MacDonald's theoretical results. Specifically, he presents the behavior of a normalized CR bound for an interference-to-noise ratio of 1.0 and $L(S/N) \ll 1$, where L is the number of uniformly spaced hydrophones. Figure 2.2 compares equation (2-30) with MacDonald's un-normalized result for variable target-to-interference separations and for the parameter values used in this study. Although, for the parameters of interest, there is only a minimal bearing estimation capability, figure 2.2 does show excellent agreement between the two expressions for the CR bound. MacDonald indicates that he has ignored some oscillatory terms in his graphical presentation of the bound. He assumes these terms are negligible due to the high INR, low SNR condition. Hence, the oscillatory behavior of our result (equation (2-30)) in figure 2.2 is to be expected.

$$Y = (2\pi/T) \cdot K \cdot (d/c) (\cos\theta_T - \cos\theta_i)$$

θ_i = Single Interference Bearing

$T = 0.128$ sec, $K=13$, $d=20$ ft, $\theta_T=90^\circ$

LL= 10 hydrophones, INR=1.0

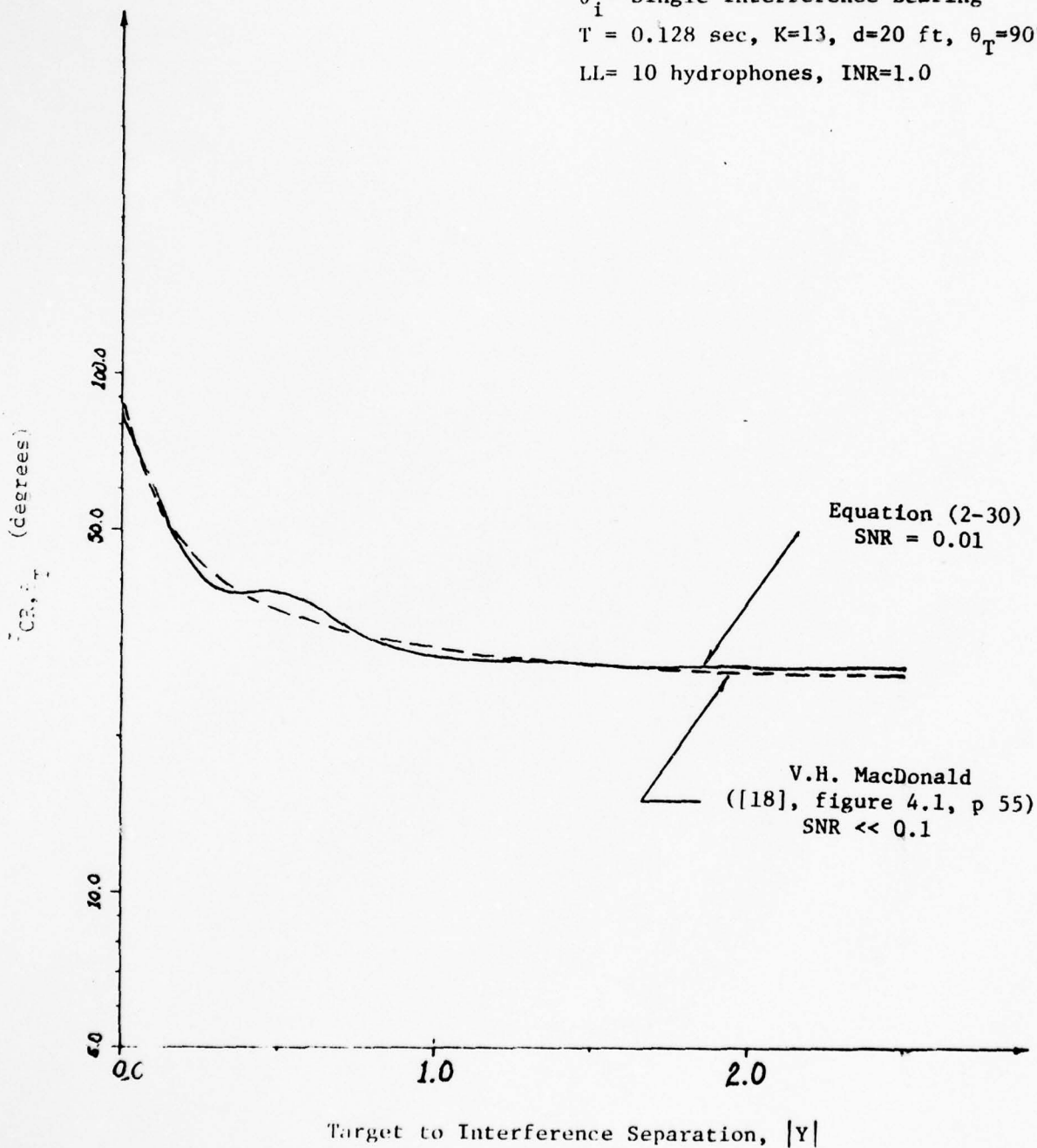


Figure 2.2 - Comparative Behavior of Equation (2-30) and MacDonald's Graphical Presentation [18] of the Cramer-Rao Bound for a Single Interferer.

CHAPTER III

SUB-OPTIMUM ESTIMATION: THE SPLIT-BEAM TRACKER

In general, one is attracted to sub-optimum implementations of parameter estimators by their potential economic benefits. Of course such implementations are usually realized at the expense of degradations in estimator performance. In passive-sonar bearing estimation problems, an intuitively logical approach is the extraction of source bearing information from the travel-time delay measured at the peak of the cross-correlation between two spatially separated receivers. Carter [5] gives a detailed discussion of this sub-optimum technique for a generalized class of cross-correlation processors. A popular extension of this approach to multiple hydrophone arrays is the split-beam correlator, or tracker [2], [18], [19], [36]. This processor has the intuitive appeal of a cross-correlation type bearing estimator and, under certain circumstances, it can rival the performance of the optimum estimator [19]. For these reasons, we have chosen the split-beam tracker as a representative, frozen-design, sub-optimal bearing estimator. In later chapters, we analyze the detailed effects of highly anisotropic noise on the split-beam tracker.

In section 1 of this chapter, we define the split-beam tracker (SBT) and briefly discuss its operation. In section 2, we derive an expression for the SBT output in terms of the array input waveforms and calculate its mean and variance. In section 3, an approximate expression is developed for the variance of bearing estimates generated by the SBT for the particular signal-noise-interference model defined previously in section 2.2.

3.1 - The Split-Beam Tracker

A block diagram of the SBT array processor is shown in figure 3.1. The linear receiving array consists of L , uniformly spaced hydrophones (mutual separation of d feet). The direction of maximum array sensitivity (i.e. its steering angle) is controlled automatically or manually through the selection of the L time-delays, τ_1, \dots, τ_L . The array outputs are then split in half and summed to form the left and right half-beam signals $y_1(t)$ and $y_2(t)$. The left half-beam output $y_1(t)$ is phase shifted 90° by time differentiation. Both signals, $y_1(t)$ and $y_2(t)$, are then passed through identical filters with transfer functions $|H(j\omega)|^2$, multiplied together, and integrated for T seconds. The processor output, $z(\alpha)$, is finally operated upon by a null detector to obtain the target bearing estimate, $\hat{\theta}$.

The 90° phase shift of one split beam output ($y_1(t)$) results in a mean processor output equal to zero when the array is steered exactly on target. In the absence of the 90° phase shift, the correlation, $z(\alpha)$, of the two split-beam signals would be a peak rather than a null when steered at the target. As the array steering angle, α , is swept through 180 degrees by adjusting the delays (τ_1, \dots, τ_L), the mean processor output for a single signal in isotropic noise would increase from near-zero to a positive peak-level just prior to crossing zero at $\alpha = \theta_T$ followed by a negative peak and a subsequent return to zero-level. A nominal, mean SBT output for steering angles in the region of 0 - 180 degrees is shown in figure 3.2.

The task that the estimator (or null detector) must perform to obtain an individual bearing estimate is not quite as simple as might be inferred from figure 3.2. Since the integrator output, $z(\alpha)$, is a random process, the source bearing estimate, $\hat{\theta}$, will be a random variable. Consequently, in practice, the algorithm not only estimates the angular location

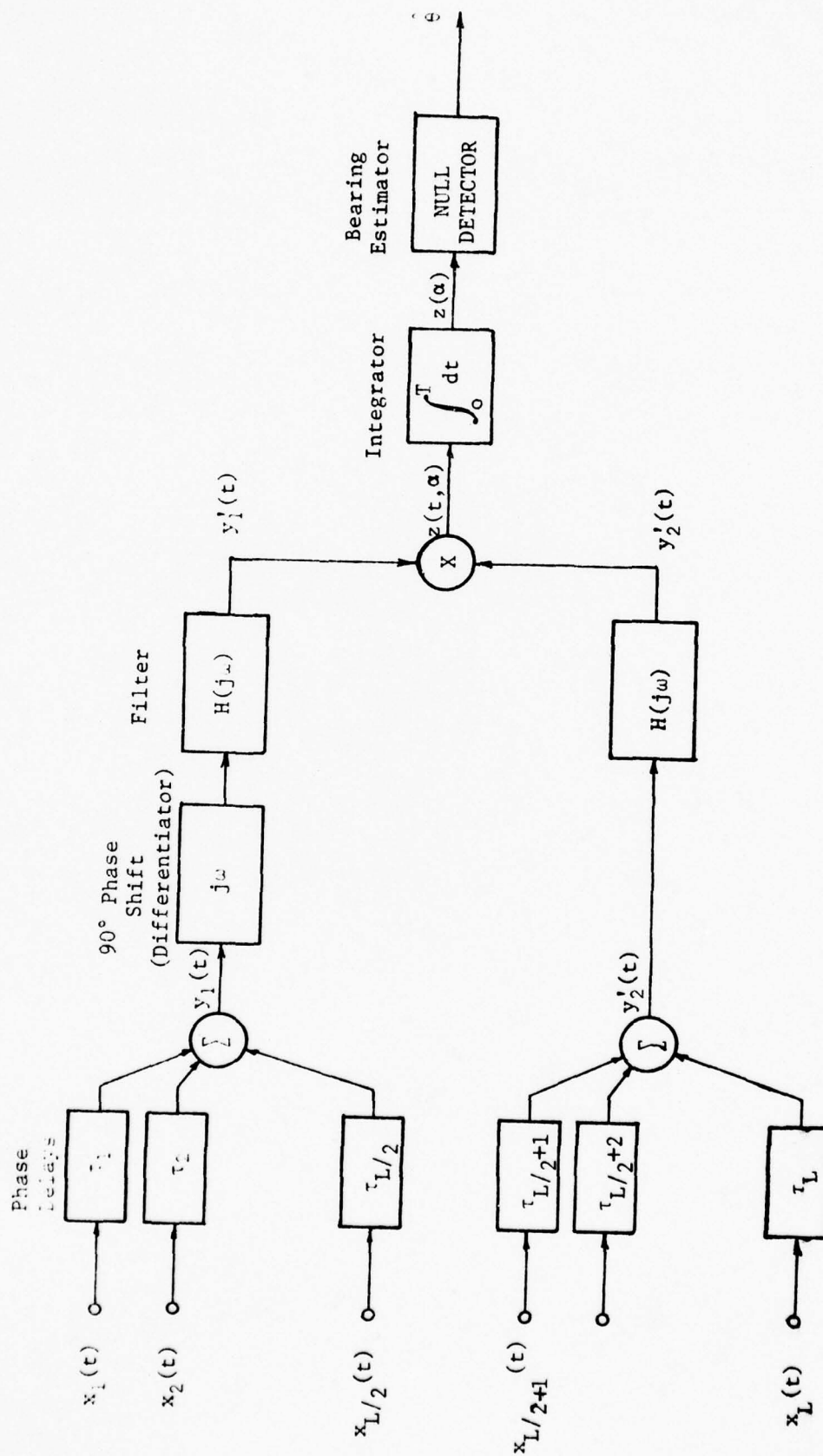


Figure 3.1 - Block Diagram of the Split-Beam Tracker

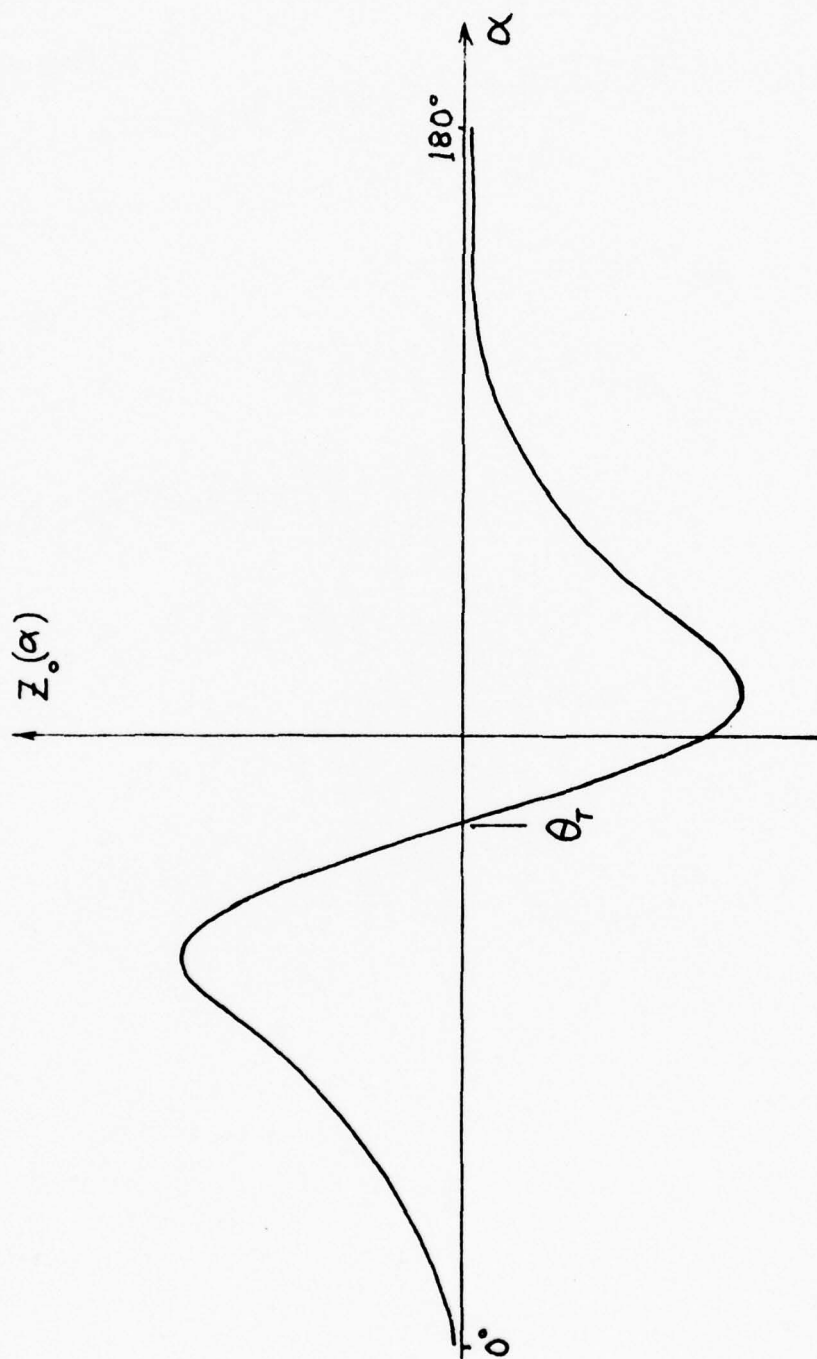


Figure 3.2 - Functional Dependence of Mean SBT Output on Steering Angle

of a particular zero-crossing, it also decides between multiple zero-crossings and discriminates between positive and negative-sloped zero-crossings. In theory, however, we can develop expressions for the SBT output mean and variance and analyze its bearing estimation performance without actually confronting these problems. We demonstrate this in the remaining sections of this chapter.

3.2 - SBT Output Mean and Variance

We again assume that the hydrophone output signals $x_1(t)$, ..., $x_L(t)$ are band-limited, zero-mean, Gaussian processes. The outputs of the two split-beamformers in figure 3.1 are simply

$$y_1(t) = \sum_{\ell=1}^{L/2} x(t + \tau_{\ell}) \quad (3-1a)$$

and

$$y_2(t) = \sum_{\ell=L/2+1}^L x(t + \tau_{\ell}) \quad (3-1b)$$

where the steering delays τ_{ℓ} are given by

$$\tau_{\ell} = (\ell - 1) \cdot \left(\frac{d}{c}\right) \cos \alpha - (L - 1) \cdot \left(\frac{d}{c}\right) \cos \alpha \quad (3-1c)$$

and where d is the hydrophone separation,

c is the speed of sound in the sea, and

α is the steering angle of the array's main response axis.

Since individual SBT bearing estimates are constructed solely on the basis of information contained in a T -second history of $y_1(t)$ and $y_2(t)$, we can characterize them by their Fourier series representations:

$$y_1(t) = \left(\frac{1}{T}\right) \sum_{i=-N}^N Y_i(j\omega_k) e^{j\omega_k t} \quad (3-2a)$$

where

$$Y_i(j\omega_n) = \int_0^T y_i(t) e^{-j\omega_k t} dt \quad i = 1, 2 \quad (3-2b)$$

and $2\omega_N$ is the total bandwidth of the processes. Equations (3-1a, b, c) and (3-2a, b) define the split-beam output signals in terms of the L hydrophone input-signals.

The unsmoothed processor output $z(t, \alpha)$ is

$$\begin{aligned} z(t, \alpha) &= y_1'(t) \cdot y_2'(t) \\ &= \left(\frac{1}{T} \sum_{k=-N}^N Y_1'(j\omega_k) e^{+j\omega_k t} \right) \cdot \left(\frac{1}{T} \sum_{m=-N}^N Y_2'(j\omega_m) e^{+j\omega_m t} \right) \end{aligned}$$

Since the transfer function of a time-differentiator is $H_t(j\omega) = j\omega$, the unsmoothed processor output can be written as

$$z(t, \alpha) = \frac{1}{T^2} \sum_{k=-N}^N \sum_{m=-N}^N (j\omega_k) H(j\omega_k) Y_1(j\omega_k) H(j\omega_m) Y_2(j\omega_m) e^{+j(\omega_k + \omega_m)t} \quad (3-3)$$

The output of the SBT integrator is simply

$$\begin{aligned} z_o(\alpha) &= \int_0^T z(t, \alpha) dt \\ &= \frac{1}{T^2} \sum_{k=-N}^N \sum_{m=-N}^N (j\omega_k) H(j\omega_k) Y_1(j\omega_k) H(j\omega_m) Y_2(j\omega_m) \int_0^T e^{+j(\omega_k + \omega_m)t} dt \quad (3-4) \end{aligned}$$

Now, if the observation time T is much larger than the correlation time of the band-limited input processes, the integral in (3-4) approximates the Kronecker delta; that is

$$\int_0^T e^{+j(\omega_k + \omega_m)t} dt \approx T \delta_{k, -m} \quad (3-5)$$

where T is the observation interval, and

$$\delta_{k, -m} = \begin{cases} 1 & k = -m \\ 0 & k \neq -m \end{cases}$$

Hence, equation (3-4) and (3-5) can be combined to give, as the SBT processor output,

$$z_o(\alpha) = \frac{1}{T} \sum_{k=-N}^N (j\omega_k)^* |H(j\omega_k)|^2 Y_1(j\omega_k) Y_2(j\omega_k) \quad (3-6)$$

where * here denotes the complex conjugate.

From equation (3-6) it is an easy matter to generate the mean SBT output expression:

$$\begin{aligned} z_o(\alpha) &= E \{ z_o(\alpha) \} = \frac{1}{T} \sum_{k=-N}^N (j\omega_k) |H(j\omega_k)|^2 E \{ Y_1(j\omega_k) Y_2^*(j\omega_k) \} \\ &= \frac{1}{T} \sum_{k=-N}^N (j\omega_k) |H(j\omega_k)|^2 T G_{12}(\omega_k) \quad (3-7) \end{aligned}$$

$G_{12}(\omega_k)$ is the cross-power spectral density between $y_1(t)$ and $y_2(t)$ at the frequency ω_k . Since the frequency summation in (3-6) is symmetric about $N = 0$, we can replace $G_{12}(\omega_k)$ by its odd component (ω_k also being an odd function),

$$\begin{aligned} \text{ODD}_{\omega_k} \{ G_{12}(\omega_k) \} &= \text{ODD}_{\omega_k} \left\{ \int_0^T R_{12}(\tau) e^{-j\omega_k \tau} d\tau \right\} \\ &= -j \int_0^T R_{12}(\tau) \sin \omega_k \tau d\tau \\ &= j \text{Im} \{ G_{12}(\omega_k) \} \end{aligned}$$

so that (3-7) becomes

$$z_o(\alpha) = - \sum_{k=-N}^N \omega_k |H(j\omega_k)|^2 \text{Im} \{ G_{12}(\omega_k) \} \quad (3-8)$$

provided the observation interval T is large.

From (3-5), we can also obtain the mean square value of the SBT output:

$$E\{z_o(\alpha)z_o^*(\alpha)\} = \frac{1}{T^2} \sum_{k=-N}^N \sum_{m=-N}^N \left\{ (j\omega_k)(-j\omega_m) |H(j\omega_k)|^2 |H(j\omega_m)|^2 \right. \\ \left. \times E\left[Y_1(j\omega_k)Y_2^*(j\omega_k)Y_1^*(j\omega_m)Y_2(j\omega_m)\right] \right\} \quad (3-9)$$

It is known [18], that the following identity exists for the expectation of the product of complex, Gaussian random variables required by equation (3-9):

$$E\{Y_1(j\omega_k)Y_2^*(j\omega_k)Y_1^*(j\omega_m)Y_2(j\omega_m)\} = E\{Y_1(j\omega_k)Y_2^*(j\omega_k)\} E\{Y_1^*(j\omega_m)Y_2(j\omega_m)\} \\ + E\{Y_1(j\omega_k)Y_1^*(j\omega_m)\} E\{Y_2^*(j\omega_k)Y_2(j\omega_m)\} \\ + E\{Y_1(j\omega_k)Y_2(j\omega_m)\} E\{Y_2^*(j\omega_k)Y_1^*(j\omega_m)\} \quad (3-10)$$

The first term of (3-10) is simply the product of the cross-power spectral density at two different frequencies, i.e.

$$E\{Y_1(j\omega_k)Y_1^*(j\omega_k)\} E\{Y_1^*(j\omega_m)Y_2(j\omega_m)\} = T^2 G_{12}(\omega_k)G_{12}^*(\omega_m) \quad (3-11a)$$

Relative to the second term of (3-10), consider the following:

$$E\{Y_1(j\omega_k)Y_1^*(j\omega_m)\} = \int_0^T dt \int_0^T du E\{y_1(t)y_1(u)\} e^{-j(\omega_k t - \omega_m u)} \\ = \int_0^T d\tau R_{11}(\tau) e^{-j\omega_k \tau} \int_0^T e^{-j(\omega_k - \omega_m)u} du \\ = T G_{11}(\omega_k) \delta_{k,m}$$

assuming T is large. Thus, the second term in (3-10) becomes,

$$E\{Y_1(j\omega_k)Y_1^*(j\omega_m)\} E\{Y_2^*(j\omega_k)Y_2(j\omega_m)\} = T^2 G_{11}(\omega_k)G_{22}(\omega_k)\delta_{k,m} \quad (3-11b)$$

Also consider:

$$\begin{aligned} E\{Y_1(j\omega_k)Y_2(j\omega_m)\} &= \int_0^T dt \int_0^T du E\{y_1(t)y_2(u)\} e^{-j(\omega_k t + \omega_m u)} \\ &= \int_0^T d\tau R_{12}(\tau) e^{-j\omega_k \tau} \int_0^T e^{-j(\omega_k + \omega_m)u} du \\ &\approx T G_{12}(\omega_k)\delta_{k,-m} \end{aligned}$$

Consequently, the last term of (3-10) can be written as,

$$E\{Y_1(j\omega_k)Y_2(j\omega_m)\} E\{Y_2^*(j\omega_k)Y_1^*(j\omega_m)\} = T^2 G_{12}(\omega_k)G_{12}^*(\omega_m)\delta_{k,-m} \quad (3-11c)$$

so that, upon substitution of (3-10) and (3-11a, b, c) into (3-9), the mean square SBT output becomes,

$$\begin{aligned} E\{z_o z_o^*\} &= \frac{1}{T^2} \sum_{k=-N}^N \sum_{m=-N}^N (j\omega_k)(-j\omega_m) |H(j\omega_k)|^2 |H(j\omega_m)|^2 \left\{ T^2 G_{12}(\omega_k)G_{12}^*(\omega_m) \right. \\ &\quad \left. + T^2 G_{11}(\omega_k)G_{22}(\omega_k)\delta_{k,m} + T^2 G_{12}(\omega_k)G_{12}^*(\omega_m)\delta_{k,-m} \right\} \\ &= \left[\sum_{k=-N}^N (j\omega_k) |H(j\omega_k)|^2 G_{12}(\omega_k) \right] \cdot \left[\sum_{m=-N}^N (j\omega_m) |H(j\omega_m)|^2 G_{12}(\omega_m) \right]^* \\ &\quad + \sum_{k=-N}^N \omega_k^2 |H(j\omega_k)|^4 G_{11}(\omega_k)G_{22}(\omega_k) + \sum_{k=-N}^N (-\omega_k^2) |H(j\omega_k)|^4 G_{12}(\omega_k)G_{12}^*(-\omega_k) \end{aligned} \quad (3-12)$$

From equations (3-7) and (3-8) it is obvious that the first term of (3-12) is equivalent to $\bar{z} \cdot \bar{z}^* = \bar{z} \cdot \bar{z}$. Therefore, we can write the following expression for the variance of SBT output:

$$\sigma_{z_o}^2(\alpha) = \sum_{k=-N}^N \omega_k^2 |H(j\omega_k)|^4 \cdot \{G_{11}(\omega_k)G_{22}(\omega_k) - G_{12}^2(\omega_k)\}. \quad (3-13)$$

MacDonald and Schultheiss [19] have previously developed similar expressions for the SBT output mean and variance given by equations (3-8) and (3-13). Discussion of the form of the split-beam filter transfer functions, $|H(j\omega_k)|^2$, is deferred until the end of this chapter. At this point, we can apply the general expressions in (3-8) and (3-13) to the specific signal-noise-interference model of interest. Recall from chapter 2 that the output of the ℓ th hydrophone can be written as

$$x_\ell(t) = s(t - \Delta_\ell) + n_\ell(t) + \sum_{m=1}^M i_m(t - \delta_\ell^m) \quad (3-14)$$

The required spectral densities are, by definition

$$G_{ij}(\omega_k) = \int_{-\frac{T}{2}}^{\frac{T}{2}} R_{ij}(\tau) e^{-j\omega_k \tau} d\tau \quad i, j = 1, 2 \quad (3-15)$$

where $R_{ij}(\tau)$ is the correlation function of $y_i(t)$ and $y_j(t + \tau)$ for $i, j = 1, 2$ and where, without loss of generality, we redefined the observation interval to be $\left[-\frac{T}{2}, \frac{T}{2}\right]$.

The correlation functions in (3-15) are, by definition,

$$R_{ij}(t - u) \triangleq E\{y_i(t) y_j(u)\}. \quad (3-16)$$

From this definition and equations (3-1a) and (3-14) the autocorrelation of $y_1(t)$ is,

$$\begin{aligned}
R_{11}(t) &= E \{ y_1(t) y_1(u) \} \\
&= E \left\{ \sum_{\ell=1}^{\frac{L}{2}} x_{\ell}(t + \tau_{\ell}) \sum_{p=1}^{\frac{L}{2}} x_p(u + \tau_p) \right\} \\
&= \sum_{\ell=1}^{\frac{L}{2}} \sum_{p=1}^{\frac{L}{2}} E \left[\left\{ S(t - \Delta_{\ell} + \tau_{\ell}) S(u - \Delta_p + \tau_p) \right\} + E \{ n_{\ell}(t) n_p(u) \} \right. \\
&\quad \left. \sum_{m=1}^M E \left\{ i_m(t - \delta_{\ell}^m + \tau_{\ell}) i_m(u - \delta_p^m + \tau_p) \right\} \right] \quad (3-17)
\end{aligned}$$

where we have made use of the fact that the signal, noise and all interference processes are mutually independent. We can further simplify (3-17) by writing

$$\begin{aligned}
R_{11}(t) &= \sum_{\ell=1}^{\frac{L}{2}} \sum_{p=1}^{\frac{L}{2}} \left\{ R_{ss}(\tau - \Delta'_{\ell} + \Delta'_p) + R_{nn}(\tau) \delta_{\ell p} \right. \\
&\quad \left. + \sum_{m=1}^M R_{ii}^m(\tau - \xi'_{\ell n} + \xi'_{pm}) \right\} \quad (3-18)
\end{aligned}$$

where $\Delta'_{\ell} = \Delta_{\ell} - \tau_{\ell} = \frac{(\ell - 1)d}{c} (\cos \theta_T - \cos \alpha) + \frac{(L - 1)d}{c} \cos \alpha$

$$\delta_{\ell p} = \begin{cases} 1 & \ell = p \\ 0 & \ell \neq p \end{cases}$$

$$\xi'_{\ell m} = \frac{(\ell - 1)d}{c} [\cos \theta_m - \cos \alpha] + \left[\frac{(L - 1)d}{c} \cos \alpha \right]$$

Substitution of (3-18) into (3-15) yields, after some algebra,

$$\begin{aligned}
G_{11}(\omega_k) &= \sum_{\ell=1}^{\frac{L}{2}} \sum_{p=1}^{\frac{L}{2}} \left\{ S(\omega_k) e^{-j\omega_k(\Delta'_{\ell} - \Delta'_p)} + N(\omega_k) \delta_{\ell p} \right. \\
&\quad \left. + \sum_{m=1}^M I_m(\omega_k) e^{-j\omega_k(\xi'_{\ell n} - \xi'_{pm})} \right\} \quad (3-19)
\end{aligned}$$

where $S(\omega_k)$, $N(\omega_k)$, and $I_m(\omega_k)$ are the signal, noise and m th interference power spectral densities, respectively, at the frequency ω_k . In a similar fashion it is possible to obtain

$$G_{22}(\omega_k) = \sum_{\ell=\frac{L}{2}+1}^L \sum_{p=\frac{L}{2}+1}^L \left\{ S(\omega_k) e^{-j\omega_k(\Delta'_\ell - \Delta'_p)} + N(\omega_k) \delta_{\ell p} \right. \\ \left. + \sum_{m=1}^M I_m(\omega_k) e^{-j\omega_k(\xi'_{\ell m} - \xi'_{pm})} \right\} \quad (3-20)$$

The cross-correlation between $y_1(t)$ and $y_2(t)$ is

$$R_{12}(\tau) = E\{y_1(t)y_2(u)\} \\ = \sum_{\ell=1}^{\frac{L}{2}} \sum_{p=\frac{L}{2}+1}^L \left\{ E\{s(t - \Delta_\ell + \tau_\ell)s(u - \Delta_p + \tau_p)\} + E\{n_\ell(t)n_p(u)\} \right. \\ \left. + \sum_{m=1}^M E\{i_m(t - \delta_\ell^m + \tau_\ell)i_m(u - \delta_p^m + \tau_p)\} \right\} \\ = \sum_{\ell=1}^{\frac{L}{2}} \sum_{p=\frac{L}{2}+1}^L \left\{ R_{ss}(\tau - \Delta'_\ell + \Delta'_p) + \sum_{m=1}^M R_{ii}(\tau - \xi'_{\ell m} + \xi'_{pm}) \right\}.$$

Consequently, the cross-power spectral density $G_{12}(\omega_k)$ is

$$G_{12}(\omega_k) = \sum_{\ell=1}^{\frac{L}{2}} \sum_{p=\frac{L}{2}+1}^L \left\{ S(\omega_k) e^{-j\omega_k(\Delta'_\ell - \Delta'_p)} + \sum_{m=1}^M I_m(\omega_k) e^{-j\omega_k(\xi'_{\ell m} - \xi'_{pm})} \right\} \quad (3-21)$$

where Δ'_ℓ , Δ'_p , $\xi'_{\ell m}$, and ξ'_{pm} are defined as in equation (3-18).

Substituting equation (3-21) into equation (3-8) yields the following expression of the mean SBT output for the signal-noise-interference model of interest:

$$\bar{z}_o(\alpha) = \sum_{k=-N}^N \omega_k |H(j\omega_k)|^2 \left\{ \sum_{\ell=1}^{\frac{L}{2}} \sum_{p=\frac{L}{2}+1}^L \left[S(\omega_k) [\sin \omega_k (\Delta'_\ell - \Delta'_p)] \right] + \sum_{m=1}^M I_m(\omega_k) \sin [\omega_k (\xi'_{\ell m} - \xi'_{pm})] \right\} \quad (3-22)$$

Likewise, the substitution of equations (3-19), (3-20) and (3-21) into (3-13) yields the following expression for the SBT output variances:

$$\begin{aligned} \sigma_{z_o}^2(\alpha) = & \sum_{k=-N}^N \omega_k^2 |H(j\omega_k)|^4 \cdot \left\{ \sum_{p=1}^{\frac{L}{2}} \sum_{q=1}^{\frac{L}{2}} \sum_{r=\frac{L}{2}+1}^L \sum_{s=\frac{L}{2}+1}^L \left[S(\omega_k) e^{-j\omega_k (\Delta'_p - \Delta'_q)} + N(\omega_k) \delta_{pq} \right] \right. \\ & + \sum_{m=1}^M I_m(\omega_k) e^{-j\omega_k (\xi'_{pm} - \xi'_{qm})} \cdot \left[S(\omega_k) e^{-j\omega_k (\Delta'_r - \Delta'_s)} + N(\omega_k) \delta_{rs} \right] \\ & + \sum_{i=1}^M I_i(\omega_k) e^{-j\omega_k (\xi'_{ri} - \xi'_{si})} \left. \right\} - \left\{ \sum_{p=1}^{\frac{L}{2}} \sum_{q=\frac{L}{2}+1}^L S(\omega_k) e^{-j\omega_k (\Delta'_p - \Delta'_q)} \right. \\ & + \sum_{m=1}^M I_m(\omega_k) e^{-j\omega_k (\xi'_{pm} - \xi'_{qm})} \left. \right\}^2 \quad (3-23) \end{aligned}$$

3.3 - Theoretical SBT Bearing Estimation Variance

Figure 3.3 shows that the steering-angle (α) dependence of the theoretical mean SBT output ($\bar{z}_o(\alpha)$ in equation (3-22)) closely follows the conjectured α -dependence of the nominal SBT output in figure 3.2. The effect of a single, weak interference at 45° is evident in figure 3.3 while the effect of the target, located at 90° , is most obvious. The linearity of $\bar{z}_o(\alpha)$ over the small angular region about θ_T , the true source bearing, provides the basis for a theoretical approximation to the bearing variance, σ_{θ}^2 , of the SBT processor. MacDonald and Schultheiss [19] first reported a straightforward approximation to σ_{θ}^2 that assumes $\bar{z}_o(\alpha)$ is linear over

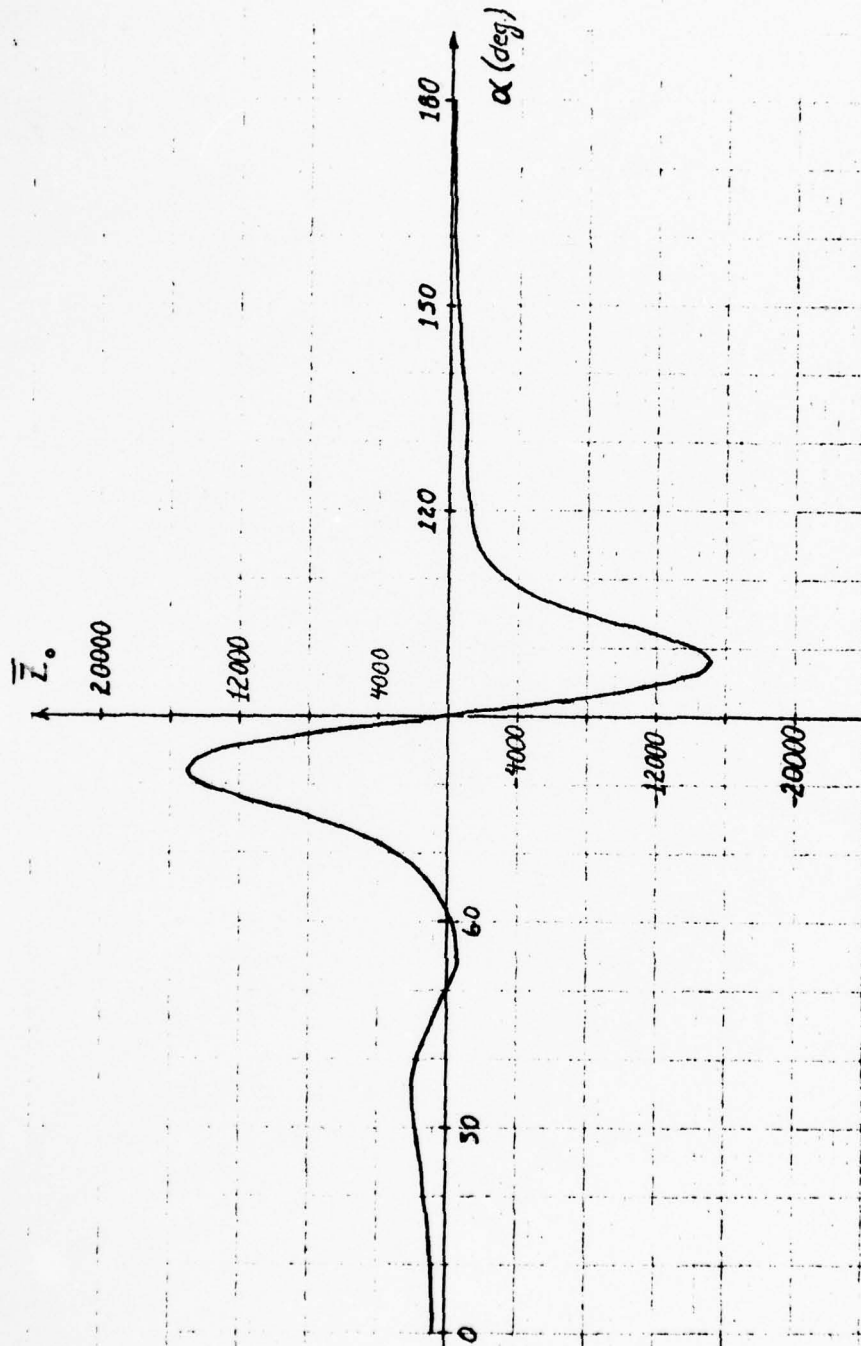


Figure 3.3 - Approximate Theoretical Mean SBT Output (Equation (3-22))

at least an $\alpha = 2\sigma_0$ region about $\hat{\theta}$. The nature of their approximation can be clearly seen in figure 3.4. If $\bar{z}_0(\alpha)$ is linear for α in the region $[\hat{\theta} - \sigma_\theta, \hat{\theta} + \sigma_\theta]$ and if $\sigma_{z_0}(\alpha)$ is relatively insensitive to changes in α over this region, then the following linear, stochastic model of $z_0(\alpha)$ is valid:

$$z_0(\alpha) = A + B\alpha + \zeta \quad \hat{\theta} - \sigma_\theta < \alpha < \hat{\theta} + \sigma_\theta \quad (3-24)$$

where ζ is a zero-mean, Gaussian random variable with variance equal to $\sigma_{z_0}^2$. The estimate $\hat{\theta}$ occurs at the zero-crossing of $z_0(\alpha)$ so that,

$$z_0(\alpha) \Big|_{\alpha=\hat{\theta}} = 0 = A + B\hat{\theta} + \zeta$$

From this model, we obtain

$$\hat{\theta} = -\frac{A}{B} - \frac{\zeta}{B}$$

so that,

$$E\{\hat{\theta}\} = \bar{\theta} = -\frac{A}{B}$$

and

$$\begin{aligned} \text{Var}\{\hat{\theta}\} &= \sigma_\theta^2 = E\left\{\hat{\theta}^2\right\} - \bar{\theta}^2 \\ &= E\left\{\frac{\zeta^2}{B^2}\right\} \\ &= \frac{\sigma_{z_0}^2}{B^2} \end{aligned}$$

Since $B = \frac{\partial z_0}{\partial \alpha}$, we obtain the following expression for the MacDonald-Schultheiss theoretical approximation to the bearing variance of the SBT processor:

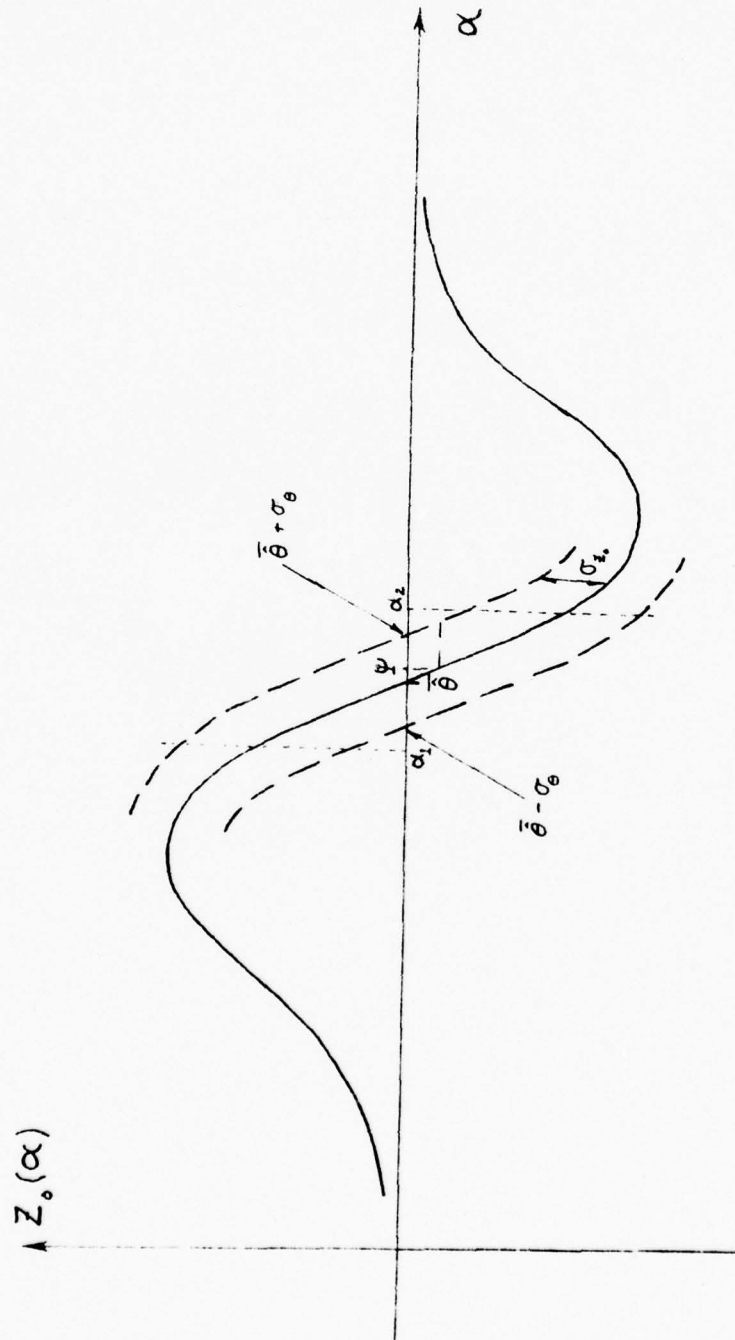


Figure 3.4 - Linear Mean SBT Output and Constant Variance Model

$$\sigma_{\theta}^2 = \frac{\sigma_{z_o}^2(\alpha)}{\left(\frac{\partial \bar{z}_o(\alpha)}{\partial \alpha} \right)^2} \bigg|_{\alpha=\hat{\theta}} \quad (3-25)$$

If $\hat{\theta}$ is unbiased, then $\hat{\theta} = \theta_T$ and (3-25) becomes

$$\sigma_{\theta}^2 = \frac{\sigma_{z_o}^2(\alpha)}{\left(\frac{\partial \bar{z}_o(\alpha)}{\partial \alpha} \right)^2} \bigg|_{\alpha=\theta_T} \quad (3-26)$$

If $\hat{\theta}$ is biased, but only slightly, then equation (3-26) is still a good approximation to σ_{θ}^2 . Otherwise, equation (3-25) is more accurate. If, however, one can assume that $\bar{z}_o(\alpha)$ is linear and $\sigma_{z_o}^2(\alpha)$ is almost constant over a larger angular region about $\hat{\theta}$, then equation (3-26) is again valid.

If, for example, the true target were located at the bearing ψ in figure 3.4, then (3-26) is equally as valid as (3-25) since the assumptions are true for $\alpha = \alpha_1 \leq \alpha_2$.

The error metric defined in (3-26), although not as general as that in (3-25), is somewhat simpler to interpret since it decouples the variance and bias errors. Equation (3-26) is the approximate theoretical SBT variance metric examined in chapters 5 and 6. The numerator and denominator of equation (3-26) exist in the form of equations (3-22) and (3-23). Equation (3-22) must be differentiated with respect to α and both equations then evaluated at $\alpha = \theta_T$. Recalling the definitions of Δ'_ℓ and $\xi'_{\ell n}$, the derivative of the mean SBT output can be written as,

$$\begin{aligned} \frac{\partial \bar{z}_0}{\partial \alpha} = & \sum_{k=-N}^N \omega_k |H(j\omega_k)|^2 \left\{ \sum_{\ell=1}^{\frac{L}{2}} \sum_{p=\frac{L}{2}+1}^L \left[\omega_k \frac{(\ell-p)d}{c} (\sin \alpha) S(\omega_k) \cos [\omega_k (\Delta'_\ell - \Delta'_p)] \right. \right. \\ & \left. \left. + \sum_{m=1}^M \omega_k \frac{(\ell-p)d}{c} \sin \alpha I_m(\omega_k) \cos [\omega_k (\xi'_{\ell n} - \xi'_{pm})] \right] \right\} \quad (3-27) \end{aligned}$$

To evaluate (3-27) at $\alpha = \theta_T$, note that

$$\Delta'_\ell - \Delta'_p = 0 \quad (3-28a)$$

and

$$\xi'_{\ell n} - \xi'_{pn} = \frac{(\ell-p)d}{c} [\cos \theta_m - \cos \theta_T] \quad (3-28b)$$

so that equation (3-27) becomes,

$$\begin{aligned} \frac{\partial \bar{z}_0}{\partial \alpha} \bigg|_{\alpha = \theta_T} = & \frac{d \sin \theta_T}{c} \sum_{k=-N}^N \omega_k^2 |H(j\omega_k)|^2 \left\{ \sum_{\ell=1}^{\frac{L}{2}} \sum_{p=\frac{L}{2}+1}^L [(\ell-p) S(\omega_k) \right. \\ & \left. + (\ell-p) \sum_{m=1}^M I_m(\omega_k) \cos [(\ell-p)\Omega]] \right\} \quad (3-29) \end{aligned}$$

where we have defined $\Omega = \omega_k \frac{d}{c} [\cos \theta_m - \cos \theta_T]$. As shown in appendix C, by expressing the cosine term in (3-29) as a sum of complex exponentials, it is possible to evaluate both double summations over the hydrophone indices (i.e. equations (C-1) and (C-8)) and obtain the following expression for the denominator of (3-26)

$$\begin{aligned} \frac{\partial \bar{z}_0}{\partial \alpha} \bigg|_{\alpha = \theta_T} = & \frac{-d \sin \theta_T}{c} \sum_{k=-N}^N \omega_k^2 |H(j\omega_k)|^2 \left\{ \frac{3}{8} S(\omega_k) - \sum_{m=1}^M I_m(\omega_k) C_m(\omega_k) \right. \\ & \left. \times \left[\sin(L \frac{\Omega}{2}) \cot(\frac{\Omega}{2}) - \frac{1}{2} \sin(L \frac{\Omega}{2}) \cot(\frac{L}{2} \cdot \frac{\Omega}{2}) - \frac{1}{2} \cos(L \frac{\Omega}{2}) \right] \right\} \quad (3-30) \end{aligned}$$

where

$$C_m(\omega_k) = \frac{\sin^2\left(\frac{L}{2} - \frac{\Omega}{2}\right)}{\sin^2\left(-\frac{\Omega}{2}\right)}$$

and

$$\Omega = \omega_k \frac{d}{c} \left[\cos \theta_m - \cos \theta_T \right]$$

Using the results of appendix C and equations (3-28a, b), it can be shown that

$$\begin{aligned} \sigma_{z_o}^2(\alpha) \Big|_{\alpha=\theta_T} &= \sum_{k=-N}^N \omega_k^2 |H(j\omega_k)|^4 \left\{ \frac{L^2}{4} N^2(\omega_k) + \frac{L^3}{4} S(\omega_k) N(\omega_k) \right. \\ &\quad + LN(\omega_k) \sum_{m=1}^M I_m(\omega_k) C_m(\omega_k) + L^2 S(\omega_k) \sum_{m=1}^M I_m(\omega_k) C_m(\omega_k) \sin^2\left(\frac{L}{2} - \frac{\Omega}{2}\right) \\ &\quad \left. + 4 \left[\sum_{m=1}^M I_m(\omega_k) C_m(\omega_k) \sin\left(\frac{L}{2} - \frac{\Omega}{2}\right) \right] \cdot \left[\sum_{n=1}^M I_n(\omega_k) C_n(\omega_k) \cos\left(\frac{L}{2} - \frac{\Omega}{2}\right) \right] \right\} \end{aligned} \quad (3-31)$$

The final expression for the approximate, theoretical SBT bearing variance is given by equation (3-26) with its numerator and denominator defined explicitly by equations (3-31) and (3-30), respectively. This performance metric will be evaluated numerically in chapters 5 and 6.

The bearing variance metric presented above is expressed in terms of the filter transfer functions, $|H(j\omega_k)|^2$, which are as yet unspecified. Ideally, one should like to select that filter transfer function which minimizes the bearing estimation variance. Since the sub-optimal SBT processor is designed to discriminate only against isotropic, Gaussian noise, $|H(j\omega_k)|^2$ cannot be selected by minimizing the above bearing variance expressions (equations (3-26), (3-30), and (3-31)) which pertain to a highly anisotropic

noise model. However, if we let $I_m(\omega_k) = 0$ for $m = 1, \dots, M$ at all frequencies, then our bearing variance expressions will reflect a noise model which is isotropic. Under this isotropic assumption (3-31) and (3-30) can be substituted into (3-26) to obtain:

$$\sigma_{\theta}^2 = \frac{\sum_{k=-N}^N \omega_k^2 |H(j\omega_k)|^4 \left(\frac{L}{4}\right)^2 (N^2(\omega_k) + LS(\omega_k)N(\omega_k))}{\frac{d \sin \theta_T}{c} \left\{ \sum_{k=-N}^N \omega_k^2 |H(j\omega_k)|^2 \left(\frac{L}{8}\right) S(\omega_k) \right\}^2} \quad (3-32)$$

It is known [18], [19] that the bearing variance in (3-32) can be minimized through a variational calculus approach and results in the following filter function:

$$|H(j\omega_k)|^2 = \frac{\frac{S(\omega_k)}{N^2(\omega_k)}}{\left(1 + \frac{LS(\omega_k)}{N(\omega_k)}\right)} \quad (3-33)$$

Use of this filter transfer function in the SBT processor shown in figure 3.1 will optimize its bearing estimation performance for a unidirectional, plane wave, Gaussian signal in isotropic, Gaussian noise. In the remainder of this research, when a specific form of the SBT filter coefficients is required, the filter defined by (3-33) will be employed.

CHAPTER IV

DIGITAL SBT SIMULATION

This chapter describes a digital computer simulation which was developed to provide additional measures of the performance of the SBT in highly anisotropic noise environments. A real-time array processor can be implemented in either the time or frequency domains. Traditionally, sonar processors have been implemented in the temporal domain. However, with the current, sophisticated digital technology, sonar processors are also easily implemented in the frequency domain.

Discrete models of some temporal operations, such as differentiation, are unavoidably noisy procedures. However, the equivalent frequency domain operation is complex multiplication and easily modeled. There are also problems associated with digital implementations or simulation models of array beam steering. Discrete temporal beam steering requires extremely high sampling rates or the use of complex interpolation algorithms. In the frequency domain, beam steering is also a simpler operation. At each frequency, the input is simply multiplied by a complex-exponential weighting. The advantages of frequency domain implementations (or simulations) are often completely negated by the added cost and complexity of the time-frequency transformation. If the input process spectra vary considerably with frequency and exist over a large bandwidth, then even the computational speed of FFT algorithms may fall short of making frequency domain processing attractive.

In section 4.1 below, we discuss the reasons for developing a frequency domain simulation and describe its operation. Section 4.2

describes the methodology employed to generate samples of the desired input, signal-noise-interference processes at each hydrophone. The last section develops the digital bearing estimation algorithm.

4.1 - Digital SBT Simulation

A block diagram of the complete frequency-domain SBT simulation is shown in figure 4.1. The simulation performs three basic functions: generation and FFT processing of the input data sequences, application of the SBT algorithm, and extraction of the source bearing estimate from the processor output. The SBT as configured in figure 4.1 is conceptually capable of processing recorded field data instead of the T-second long simulated time sequences, $x_\ell(n\Delta t)$, $\ell=1, \dots, L$. However, for the purpose of emulating the SBT processor, observe that if the frequency domain characterization of the hydrophone outputs could be synthesized directly, then the costly requirement for a Fourier transformer is eliminated. Indeed, the linearity of the Fourier transform assures that the Fourier coefficients will be Gaussian random variables when the hydrophone outputs are Gaussian processes. Consequently, the direct generation of the frequency-domain random deviates is justified. In the next section, we describe a methodology for generating the Gaussian deviates, $X_\ell(j\omega_k)$, $k=0, 1, \dots, N-1$, which possess the desired statistical properties.

The hydrophone output sequences of random deviates stimulate the SBT array processing algorithm which generates an output random deviate corresponding to the chosen steering angle, α . If the steering angle is subsequently incremented and the SBT algorithm reapplied a total of ISTEER times, then the processor output sequence $z_o(1), z_o(2), \dots, z_o(\text{ISTEER})$ is generated. The simulated bearing estimates are then formed from these ISTEER deviates.

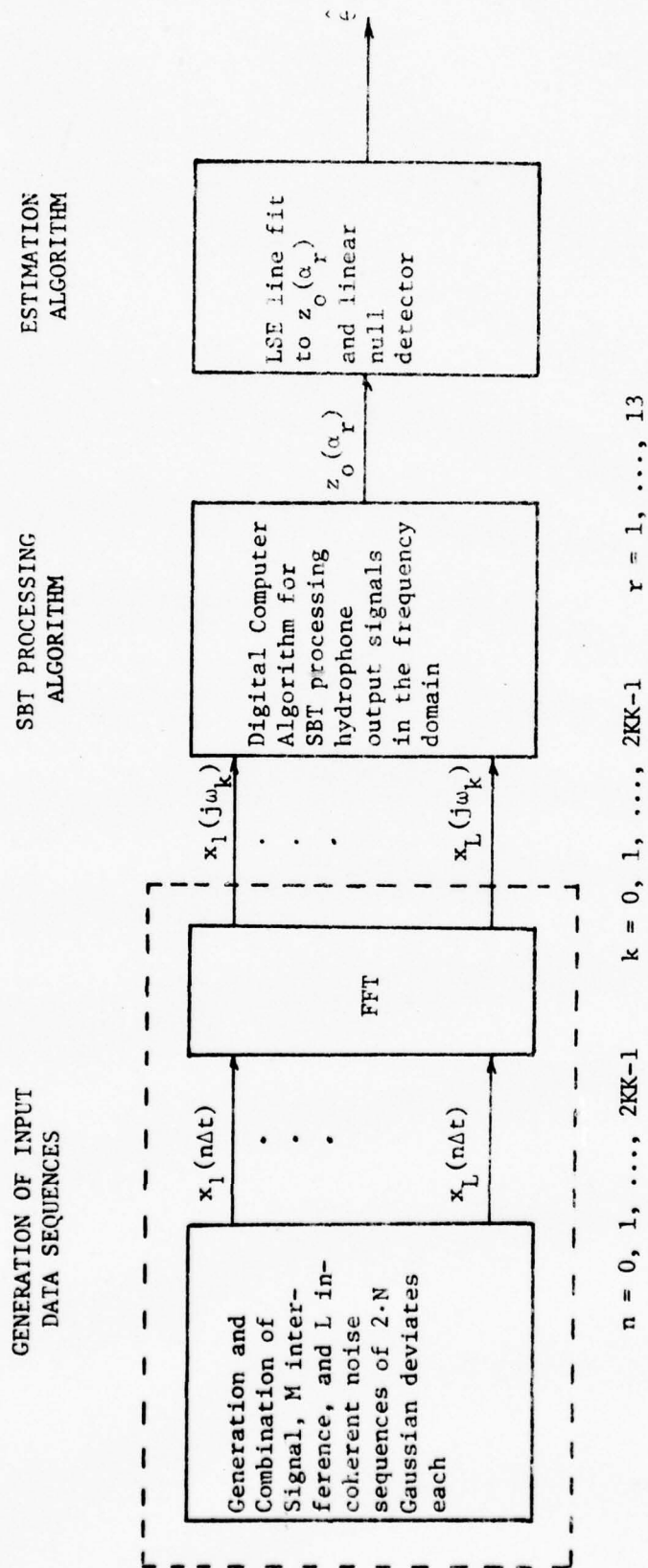


Figure 4.1 - Frequency Domain SBT Simulation

The SBT processing algorithm is simply the output expression developed in chapter 3 for arbitrary hydrophone output waveforms and need not be discussed in detail again. Specifically, the SBT algorithm is defined by equations (3-1) through (3-3) and equation (3-6) where the filter transfer function $|H(j\omega_k)|^2$ is defined in equation (3-33). Recall that the utility of the frequency domain processor-simulation arises from the ease of performing the following operations in the frequency domain: beamsteering, differentiation (or 90° relative phase shift), filtering and integration.

The third function performed by the simulation is the actual bearing estimation algorithm. We utilize a linear, null-detection algorithm which closely follows the one developed by Witt [36]. That is, the bearing estimate is the angular location of the steepest, negatively-sloped, zero-crossing of the linear regression of the output sequence, $z_0(1), \dots, z_0(\text{ISTEER})$, on the steering angle sequence $\alpha_1, \dots, \alpha_{\text{ISTEER}}$. Our algorithm is detailed in section 4.3.

4.2 - Generation of Input Random Deviates

Before discussing the direct generation of the frequency deviates, $x_\ell(j\omega_k)$, it is of interest to outline the steps required to generate the time sequences, $x_\ell(n\Delta t)$. Since the noise model of interest contains M-directional interferences and an uncorrelated, isotropic component, a total of $M + L + 1$ independent sequences of Gaussian random deviates are required. At each hydrophone, the $M+1$ sequences associated with the target and interferences must be time delayed in proportion to their respective bearings. As mentioned earlier, this time delay insertion requires high sample rates or interpolation between every adjacent point in each of the L hydrophone

time sequences. The $M + L + 1$ sequences are discrete samples of white, Gaussian noise processes and must each be filtered to obtain the desired spectral characteristics. If, for example, one restricts his attention to low-pass band-limited, white Gaussian processes, then the spectral shaping is easily accomplished by a linear-phase, FIR digital filter [24]. Finally, the simulated output signal at each hydrophone is the sum of an independent noise sequence and $M + 1$ properly delayed, propagating (directional) sequences. As indicated in figure 4.1, the input time sequences must also be pre-processed by the Fourier transformer in order to stimulate a frequency-domain SBT algorithm. If one intends to stimulate a time domain algorithm, it has been noted [36] that the input time sequences must be of length greater than T to permit truncation of noisy end-point values generated by the time-differentiation operation.

If, as is the case here, one can define the first and second order signal-plus-total-noise statistics, then it is possible to generate the required input random deviates through a transformation of zero-mean, unit variance random deviates (e.g. [4] and [23]). Our approach closely parallels that of Franklin [10]. By assumption, the hydrophone outputs are zero-mean, Gaussian random processes. By design, the hydrophone output $X_\ell(j\omega_k)$ at frequency ω_k and the output $X_\ell(j\omega_m)$ at frequency ω_m are independent for $\omega_k \neq \omega_m$. Consequently, the array response is completely specified by the KK , $L \times L$ dimensional signal-plus-total-noise covariance matrices, $K_{\text{--}SN}$. In other words, for $k = 0, 1, \dots, KK-1$, we have at the frequency ω_k

$$\vec{X} = \left[X_1(j\omega_k), X_2(j\omega_k), \dots, X_L(j\omega_k) \right]^T$$

$$E \left\{ \vec{X} \right\} = \vec{0}$$

and

$$E \left\{ \vec{X} \vec{X}^* \right\} = \underline{K}_{SN}(\omega_k)$$

The covariance matrix $\underline{K}_{SN}(\omega_k)$ is not only Hermitian, it is also Toeplitz and is defined in equation (3-20) as,

$$\begin{aligned} \underline{K}_{SN}(\omega_k) &= TS(\omega_k) \vec{a}(\omega_k) \vec{a}^*(\omega_k) + TN(\omega_k) \underline{I} + T \sum_{m=1}^M I_m(\omega_k) \vec{b}_m(\omega_k) \vec{b}_m^*(\omega_k) \\ &= TS \vec{a} \vec{a}^* + \underline{K}_N \end{aligned} \quad (4-1)$$

where S, N, and I are, respectively, the signal, noise, and interference power spectral densities at ω_k , $\vec{a}(\omega_k)$ and $\vec{b}_m(\omega_k)$ are the signal and m th interference phase delay vectors, T is the observation time interval, and \underline{K}_N is the noise plus interference covariance matrix at ω_k . Since both the propagating and non-propagating components of the received waveforms are by assumption homogeneous, the signal-plus-total-noise covariance matrix in (4-1) is a Toeplitz matrix. For simplicity, we drop the frequency index for the remainder of the derivation.

Generation of the desired complex vector Gaussian deviate \vec{X} first requires the generation of an L dimensional, complex vector Gaussian variable \vec{z} which has zero mean and unit variance. The vector \vec{z} is easily constructed from two real, Gaussian, vector random variables with zero mean and unit variance. If the probability density functions of the real, independent, L-dimensional vectors \vec{u} and \vec{v} are $N(\vec{0}, \underline{I})$, then by defining

$$\vec{z} = \left(\frac{1}{\sqrt{2}} \right) \left[\vec{u} + j\vec{v} \right] \quad (4-2)$$

it is apparent that

$$E \left\{ \begin{matrix} \vec{z} \\ \vec{z} \end{matrix} \right\} = \vec{0}$$

and
$$E \left\{ \begin{matrix} \vec{z} & \vec{z}^* \\ \vec{z} & \vec{z} \end{matrix} \right\} = \underline{I}$$

A standard DEC system KL-10 library subroutine was used to generate the zero-mean, unit variance Gaussian elements of the vector random variables \vec{u} and \vec{v} .

In general, the vector \vec{X} is related to the vector \vec{z} by the following transformation:

$$\vec{X} = \underline{C} \vec{z} + \vec{u} \quad (4-3)$$

where \underline{C} is a unique, $L \times L$ lower-triangular, deterministic, complex matrix such that

$$\underline{K}_{SN} = E \left\{ \begin{matrix} \vec{X} & \vec{X}^* \end{matrix} \right\} = \underline{C} \cdot \underline{C}^* \quad (4-4)$$

and, by assumption, $\vec{\mu} = E \left\{ \begin{matrix} \vec{X} \end{matrix} \right\} = \vec{0}$. Since \underline{K}_{SN} is known (see equation (4-1)), equation (4-4) can be solved recursively (Franklin [10], p. 208) for the elements of the transformation matrix \underline{C} .

The signal, noise, and interference power spectral densities must be defined at each frequency in order to completely specify \underline{K}_{SN} . To facilitate numerical evaluation of both the theoretical and simulation error measures, we make the simplifying assumption that the spectral shapes of all processes are identical, i.e.

$$S(\omega), N(\omega), I_m(\omega) = (S, N, I_m) \cdot G(\omega) \quad (4-5)$$

where α , N and I_m in (4-5) are constants and $G(\omega)$ is a normalized power spectral density function. In the remainder of this study, we shall assume an observation interval of $T = 0.128$ seconds and a sampling frequency of 250 Hz. Consequently, the one-sided spectrum $G(\omega)$ is defined by 16 samples at $\omega_k = \frac{2\pi}{T} k$, $k = 0, 1, 2, \dots, 15$. Furthermore, we require the low pass spectral sequence, $G(\omega_k)$ to roll-off at 40 dB/octave and define its 12 dB down frequency to be $\omega_{13} = \left(\frac{2\pi}{T}\right) \cdot 13 = 2\pi(101.5 \text{ Hz})$. Figure 4.2 illustrates the idealistic spectral shape of signal, noise and interference employed in this study. Since the parameters $\frac{S}{N}$, $\frac{I_m}{N}$, θ_T , M , and θ_m ($m = 1, \dots, M$) are investigated as variables within this study, we have completely specified K_{SN} and are able to use the above methodology (equations (4-1), (4-4), (4-3) and (4-2)) to transform independent, zero-mean, unit-variance Gaussian deviates into the desired, complex, vector Gaussian deviates $X(j\omega_k)$ ($k = 0, 1, \dots, 15$) from the distribution $N(\vec{0}, K_{SN}(\omega_k))$.

4.3 - Simulated Estimation Algorithm

If, as in chapter 3, we make the assumption that the mean SBT output is a linear function of steering angle, (around $\hat{\theta}$), then it seems reasonable to form an LSE straight line fit to several output points which encompass a zero crossing and calculate the bearing estimate from this line. The simulation program calculates "ISTEER" SBT output deviates centered around the true target bearing, from which the line fit is computed. In the baseline numerical evaluation that follows, the parameter ISTEER is equal to 13. For simplicity, let $P = \text{ISTEER}$ in the following derivation.

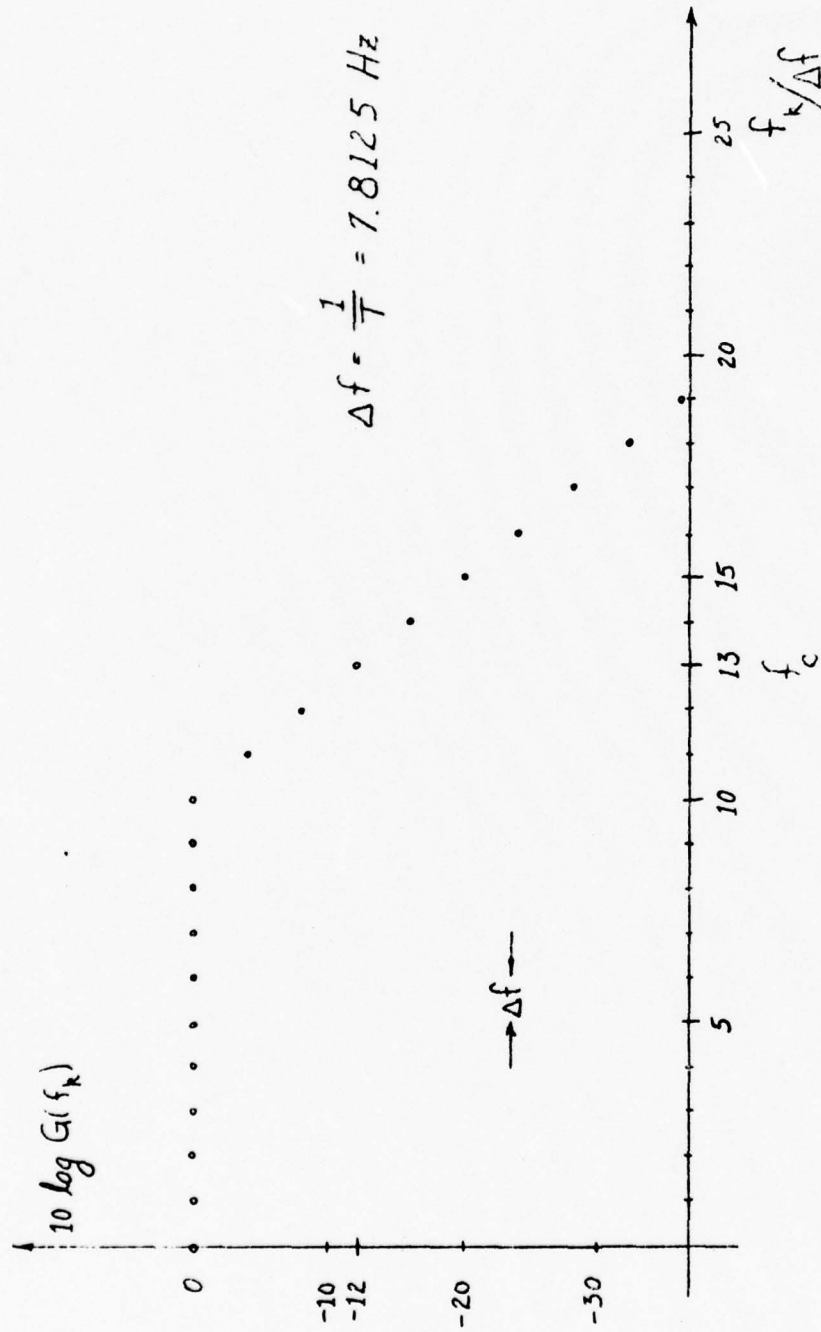


Figure 4.2 - Normalized, Signal, Noise, and Interference Power Spectral Densities

Figure 4.3 illustrates the estimation procedure for P hypothetical simulation output values. The LSE line is defined by

$$z_{LSE}(\alpha) = A - B\alpha \quad (4-6)$$

The bearing estimate, $\hat{\theta}$, satisfies

$$z_{LSE}(\hat{\theta}) = 0$$

and is clearly,

$$\hat{\theta} = \frac{A}{B} \quad (4-7)$$

The coefficients A and B are chosen to minimize the mean-square-error,

$$\begin{aligned} \text{MSE} &= \frac{1}{P} \sum_{i=1}^P \left(z_i - z_{LSE}(\alpha_i) \right)^2 \\ \text{MSE} &= \frac{1}{P} \sum_{i=1}^P \left(z_i - (A - B\alpha_i) \right)^2 \end{aligned} \quad (4-8)$$

By setting the derivatives, with respect to A and B , of (4-8) equal to zero, A and B are easily found and, upon substitution into (4-7) yield,

$$\hat{\theta} = \frac{\sum z_j \sum \alpha_i - \sum z_j \alpha_j \sum \alpha_i}{\sum z_j \sum \alpha_i - P \sum z_j \alpha_j} \quad (4-9)$$

where all summations range from 1 to P . Since we are interested in target tracking applications, as long as the sector over which the beam is swept is not unrealistically small, we need not be unduly concerned with multiple zero-crossings of the simulation output. Consequently, the simulation program uses all of the ISTEER output values to calculate $\hat{\theta}$ and requires only that the slope of $z_{LSE}(\alpha)$ be negative.

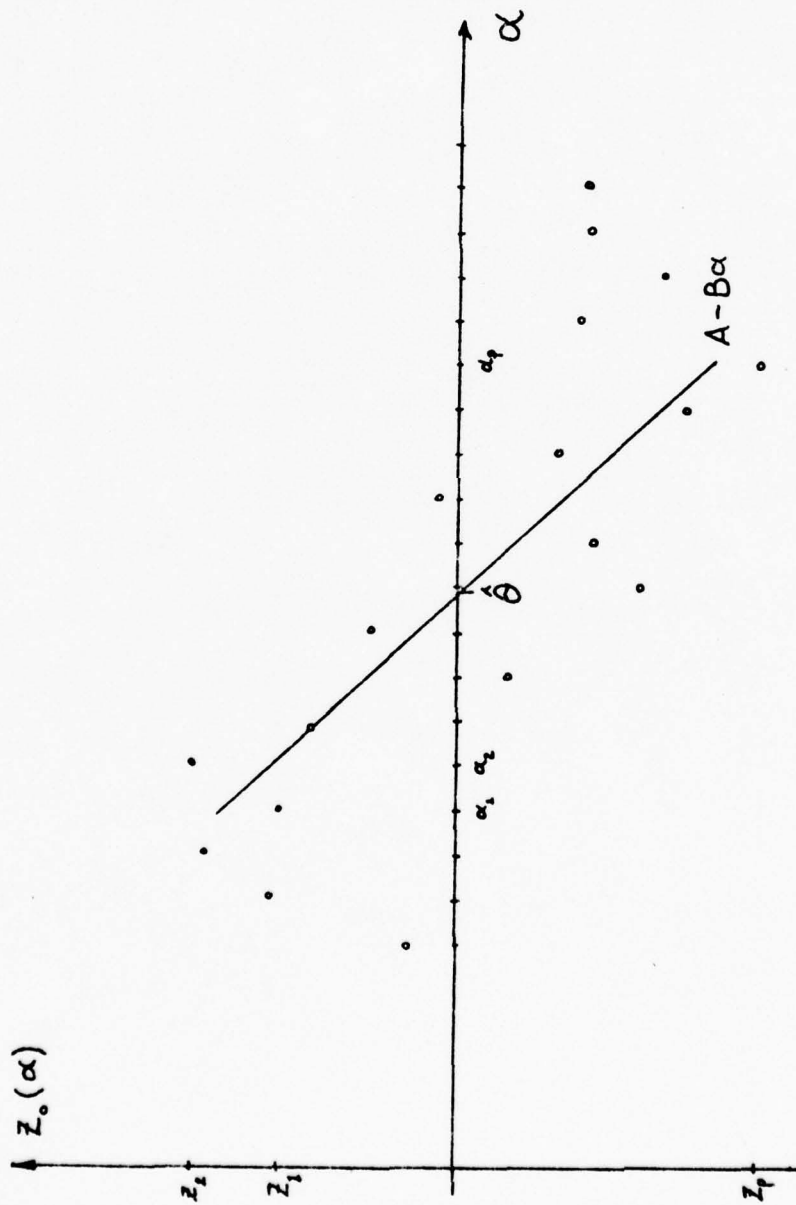


Figure 4.3 - Discrete Bearing Estimation by LSE Line Fit

Previous studies [e.g., 36] have successfully employed similar techniques for estimating source bearing from sampled SBT output values. As discussed in chapter 5, there are potential problems with this type of algorithm. It is desirable to have a large number of beam positions, ISTEER, as well as having the angular beam-sweep region large relative to the bearing standard deviation. Otherwise, it is likely that LSE lines with very small slopes will occur, resulting in unplausible bearing estimates. In any event, this problem requires larger simulation sample sizes.

For every parametric combination (SNR, M , L , θ_m , etc.) of interest, the simulation must be exercised a total of $ISTEER \times J_{REP}$ times, where J_{REP} is the number of estimates per sample and, recall, ISTEER is the number of beam positions per estimate. Based on these samples, statistical measures of the performance of the SBT array processor are defined in the next chapter.

CHAPTER V

NUMERICAL RESULTS - BASELINE

This chapter presents the results of the numerical analysis of bearing estimation in the presence of multiple, interfering noise sources. The Cramer-Rao (CR) bound derived in chapter 2 is the performance metric for examining the effects of such interference on the optimal (ML) estimator, which is assumed to be unbiased. For the sub-optimal split-beam tracker (SBT), bias as well as standard deviation of error is evaluated. The performance of the SBT is presented in terms of both theoretical measures of error and statistical measures of the simulated SBT performance. The SBT performance metrics are described in detail in the following section. Section 2 lists the baseline values of the fixed and variable array, processor, signal, noise and interference parameters. Section 3 presents and discusses the baseline results in terms of the standard deviation-type error measures while the last section contains the baseline results in terms of the bias error metrics.

5.1 - SBT Performance Metrics

One theoretical measure of the SBT performance is the approximate expression of the standard deviation of the bearing estimate derived in chapter 3. The approximation arose from the assumptions of long observation interval and linear behavior (as a function of steering angle) of the SBT output. Another theoretical measure of the SBT performance is the estimation bias or expected value of the bearing estimation error. It is reasonable to assume that the SBT bias error, unlike that of the maximum likelihood estimator, will be significant for many target-to-interference

separations. The bias error, B , is defined as

$$B \triangleq E\{\hat{\theta}\} - \theta_T = \bar{\hat{\theta}} - \theta_T \quad (5-1)$$

where $E\{\cdot\}$ denotes the statistical expectation, $\hat{\theta}$ denotes the bearing estimate and θ_T is the true value of the target bearing. Assuming the probability density function of the SBT output, z_o , is symmetric about its mean, the expected value of the bearing estimate can be calculated from:

$$E\{z_o(\alpha)\} \Big|_{\alpha=\bar{\hat{\theta}}} = \bar{z}_o(\alpha) \Big|_{\alpha=\bar{\hat{\theta}}} = 0 \quad (5-2)$$

where $\bar{z}_o(\alpha)$ is the mean SBT output derived in chapter 3. The exact solution of equation (5-2) for $\bar{\hat{\theta}}$ is mathematically intractable. A good approximation of $\bar{\hat{\theta}}$ is obtained for forming a least-square-error (LSE) straight line fit to p values of $\bar{z}_o(\alpha)$ and solving the result for $\bar{\hat{\theta}}$ according to equation (5-2). This algorithm is the same one employed to obtain bearing estimates from the simulated SBT output which was described in chapter 4. The bias error in equation (5-1) above and the standard deviation of the bearing estimate given by equation (3-26) are the theoretical measures of SBT performance which are presented in this chapter. They both represent approximations to ensemble averages of bias error and estimation standard deviation assuming a linearity of the SBT output with respect to steering angle, α .

The relevant statistical measures of the performance of the simulated SBT processor are simply the sample mean and standard deviation of the estimated bearings. Samples of sizes from 20 to 60 replications were generated for the various parametric combinations. Consistent with the previous theoretical measure, the sample bias error is presented in this

chapter rather than the sample mean of the estimated bearing. With the i th bearing estimate, $\hat{\theta}_i$, generated by the simulation as described in chapter 4, the sample bias error is simply

$$B_s = \frac{1}{N} \cdot \sum_{i=1}^N (\hat{\theta}_i - \theta_T) \quad (5-3)$$

where N is the sample size. The inherent, statistical uncertainty in the sample bias is defined by the confidence belt calculated for each sample bias estimate. If instead of a single sample of size N , a large number of samples of size N are generated, then one would expect the true population bias to fall within the sample confidence intervals for $(1 - \alpha)$ percent of the samples. The confidence intervals presented in these results are computed from [18]

$$B_s - t_{N-1, \frac{\alpha}{2}} \sqrt{\frac{\sigma_{\hat{\theta}}^2}{N}} \leq B \leq B_s + t_{N-1, \frac{\alpha}{2}} \sqrt{\frac{\sigma_{\hat{\theta}}^2}{N}} \quad (5-4)$$

where, B_s is the sample bias computed in equation (5-3),

B is the true, or population bias,

$t_{N-1, \frac{\alpha}{2}}$ is the students t -statistic for $N-1$ degrees of freedom and a significance level of α

N is the number of replications per sample (the sample size, e.g. 20)

α is the level of significance and was chosen to be 0.10 for this investigation,

$\sigma_{\hat{\theta}}^2$ is the sample variance of the estimated bearing as described below.

⁴The simulation estimates $\hat{\theta}_i$ and the theoretical mean bearing estimate, θ , described previously are computed using the same number of beam positions for each LSE line fit.

The sample variance of the estimated bearing is [8],

$$\sigma_{\hat{\theta}}^2 = \frac{1}{N-1} \left\{ \sum_{i=1}^N \hat{\theta}_i^2 - \frac{1}{N} \left(\sum_{i=1}^N \hat{\theta}_i \right)^2 \right\} \quad (5-5)$$

The statistical nature of the sample variance or the sample standard deviation, $\sigma_{\hat{\theta}}$, is also reflected by its confidence interval. This confidence interval is calculated from the following expression [8]:

$$\sigma_{\hat{\theta}} \sqrt{\frac{(N-1)}{\chi^2_{N-1, 1-\frac{\alpha}{2}}}} \leq \sigma_{\hat{\theta}} \leq \sigma_{\hat{\theta}} \sqrt{\frac{(N-1)}{\chi^2_{N-1, \frac{\alpha}{2}}}} \quad (5-6)$$

where $\chi^2_{N-1, \frac{\alpha}{2}}$ is the chi-squared statistic for $N-1$ degrees of freedom and a significance level of α ,

N is the number of estimates per sample and,

α is the significance level, equal to 0.10.

The sample variance computed in equation (5-5) reflects the random variation of bearing estimates formed from p values of the simulation output at corresponding values of the array steering angle about the target bearing. In other words, the variance in (5-5) is based on p observations of T seconds of data. However, the approximate, theoretical SBT bearing variance described earlier and the Cramer-Rao variance bound derived in chapter 2 are based on only T seconds of observed data. To facilitate a direct comparison between the three variance (or standard deviation) measures, the quantity

$$\sigma_{\hat{\theta}, T}^2 = p \times \sigma_{\hat{\theta}}^2 \quad (5-7)$$

is presented as an approximation to the T -second bearing variance of the simulated SBT processor. This type of approximation, suggested by Swerling [28] and adopted by Witt [36], implies that the angular region

over which the LSE line fit is made is small enough to assume the points in the line fit are p independent observations of statistically identical data.

5.2 - Baseline Parameter Values

The results presented in this chapter pertain to a baseline set of array, processor, signal and noise parameters. The baseline set of parameters is listed in table 5.1. The baseline values in table 5.1 allow a realistic yet manageable numerical analysis of the effects of highly anisotropic noise on passive bearing estimation. It is seen that the only variable parameters in the baseline study are the number of interferers, the angular separation between interferers, and the interferer locations relative to the array axis.

5.3 - Standard Deviation Results

The numerical effects of a highly anisotropic noise field are presented in figures 5.1 through 5.5 in terms of the standard deviation of the bearing error for the baseline case. Later, the bias error of the bearing estimates is presented. The standard deviation of bearing error or bearing estimate standard deviation is presented as a function of the target-to-interference separation which is expressed as the phase difference,

$$Y = \left(\omega_{KK} \frac{d}{c} \right) \cdot (\cos \theta_T - \cos \theta_I) \quad (5-8)$$

where $\omega_{KK} = \left(\frac{2\pi}{T} \right) \cdot (KK-1)$ is the highest radian frequency in the signal and noise bandwidths and,

θ_I is the mean interference bearing of the cluster of 1, 2, or 4 interferers.

TABLE 5.1
 BASELINE VALUES OF ARRAY, PROCESSOR,
 SIGNAL, AND NOISE PARAMETERS

PARAMETER	SYMBOL	VALUE
Number of hydrophones	LL	10
Hydrophone separation	D	20 feet
Integration time	T	0.128 seconds
Sample rate		250 Hz
Signal-to-Noise ratio	SNR	1.0
True target bearing	θ_T	90°
Interference-to-Noise ratio	INR	0.1
Number of interferers	MM	1, 2, 4
Interferer separation	($\Delta\theta$)	3, 6, 9 degrees
Interference location	θ_I	Theoretical: 0-180 degrees Simulation: 30, 45, 60, 70, 76, 82, 90 degrees
Signal and noise process bandwidth		101.5 Hz
Discrete bandwidth	KK-1	13
Number of beam positions per estimate	ISTEER (p)	13
Angular steering sector covered		86 - 94 degrees

Since the standard deviation of error metrics are symmetric about the zero phase separation, these results are presented as function of $|Y|$ rather than Y .

Figure 5.1 shows the standard deviation of error for the case of a single plane wave interference. Figures 5.2a, b, and c show the results for two interferers separated by 3, 6, and 9 degrees, respectively. Likewise, figures 5.3a, b, and c show the results for four interferers. Three general observations are readily apparent from these results. First, in every case the standard deviation of error exhibits a different behavior in each of three segments of the range of $|Y|$ values. For remote interferers, all three error measures are independent of the target-to-interference separation $|Y|$, and only somewhat larger than the standard deviation for isotropic noise alone. For intermediate values of $|Y|$ (approximately 0.4 to 1.0), the standard deviation metrics exhibit a peak value (or a relative maxima). Finally at small separations of target and interferer, the behavior of the three metrics appears to vary from case to case as a complex function of MM , $\Delta\theta$ and $|Y|$. The detailed behavior of the standard deviation of error in these three segments will be examined later.

A second general observation is that the Cramer-Rao bound indeed provides a lower bound on the bearing error except at very small phase separations (small $|Y|$), thus illustrating the performance degradation of the SBT processor over the ML processor. In some cases, at small $|Y|$ values, the theoretical SBT error becomes less than the Cramer-Rao bound. In these regions, the target and one or more interferers are unresolvable by both ML and SBT processors. However, the SBT processor essentially "sees" a single source of directional noise (with increased level) and a background noise field that is nearly incoherent, or isotropic. As a result of the

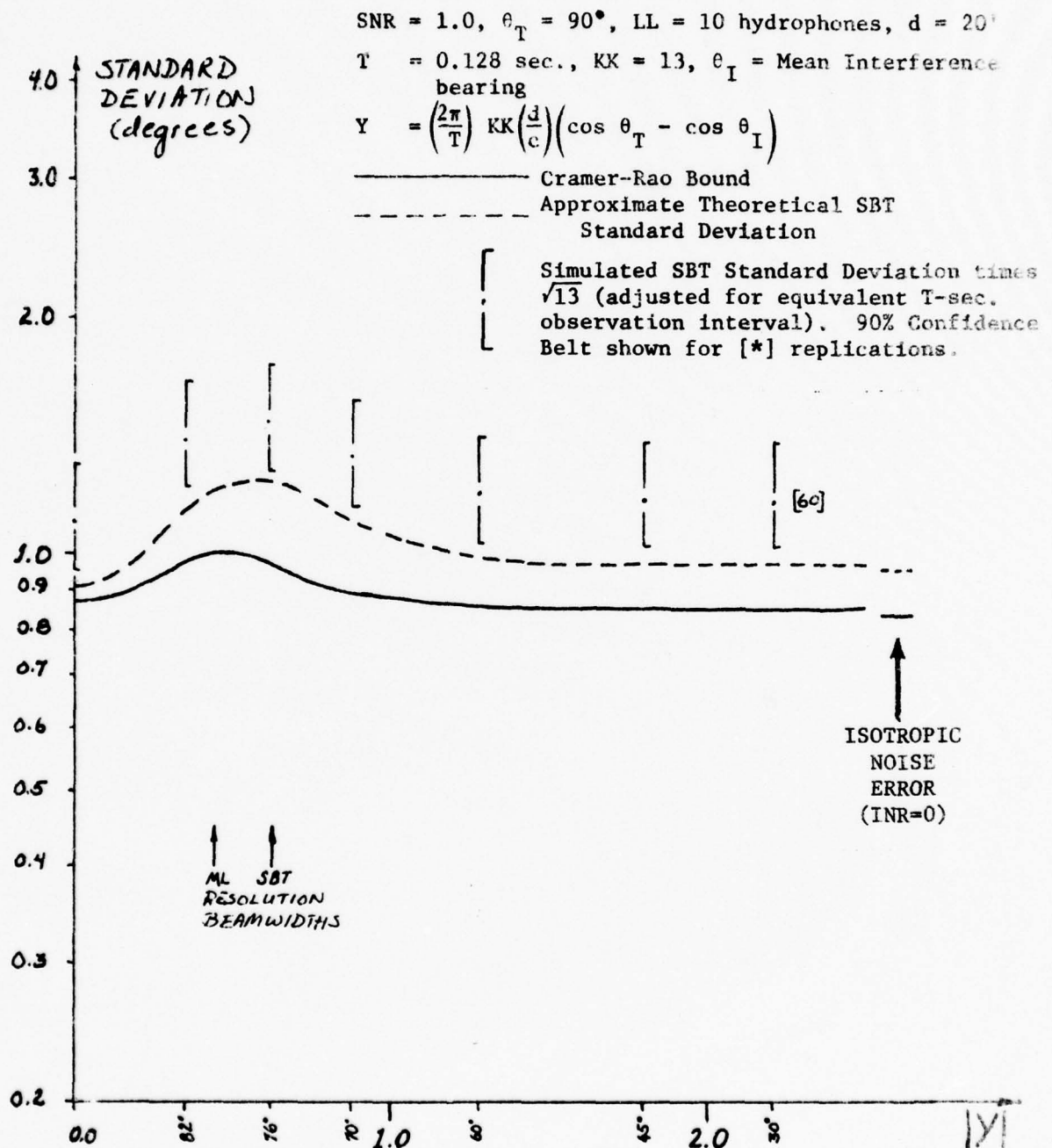


Figure 5.1 - Standard Deviation of Estimation Error, MM=1

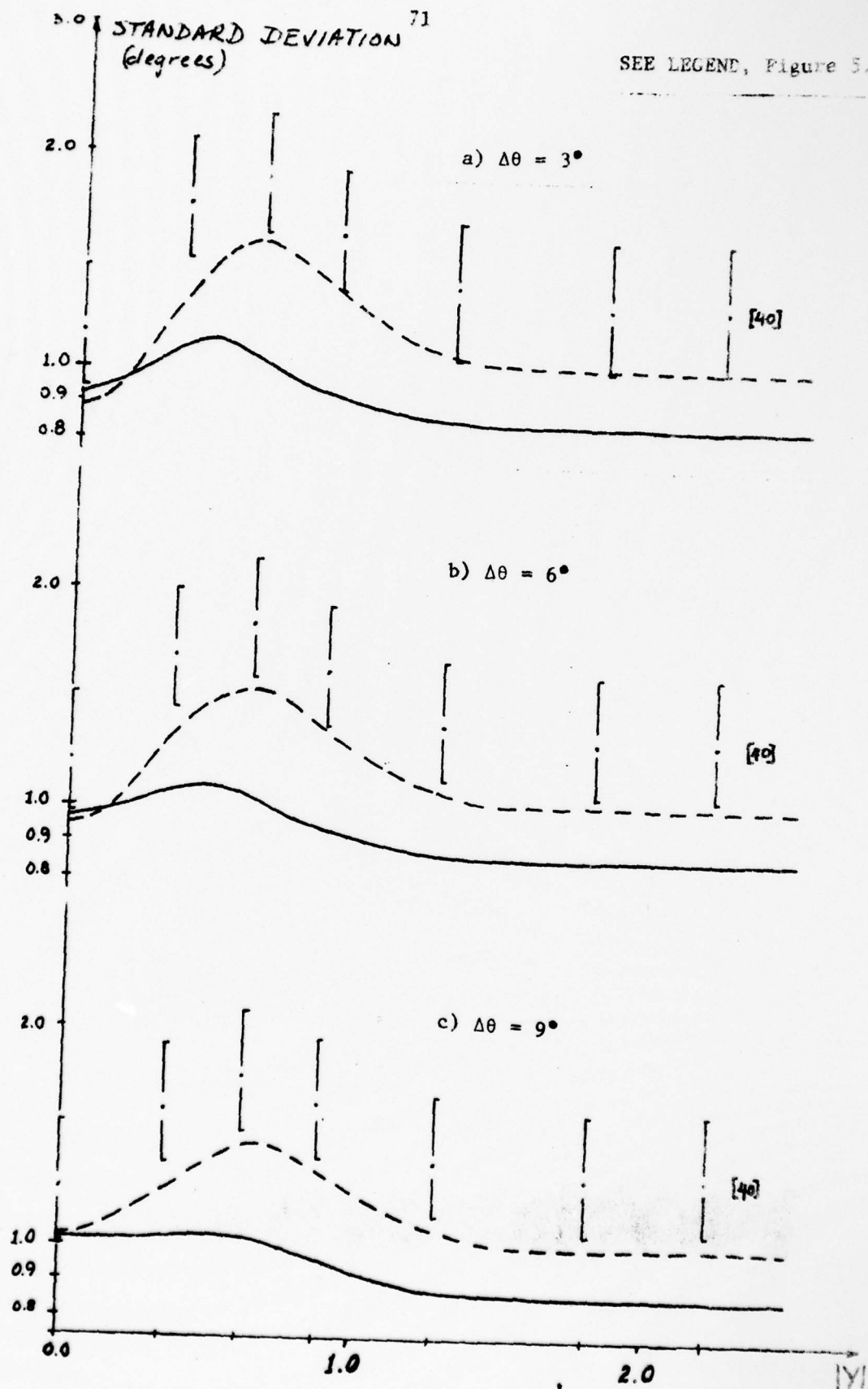


Figure 5.2 - Standard Deviation of Estimation Error, $MM=2$

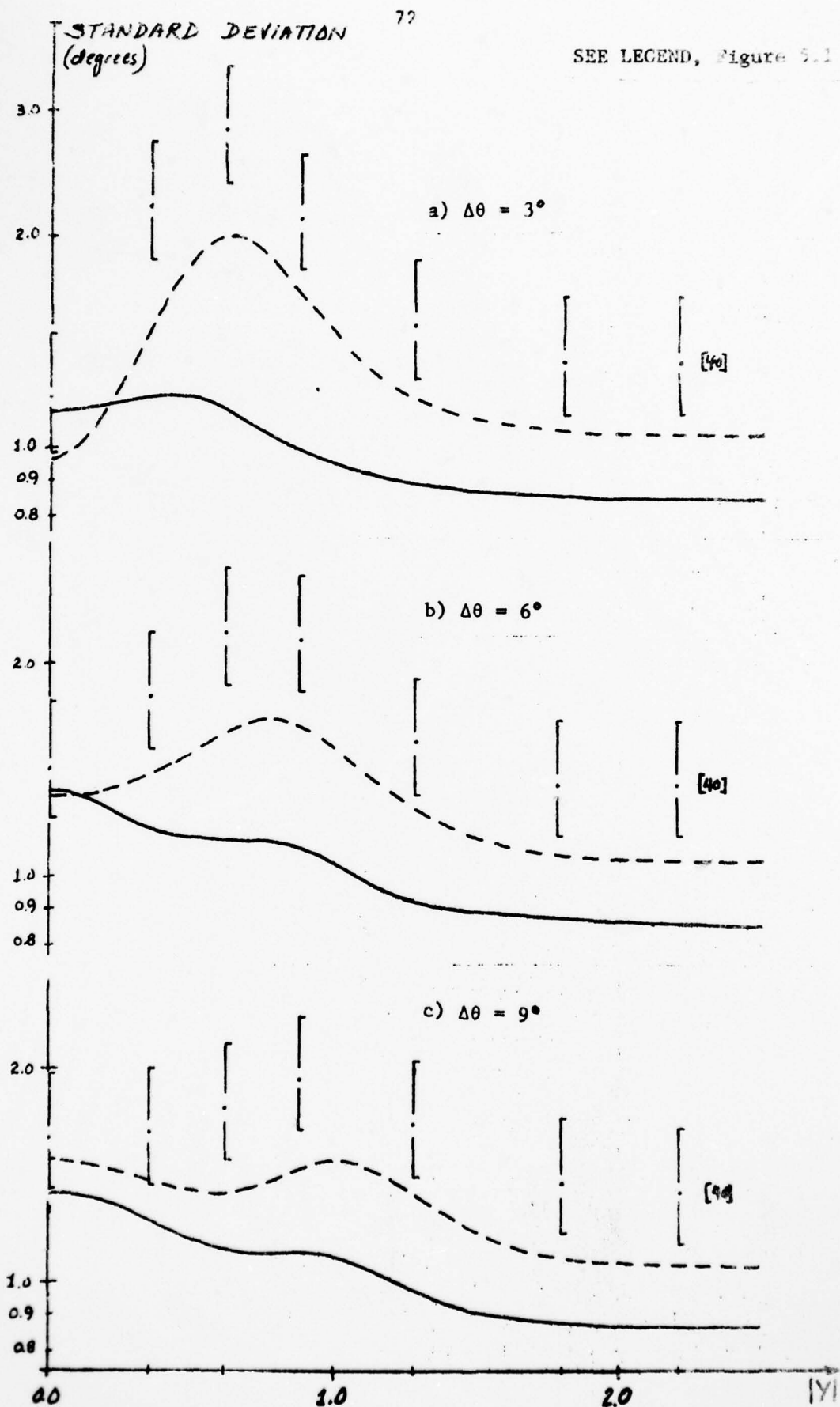


Figure 5.3 - Standard Deviation of Estimation Error, $MM=4$

higher apparent signal level, it is seen in figure 5.1 that the SBT error at small $|Y|$ falls below its own isotropic-noise error level. The performance of the ML estimator which is bounded by the larger, CR bound reflects the tacit assumption that the optimal estimator is perfectly matched to, or has perfect knowledge of, the true background noise field. Hence, the fact that the SBT and ML processors are addressing "different" noise fields at small $|Y|$ values is reflected by the seemingly superior performance of the SBT processor.

The third general observation is that the bearing error of the simulated SBT is, at the chosen confidence level of 0.90, significantly poorer than the approximate, theoretical SBT bearing error. This appears true in each of the figures 5.1 through 5.3 at most target-to-interference separations. The appearance that this difference is almost constant over all $|Y|$ values is explained by the use of the same set of input normal deviates for each of the seven target-to-interference separations examined by the simulation. The difference between the simulation and theoretical SBT bearing errors occurs consistently throughout the investigation. Although the exact cause of this somewhat unexpected difference is unknown, a combination of one or more of the following points is suggested as a possible explanation:

- 1) The number of replications (i.e., simulation runs) is small relative to the number of points used in the line fit. The SBT output values used in the LSE line fit occur in an eight degree segment of steering angles between 86° and 94° . The true bearing error, which is estimated by the simulation results, is on the order of one to two degrees - a significant fraction of the 8° segment of steering angles forming the line fit. Hence, the number of points used to form each

estimate and the number of estimates per sample will significantly affect the standard deviation of estimation error.

- 2) The theoretical assumption that the SBT output is a linear function of steering angle is invalid for the 86-94 degree range over which the simulation forms the LSE straight line fit. Figure 5.4 shows a plot of the theoretical SBT output mean, \bar{z}_0 , and standard deviation, σ_{z_0} , as functions of steering angle, α , using the expressions derived in chapter 3. Notice that in the 86-88 and 92-94 degree regions, the assumption of linearity is somewhat strained. The nature of this non-linearity would tend to cause a lower LSE line slope than expected and thus a higher standard deviation of error.
- 3) There are 13 points used by the LSE line fit estimator to obtain the baseline simulation bearing estimates. Under the assumption that 13 T-second observations of statistically identical random data produce an error variance which is 13 times lower than that obtained for a single T-second observation, the standard deviation of error has been multiplied by $\sqrt{13}$ for presentation in figures 5.1 to 5.3. Here lies the third possible contributing cause of the difference between simulated and theoretical bearing error. That is, the observations at 13 different beam positions ($86^\circ - 94^\circ$) may not be statistically identical, at least to the extent that it is optimistic to assume that the simulation error variance should be 13 times lower than an "equivalent" T-second error variance. A less optimistic assumption would, of course, result in lower "T-second equivalent" simulation bearing errors than those presented in figures 5.1-5.3.

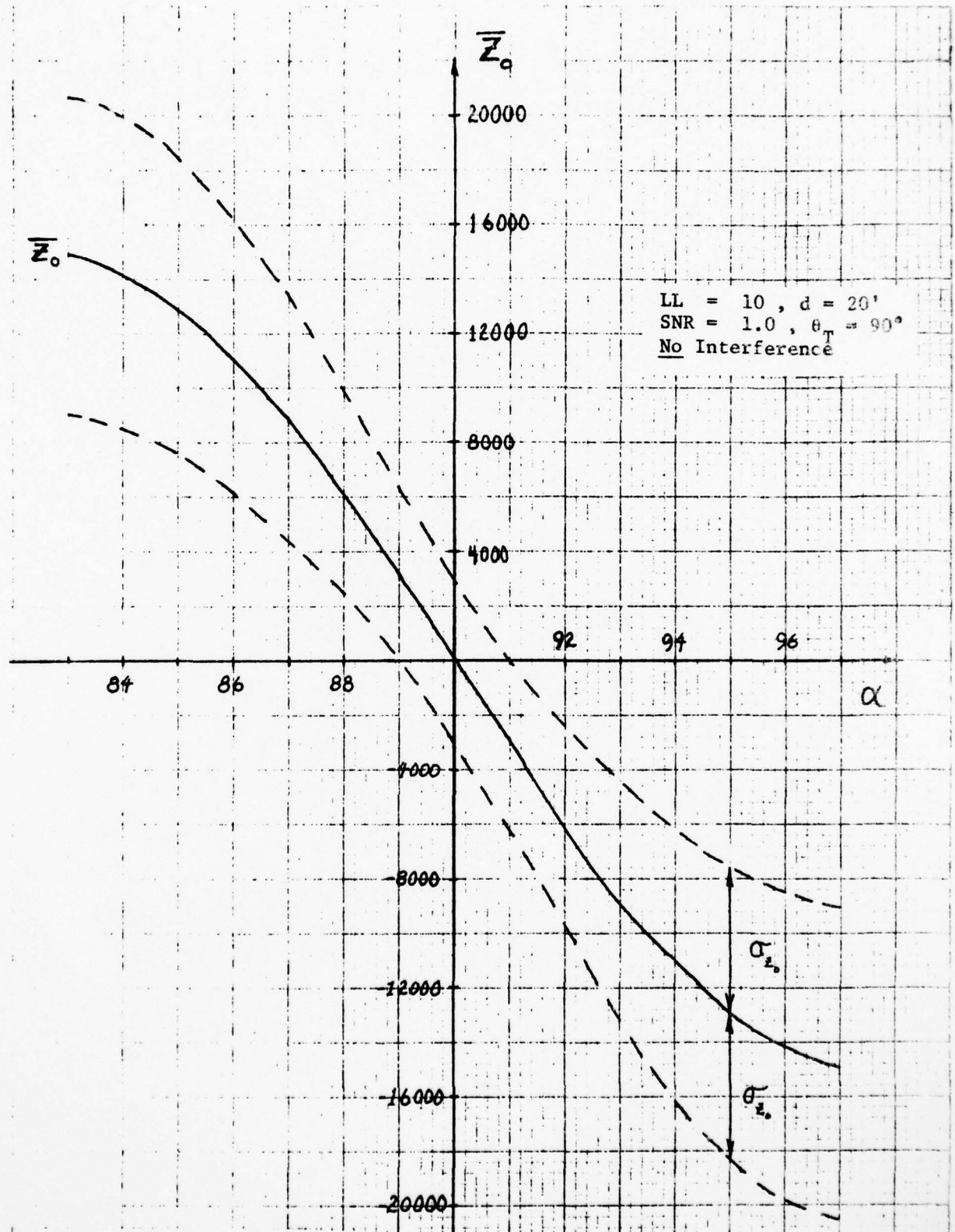


Figure 5.4 - Approximate, Theoretical SBT Output Mean and Standard Deviation

- 4) The actual observation time of 0.128 seconds is too small for the approximation, made in the theoretical SBT standard deviation of error derivation, that the spectral density, $X(\omega)$, can be expressed as

$$X(\omega) = \frac{1}{T} \cdot E \left\{ x(j\omega) x^*(j\omega) \right\} \quad (5-9)$$

where $x(j\omega)$ is the Fourier Transform of the signal-plus-noise-plus-interference process existing in the water at the face of the array.

Recalling the first general observation drawn from the standard deviation of error results, it seems appropriate to discuss the detailed effects of a highly anisotropic noise field in terms of the three levels of target-to-interference separations -- remote interferers, intermediate or "peak" interferers, and nearby or coincident interferers. In the intermediate $|Y|$ - region, the location of the peak error varies somewhat with M and θ . Also, the SBT error and the CR bounds peak at different locations. For the single interferer shown in figure 5.1, the locations of the error peaks are identified with the resolution beamwidths of the SBT and MI processors. In a previous theoretical investigation [7], Cox derived and evaluated an expression for the resolution power of the optimal (maximum likelihood) beamformer. From his results ([7], figure 4, p. 781) it is straightforward to determine that the resolution "beamwidths" (i.e. resolution power in terms of angular separation) for the parameters of interest are 14.2° for a conventional beamformer and 10° for the optimal beamformer. From figure 5.1, we see that the peak bearing error occurs when the target and interferer are separated by a resolution beamwidth. The results in figures 2 and 3 indicate that for multiple, closely spaced (e.g. 3°) interferers, the standard deviation of error peaks when the

mean interference location is approximately one resolution beamwidth from the target. As the interference separation, $\Delta\theta$, increases the $|Y|$ position of the peak error increases, reflecting the transition to independent interferer effects at $\Delta\theta$ values greater than a resolution beamwidth.

The effects of increasing the number and mutual separation of remotely positioned interfering noise sources is summarized in figure 5.5. It is obvious here that the mutual separation of interferers, like their position or bearing, has no effect on the standard deviation of error when the target-to-interference separation is large. The CR bound indicates that the ML estimator will also be independent of the number of remote interferers. The simulation and theoretical SBT errors indicate, however, that the sub-optimal processor performance worsens with increases in the number of remote interferers. Since the SBT is designed to discriminate against incoherent noise, it cannot cancel or "de-emphasize" the remote interference which in turn increases the equivalent background noise level. As discussed previously, the simulated SBT bearing error is significantly higher than the theoretical SBT error. However, its dependence on MM and $\Delta\theta$ closely mirrors that of the theoretical measure.

The behavior of the standard deviation of error in the mid or intermediate range of $|Y|$ values is shown in figure 5.6. This expresses the peak error as a function of $\Delta\theta$. As one might expect, the peak values of both the CR bound and the SBT error for multiple interferers approaches the single-interference values as the mutual separation increases. For interference separations on the order of two times the resolution beamwidth, multiple and single interferers would yield the same peak values. The CR bound now shows a slight dependence on number interferers while the

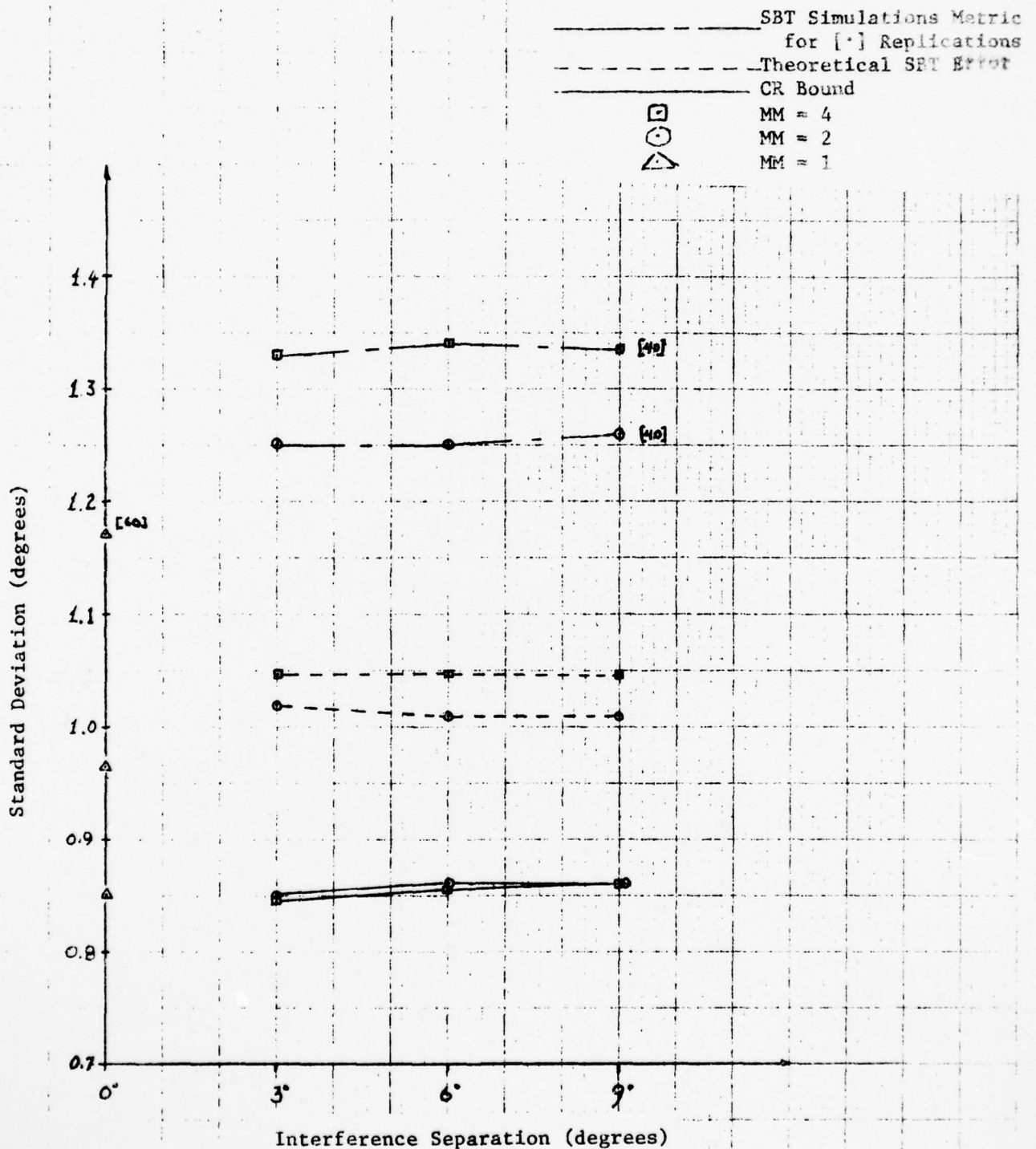


Figure 5.5 - Standard Deviation of Error for Remotely Positioned Interferers

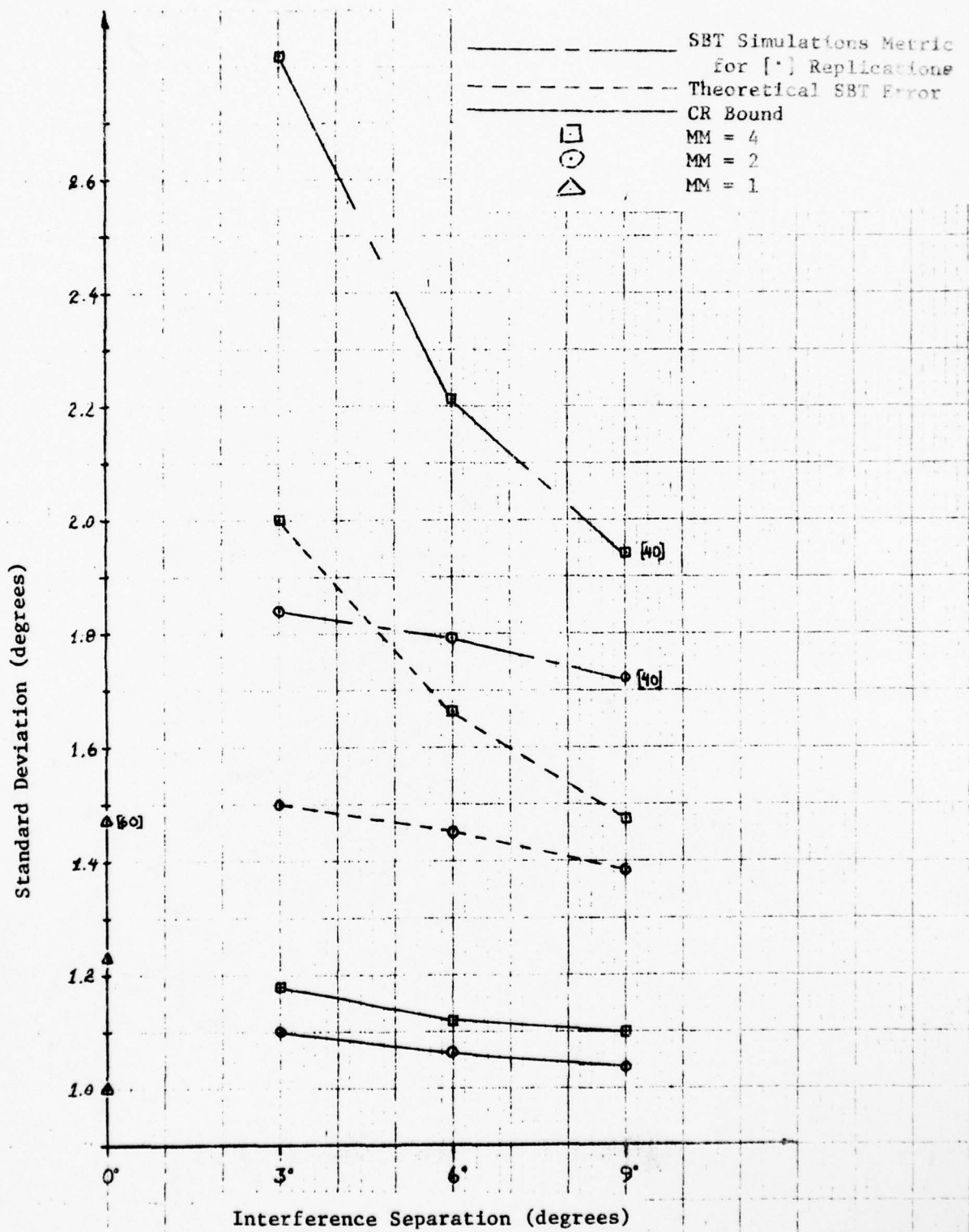


Figure 5.6 - Peak Standard Deviation of Error

SBT processor shows a high dependence on number of interferers when this separation is small.

The difference in the slopes of the error curves in figure 5.6 indicates a rapid deterioration in the relative performance (i.e. the ratio $\frac{\sigma_{\text{SBT}}}{\sigma_{\text{CR}}}$) of the SBT processor as the number of closely spaced interferers increases. MacDonald and Schultheiss [19] have shown that for incoherent background noise (no interferers) the relative, theoretical degradation of the SBT processor is

$$\frac{\sigma_{\text{SBT}}}{\sigma_{\text{CR}}} = \left(\frac{4}{3}\right)^{\frac{1}{2}} \cdot \frac{(LL - 1)^{\frac{1}{2}}}{LL} \quad (5-10)$$

where LL is the number of uniformly spaced hydrophones. For the 10-hydrophone array of interest, this ratio is 1.15. The results in figure 5.1 show theoretical and simulation degradations relative to the CR bound for a single interferer of 1.23 and 1.47, respectively. For four interferers separated by three degrees, the relative performance degradation has increased to 1.69 and 2.39 for the theoretical and simulation measures respectively. For smaller separations, we would expect larger relative performance losses. This data represents a very serious degradation in bearing estimation performance of the sub-optimal processor over the optimal processor but is not unexpected in light of the sub-optimal processor design emphasis on isotropic noise fields.

Figure 5.7 shows the standard deviation of bearing error behavior for coincident target and interference. As noted earlier, the CR bound appears not to provide a lower bound on the bearing estimation error for all separations of multiple interferers. Since the SBT processor has no knowledge of any directional aspects of the noise field, an interference in the proximity of the target is interpreted as an increase in signal

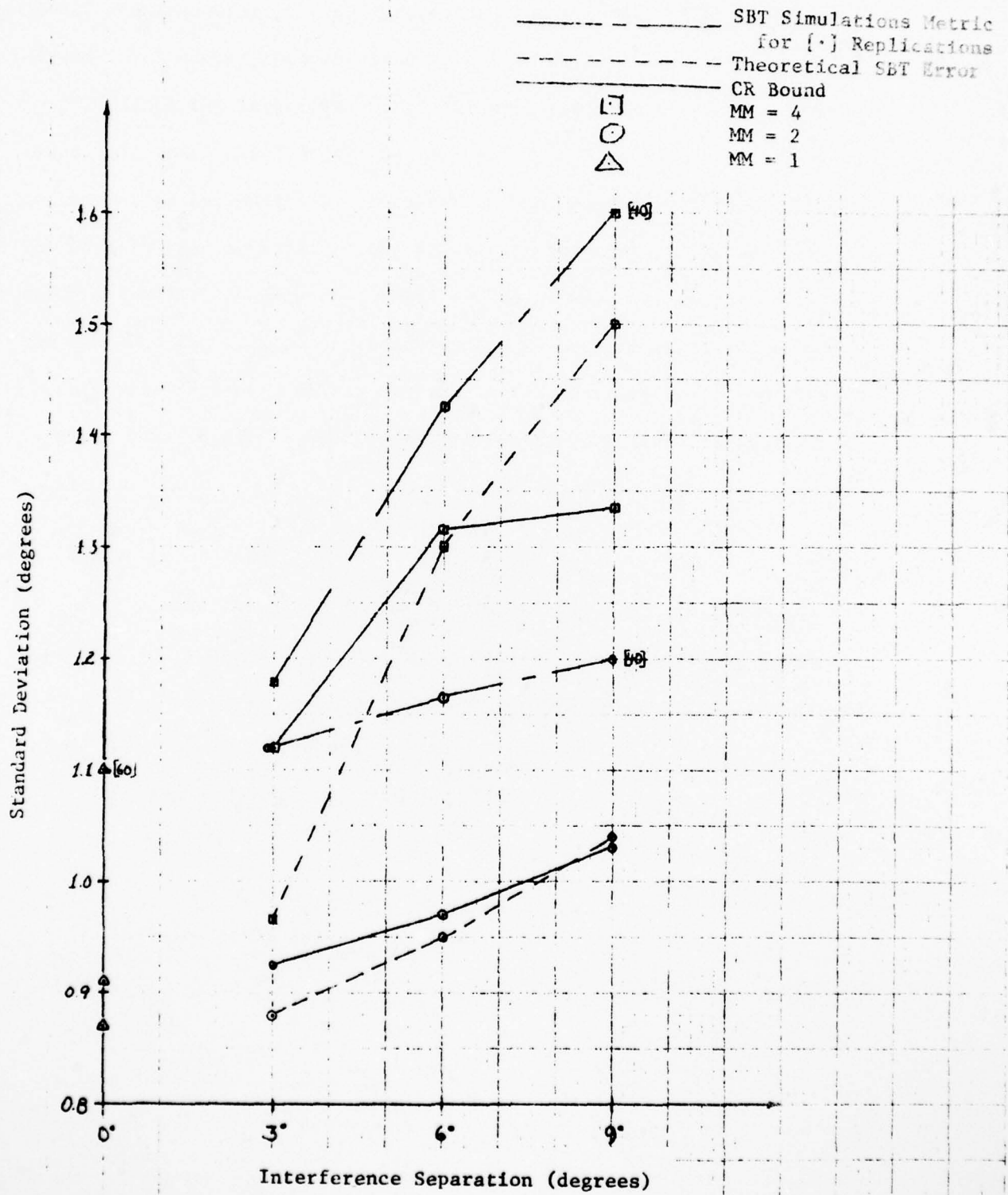


Figure 5.7 - Standard Deviation of Error - Coincident Interference

level. Consequently, the SBT processor sees a target with an effective signal level higher than the true target level.

Since the target is coincident with the mean bearing of the interference cluster, the standard deviation of error is seen to increase with increasing $\Delta\theta$ for multiple interferers. One would expect this behavior for $\Delta\theta$ less than or equal to the resolution beamwidths. As $\Delta\theta$ increases above a resolution beamwidth, there can be at most one interference within the beam and the effects of the remaining members of the interference cluster will decrease. Also, the simulation standard deviation of error is again seen to mirror the theoretical metric but at a somewhat higher level.

5.4 - Bias Error Results

The mean, or bias, errors determined for the baseline study are presented in figure 5.8 for a single interferer and figures 5.9 and 5.10 (a, b, and c) for two and four interferers at 3, 6, and 9 degree separations, respectively. The bias curves in figures 5.8 - 5.10 reflect only SBT errors since the optimal (ML) estimator is by assumption unbiased.

Several general observations can be made by examination of figures 5.8 - 5.10.

- 1) The bias error is anti-symmetric about θ_T and of significant magnitude over a wide range of target-to-interference separations (Y). As one might expect, the estimated bearings are biased in the direction of the interference location.
- 2) The bias errors exhibit peaks (relative extrema), whose locations and widths vary noticeably with number and separation of interferers.

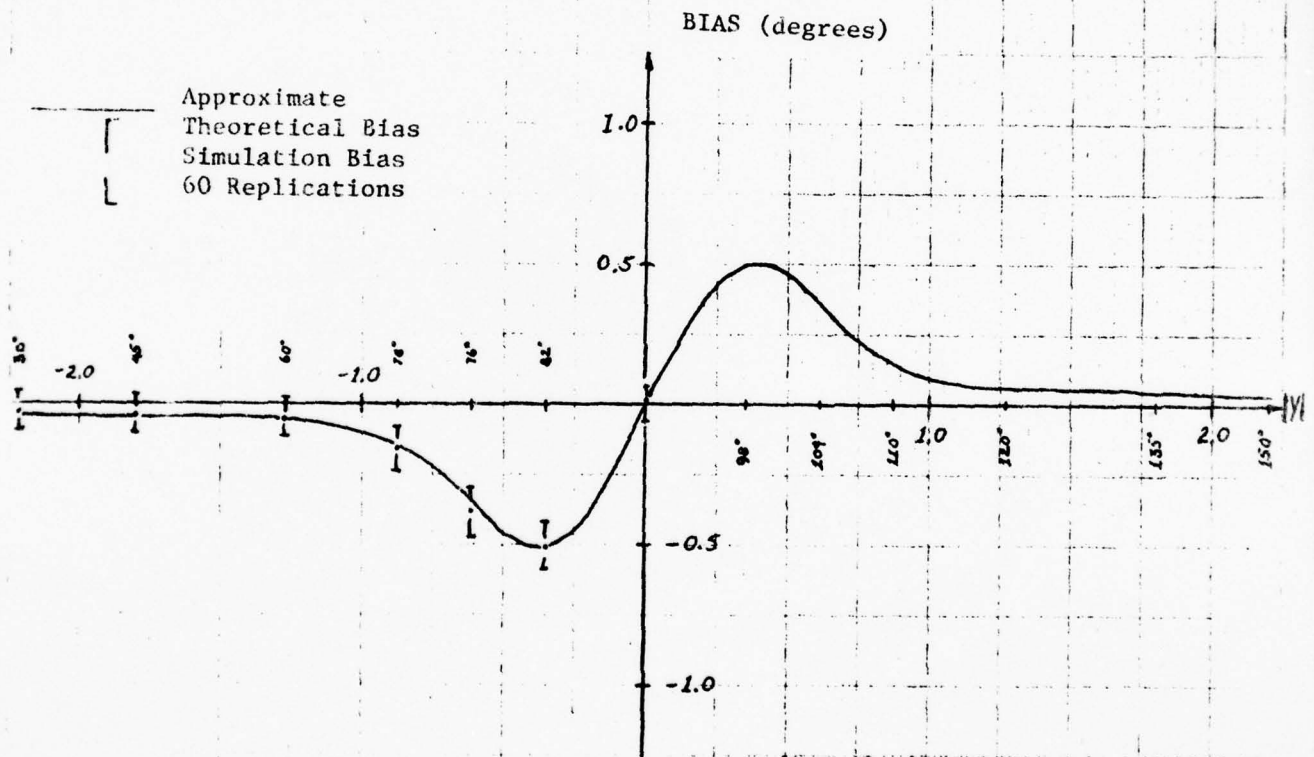


Figure 5.8 - SBT Bias Error Results, MM = 1

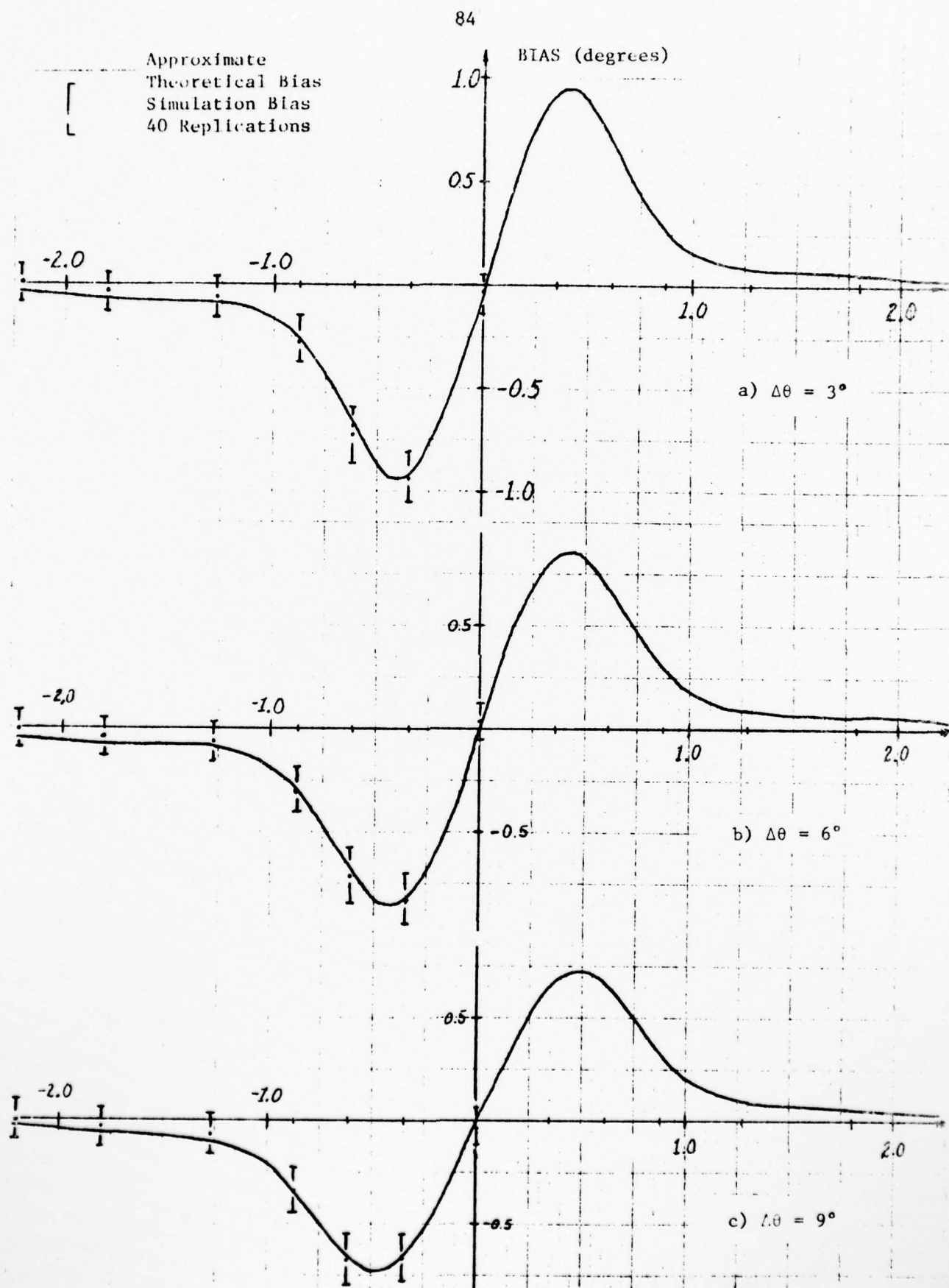


Figure 5.9 - SBT Bias Error Results, MM = 2

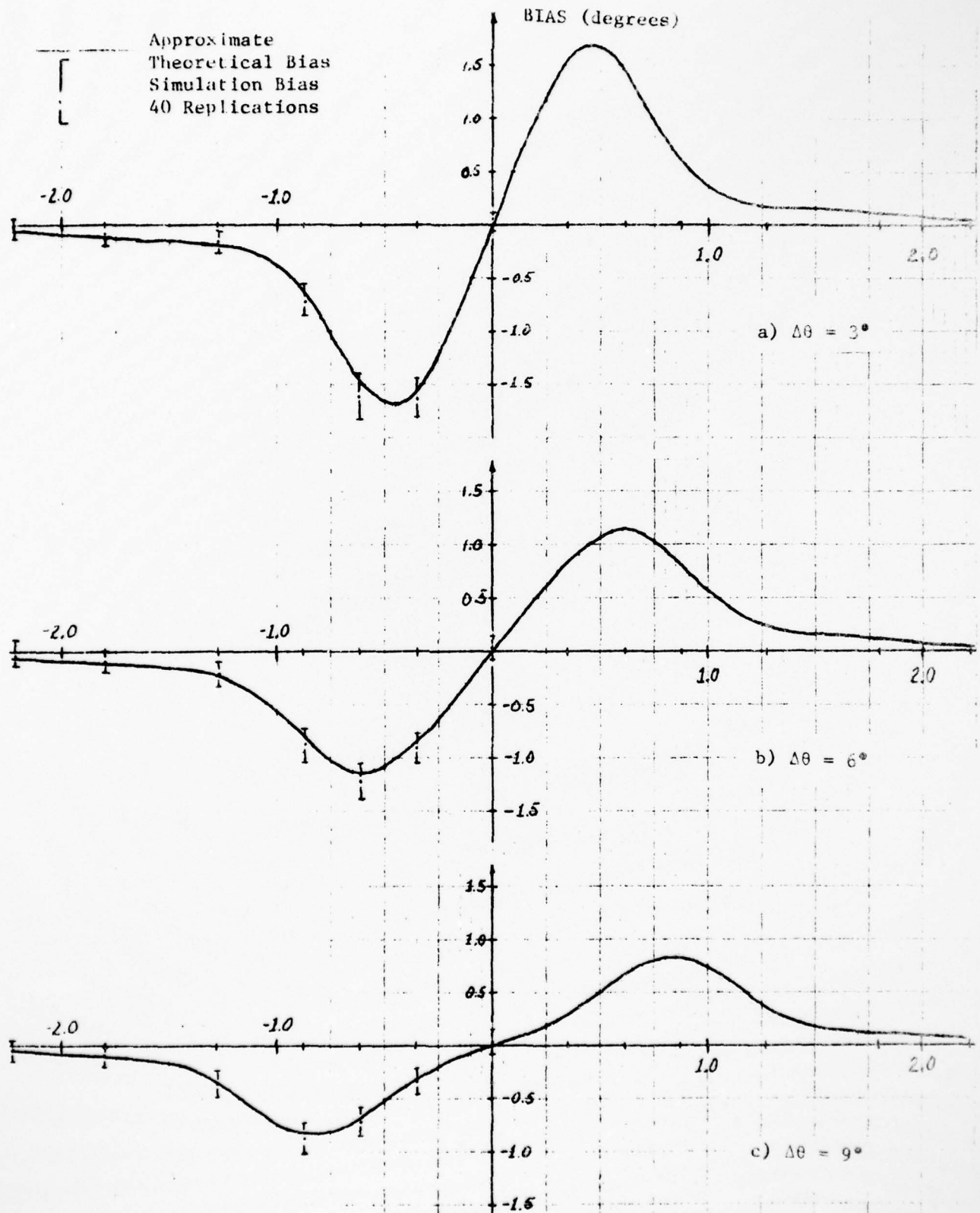


Figure 5.10 - SBT Bias Error Results, MM = 4

AD-A063 953

CATHOLIC UNIV OF AMERICA WASHINGTON D C ACOUSTICS GROUP F/G 17/1
PASSIVE SONAR BEARING ESTIMATION IN THE PRESENCE OF HIGHLY ANIS--ETC(U)
DEC 78 L R HOWELL N00014-77-C-0530

NL

UNCLASSIFIED

2 OF 2

AD
A063953



END
DATE
FILMED

4-79

DDC

For multiple interferers, the peak values decrease with increasing interference separation while the peak widths increase with increasing separation.

- 3) The simulation and theoretical bias errors are in close agreement for all cases. Unfortunately, this agreement offers no solid clue as to the source of discrepancy between the theoretical and simulated SBT standard deviations of error.

The detailed behavior of the absolute value of the peak SBT bias error as a function of number and separation of interferers is shown in figure 5.11. The close agreement between the theoretical and simulation bias metrics is apparent in figure 5.11. The bias measures decrease linearly as $\Delta\theta$ increases. The rapid performance degradation of the SBT processor as the number of closely spaced interferers increases is evidenced by the larger negative slope of the $MM = 4$ bias curve. A similar behavior was witnessed for the peak standard deviation of error curves presented in figure 5.6. As with the peak standard deviation of error, the peak bias error for multiple interferers will approach that for a single interferer as $\Delta\theta$ becomes large.

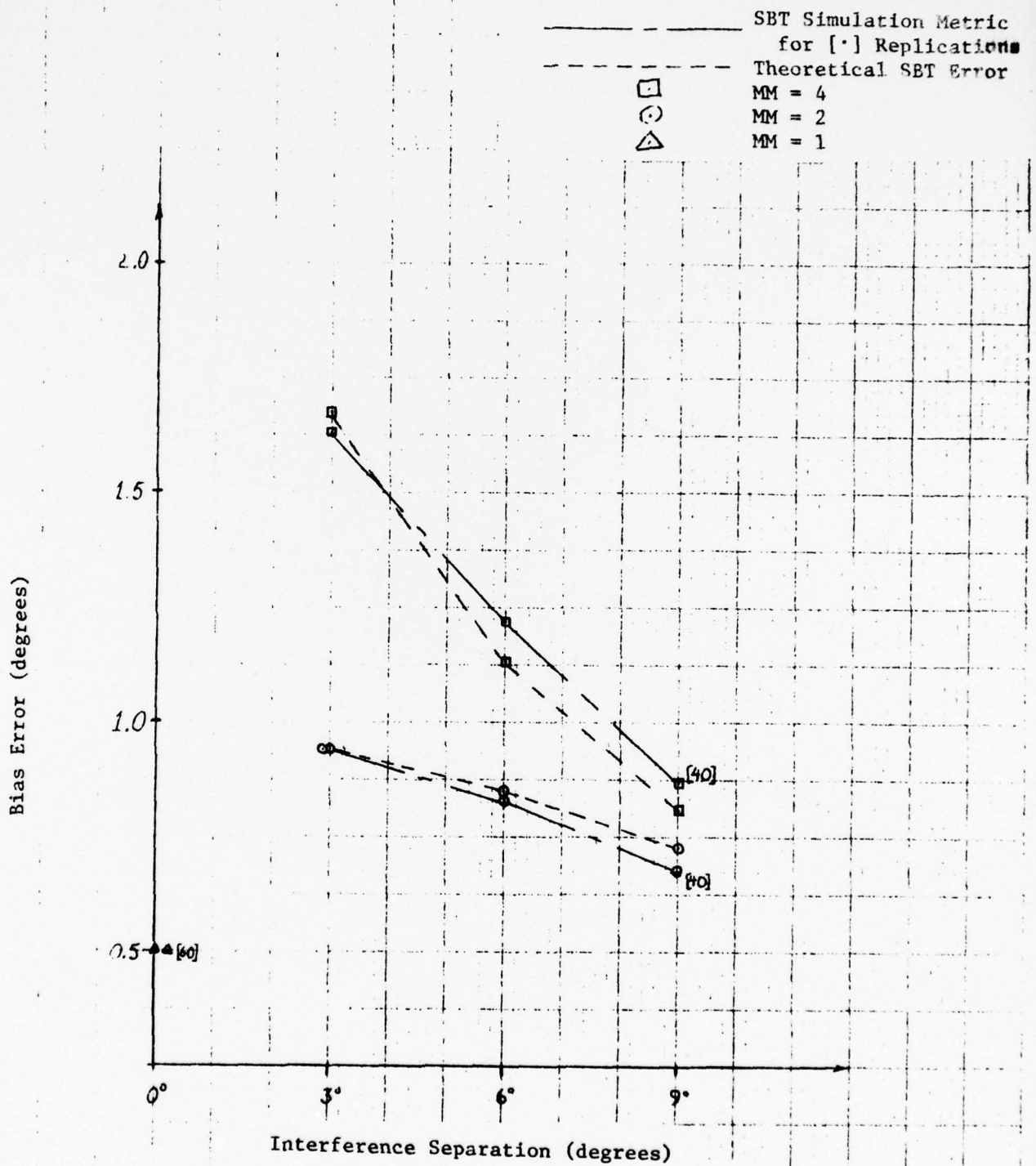


Figure 5.11 - Peak SBT Bias

CHAPTER VI

NUMERICAL RESULTS - PARAMETER EXTENSIONS

The results presented in chapter 5 provide basic insight into the effects of a highly anisotropic noise field on bearing estimation by optimal (ML) and sub-optimal (SBT) processors. In this chapter, added insight into the effects of such a noise field is provided by the numerical results of extending the range of values of selected, fixed baseline parameters. To maintain manageability and economic feasibility, only two of the potentially more interesting parameters are examined in this phase of the study. The dependency of bearing estimation performance on received signal-to-noise (SNR) ratio is presented in section 6.1 with the numerical results for SNR values of 0.5 and 2.0. The following section presents the results of extending the array size to 20 and 40 hydrophones (for an SNR of 1.0). Except as noted in each section, the remaining fixed and variable parameters assume their baseline values as defined in table 5.1.

6.1 - Extension of Signal-to-Noise Ratio

This section presents the results of extending signal-to-noise range to 0.5 and 2.0. This SNR range covers many of the situations encountered in actual target tracking applications. Although the simulated bearing error has been consistently higher than the approximate theoretical error, its overall behavior as a function of number and location of interferers is again expected to mirror the theoretical metric. Consequently, the simulation was not exercised for interference bearings of 30° and 60°. The simulation results for the remaining five interferer positions (45°,

70°, 76°, 82°, 90°) are presented in this section. Furthermore, at each interferer position the simulation sample size is limited to 20 replications. Note that throughout the SNR parameter extension, the array size remains at 10 hydrophones.

The numerical results of evaluating the three standard deviation of error metrics and the two bias error metrics are presented in figures 1-7 and 8-14, respectively of appendix D. For clarity, the baseline results at $\text{SNR} = 1.0$ are not repeated in these figures.

Several observations can be made upon examination of the standard deviation of error metrics in figures D.1 - D.7 regarding the extended SNR parameter values:

- 1) Over the entire range of $|Y|$, the standard deviation of error increases at small signal-to-noise ratios. For the most part, this phenomena results from the loss in signal power relative to the isotropic component of the background noise level. Another contribution to this effect is possible since, even at remote interference bearings, the total interference power will contribute somewhat to the received background noise level seen by the two processors.
- 2) The larger peak magnitude of the standard deviation of error and the seemingly superior coincident ($|Y| = 0$) performance, by the SBT processor relative to the CR bound at low SNR, results from a loss in signal level relative to the received interference power. In other words, these are phenomena observed as a result of a decreased signal-to-interference power ratio. Observe also that, although the error peaks are sharper (larger relative to the bound) at $\text{SNR} = 0.5$, their bearing location ($|Y|$ value) remains constant over the SNR range of values.

3) The apparent discrepancy between the theoretical and the simulated SBT standard deviations of error that was discussed in chapter 5 is also manifest in the results presented in appendix D. It is noteworthy, however, that the discrepancy worsens significantly around the error peaks for multiple interferers, particularly when closely spaced. For example, consider figure D.5 for four interferers separated by 3° . The simulation errors at $|Y|$ equal 0.355 and 0.618 for $\text{SNR} = 0.5$ have been adjusted to reflect smaller sample sizes of 18 and 16 replications, respectively. These sizes result from an after-the-fact rejection of three obviously unacceptable bearing estimates. The small "x" at Y equal 0.355 and 0.618 indicate that respective error magnitudes of 4.8 and 12.24 degrees were obtained for the original simulation sample sizes. The rationale here is that such poor bearing estimates ($\hat{\theta} = 81.9^\circ$, 78.6° , and 75.2°) would be ignored in any automatically or manually operated bearing estimation system. Furthermore, it is noted that the full, original sample sizes of 19 and 18 replications at $|Y|$ equal to 0.355 and 0.618, respectively, and $\text{SNR} = 0.5$ in figure D.5 are smaller than the other 20-run samples due to an absence of a zero-crossing by the simulation output, and hence no bearing estimate, for three simulation runs.

The unacceptable estimates from some runs and the absence of a zero-crossing in other runs is a consequence of the simulated SBT output becoming non-linear in the 86° - 94° region of the LSE line fit. This non-linearity is also responsible for the larger discrepancy between the theoretical and simulated standard deviations of error at these $|Y|$ - values. The nature of this non-linearity is shown in figure 6.1. This figure shows the theoretical mean and standard deviation of the SBT

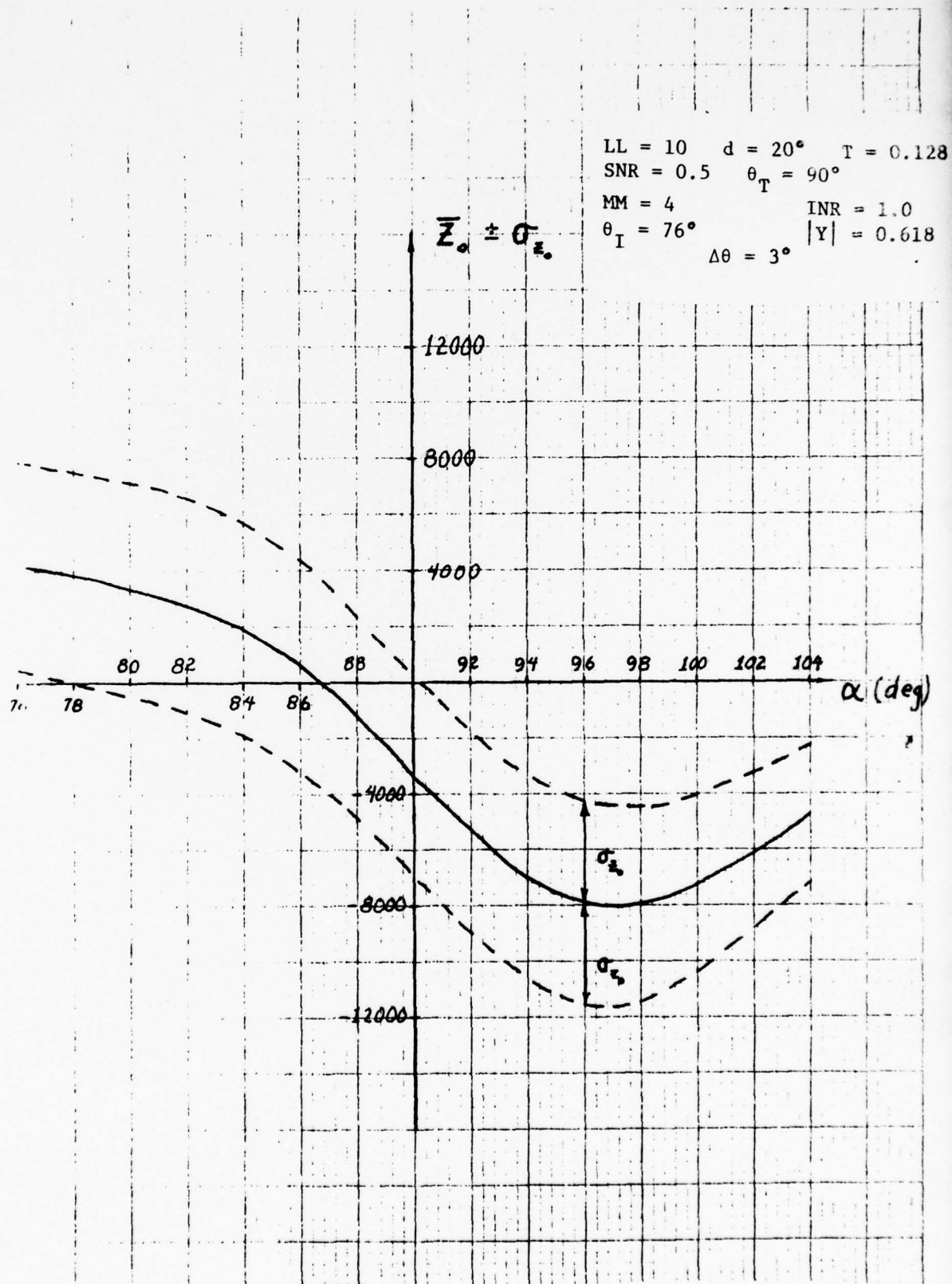


Figure 6.1 - Approximate, Theoretical SBT Mean and Standard Deviation;
 SNR = 0.5 with Four Interferers at 76°

output (equations (3-22) and (3-23)) for an SNR of 0.5 and four interferers separated by 3° and centered at a bearing of 76° ($|Y| = 0.618$). The occurrence of the non-linearity in figure 6.1 for small \bar{z}_0 values indicates not only a large bearing estimation variance but also an asymmetric probability density function (pdf) for $\hat{\theta}_1$. The unacceptably low bearing estimates mentioned previously (81.9° , 78.6° , and 75.2°) are a consequence of the unusually long "tail" in the $\hat{\theta}_1$ pdf. As seen in figure 6.1, the lower one-sigma value of the $\hat{\theta}_1$ pdf occurs approximately 8.7° below the 86.7° theoretical mean while the upper one-sigma value occurs only 3.5° above the mean. Hence, while the three exceptionally low bearing estimates might be unacceptable in an operational application, they are statistically valid estimates which are indicative of a lower SNR limit on bearing estimation by the SBT processor.

Several general observations can also be made from the SBT bias error results presented in figures D.8 through D.14:

- 1) SNR variation affects the SBT bias error primarily by compressing or amplifying the bias error peaks. At low SNR levels (approximately equal to the interference level) the bias peak has risen to the extent indicative of bearing estimates midway between target and interference. This is approximately true for $\text{SNR} = 0.5$ in figure D.12. For an SNR less than the INR at close separations, the SBT processor would be, in essence, estimating the interference bearing rather than the signal bearing.
- 2) For low bias values such as at $\text{SNR} = 2.0$ and $\text{MM} = 1$, a difference in the theoretical and simulation bias metrics appears. However, at a 90% confidence level we cannot say that this difference is significant. Also

note that for $MM = 4$ and $SNR = 2.0$ (figure D.12) the theoretical and simulation bias metrics tend to converge as their magnitudes increase. These two events might suggest the difference in bias metrics at high SNR is statistical (i.e. due to a small sample size and/or too few points in LSE line fit).

- 3) Recalling the non-linearity of the mean, \bar{z}_0 and standard deviation, σ_{z_0} , of the SBT output shown in figure 6.1, one would expect it to eventually affect the bearing estimation bias error as it did the standard deviation of bearing error. Indeed, one observes in figure D.12 that the absolute values of simulation bias error are greater than the theoretical values for the uncorrected sample sizes (19 and 18 replications) at $Y = \pm 0.355$ and ± 0.618 . Removal of the three unacceptable estimates as discussed previously yields simulation bias errors somewhat closer to the theoretical metric. From figures D.5 through D.12, it is seen that for four closely spaced interferers located within about 20° of a 0.5 SNR target the SBT processor is practically useless as a bearing estimator.

The behavior of the standard deviation metrics as functions of signal-to-noise ratio can also be examined parametrically in each of the three previously defined regions of target-to-interference separation, $|Y|$. Figure 6.2 shows the effects of increasing the signal-to-noise ratio for remote interference bearings (large $|Y|$). The primary observation from figure 6.2 is that, except for the simulation error at $SNR = 2.0$, the standard deviation of error metrics vary exponentially with SNR. For full logarithmic scaled coordinates, it is easy to show that the unscaled slope of a straight line is the exponential power of the abscissa which

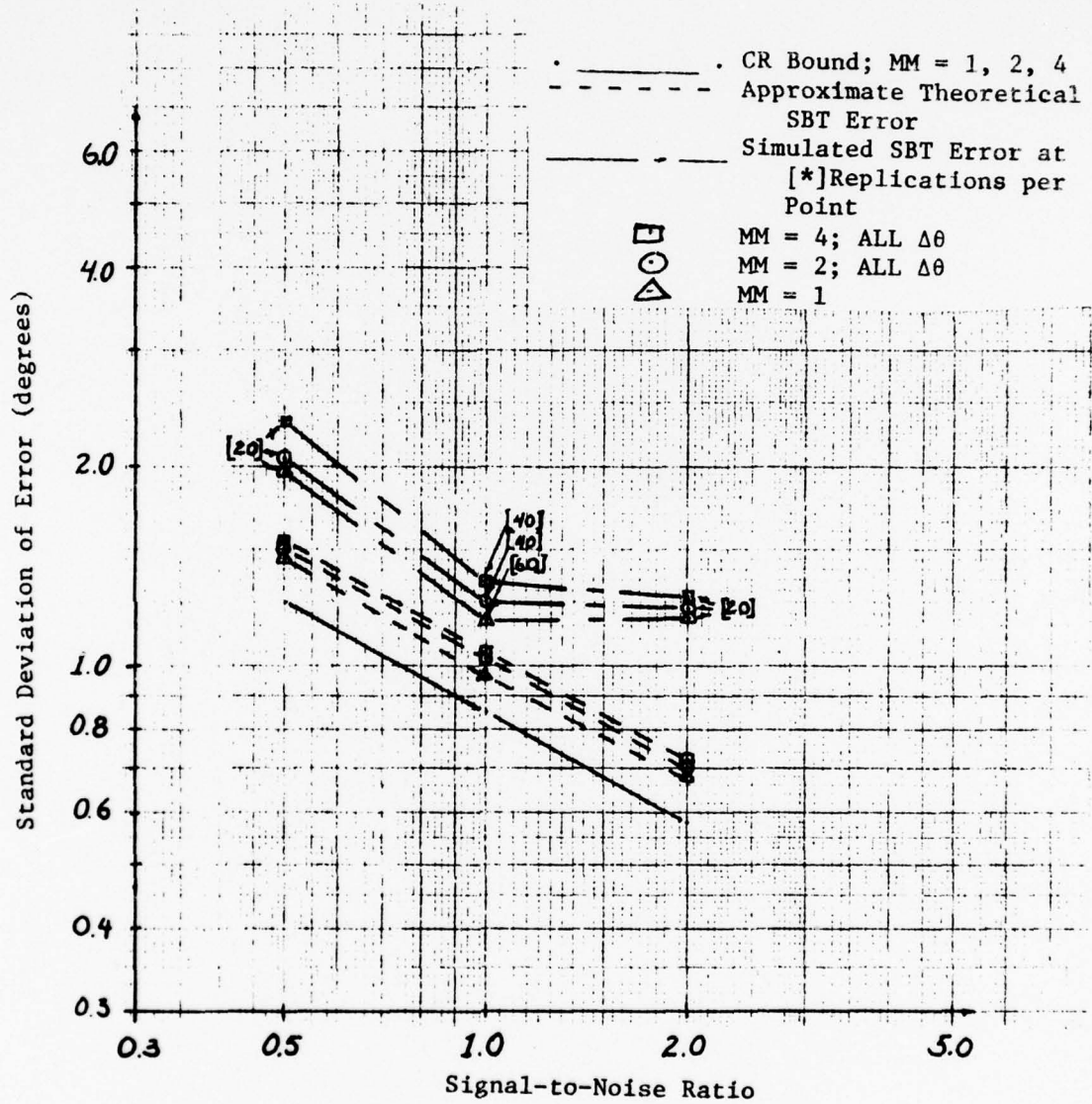


Figure 6.2 - Standard Deviation of Error vs. SNR;
Remote Interference

governs the variation of the ordinate function. Consequently, we see from Figure 6.2 the standard deviation of error varies inversely with the square root of the fractional signal-to-noise ratio, SNR. This contrasts with MacDonald's [18] results that the standard deviation of error (remote interference bearings) is inversely proportional to SNR for conditions of high INR and low SNR.

The CR bound is seen to be identical for all values of MM and $\Delta\theta$ at remote interference bearings. The SBT metrics, while also independent of $\Delta\theta$, show a slight dependence on the number of interferers present, MM .

The simulation error metric in figure 6.2 appears approximately constant over the 1.0 to 2.0 range of SNR values, thus indicating a larger theoretical/simulation error discrepancy than previously identified. This unexpected behavior is probably indicative of a bearing resolution limit characteristic of our digital estimation algorithm. In other words, the simulation random errors at $SNR = 2.0$ based on 13 T-second observations (13 beam positions) are not resolvable beyond one-half the angular separation between adjacent beam positions (0.33 degrees). Consequently, the estimation algorithm would yield erroneous results when the true random error falls below half the beam position spacing. The relatively small sample size at $SNR = 2.0$ (20 replications) would also contribute to this behavior. If these theoretical/simulation discrepancies are indeed caused by the LSE line fit, then hopefully they can be eliminated by proper selection of the parameters of the bearing estimator. It is clear that there is room for more investigation into the digital implementation of bearing estimators which are based on zero crossings of an array processor output.

Figure 6.3 indicates that the peak standard deviation of error is also inversely proportional to the square root of the signal-to-noise ratio. Only the 3° separation of multiple interferers is shown in figure 6.3. The peak errors for 6 and 9 degree separations are smaller than the $\Delta\theta = 3^\circ$ results but exhibit similar behavior as SNR increases. The SBT metrics in figure 6.3 indicate a greater sub-optimal processor degradation as the number of closely spaced interferers increases than indicated by the CR bound for the ML estimator. The simulated SBT error appears to behave more like the theoretical SBT error at the higher, peak error values than it did for remote interference bearings.

For the case of a coincident target and interference, the behavior of the standard deviation of error metrics shown in figure 6.4 closely resembles that of the error metrics for remotely positioned interferers (figure 6.2). Notable differences seen in figure 6.4 are:

- 1) Generally lower (by 0.3° to 0.5°) SBT standard deviation of error metrics.
- 2) The CR bound depends on the number of interferers.
- 3) The SBT error is not consistently bounded below by the CR bound.

As a final measure of the SNR dependence of bearing estimation performance metrics, consider the peak SBT bias errors presented in figure 6.5. The previously noted theoretical/simulation bias discrepancy is again evident at $\text{SNR} = 2.0$. This bias discrepancy decreases as the magnitudes of each metric increase. This discrepancy was previously associated with a bearing resolution limit of the SBT simulation and the small sample size at $\text{SNR} = 2.0$. Of primary importance, however, are the following two observations:

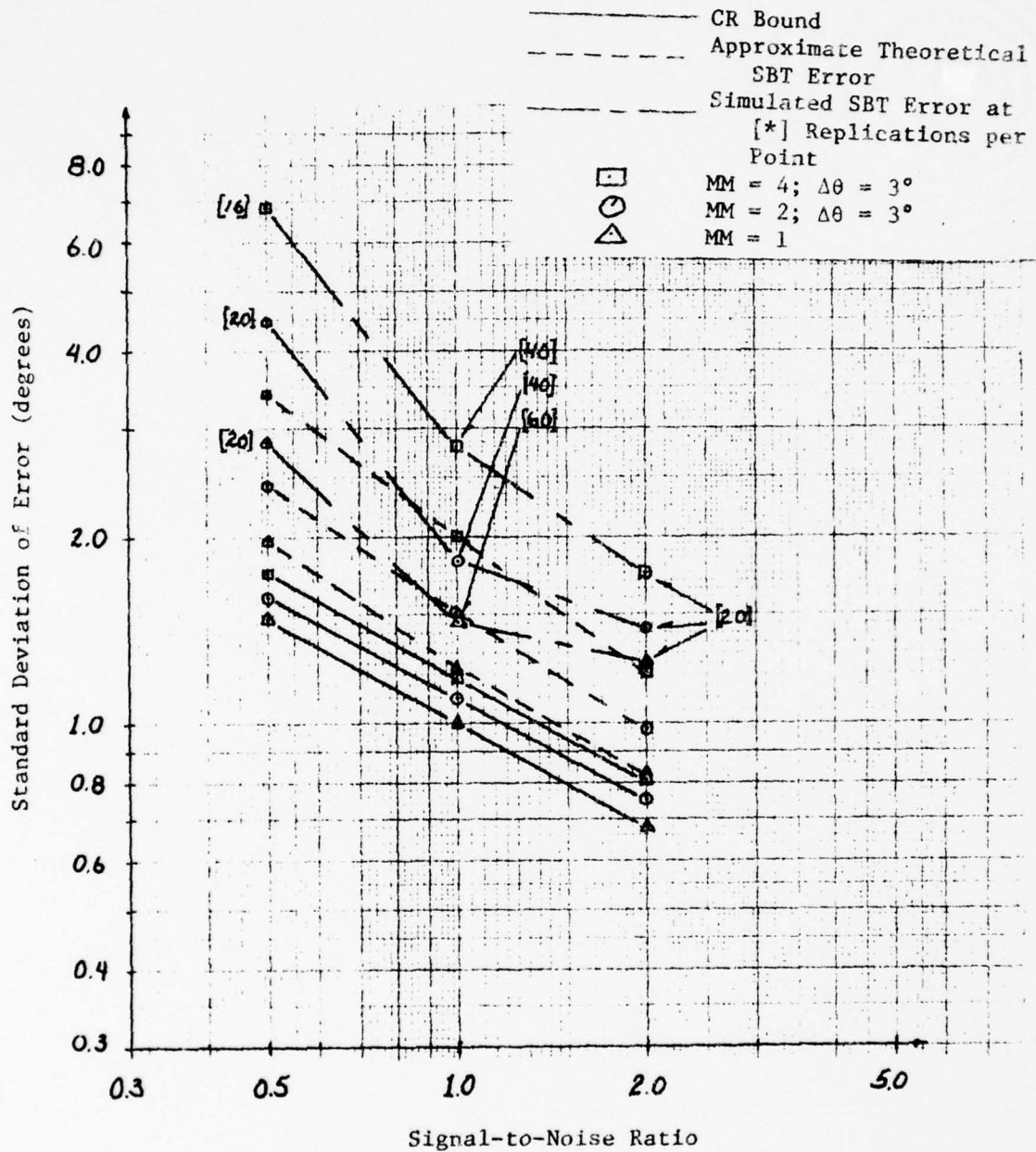


Figure 6.3 - Peak Standard Deviation of Error vs. SNR
(Intermediate Separations)

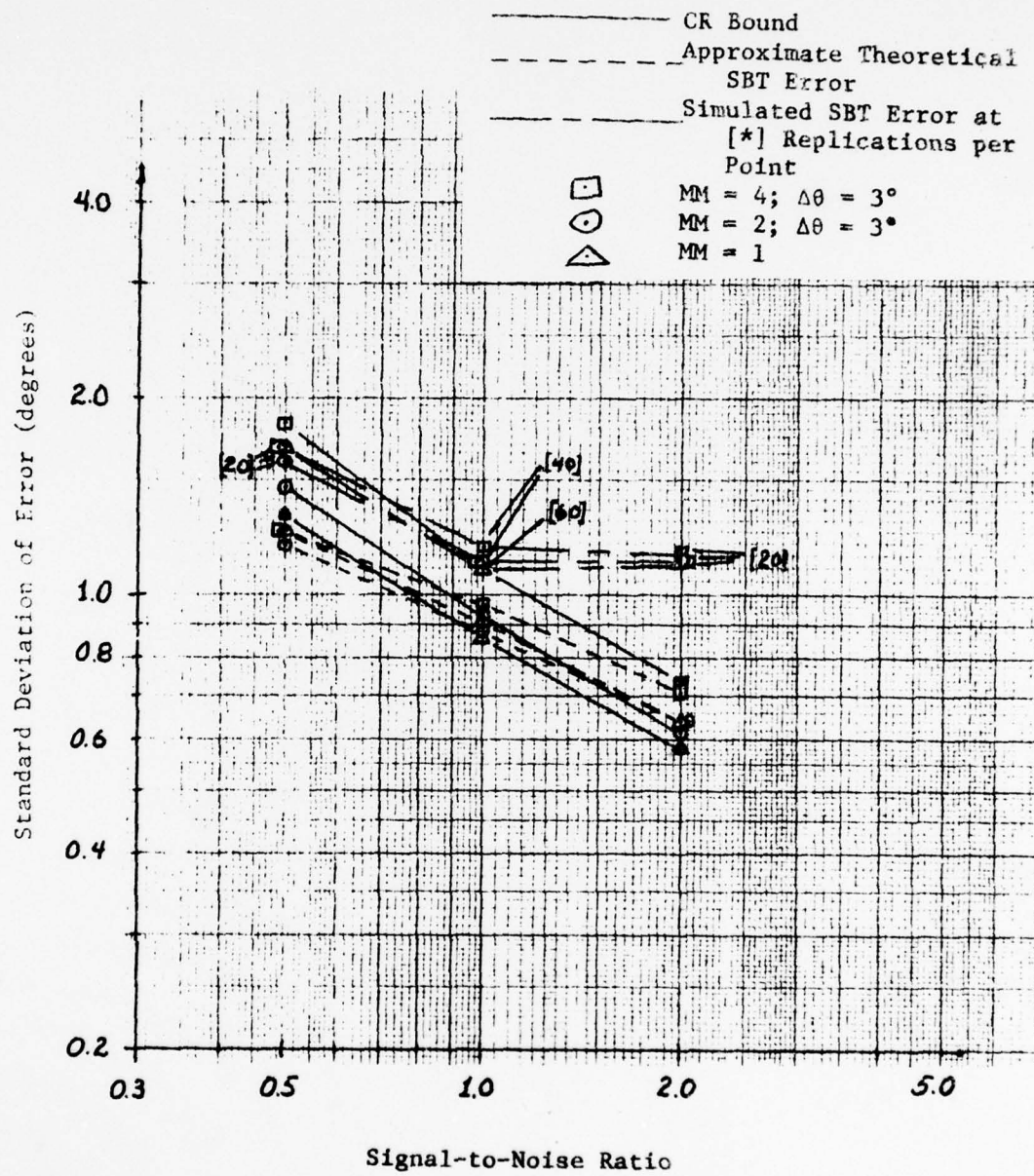


Figure 6.4 - Standard Deviation of Error vs. SNR;
Coincident Interference

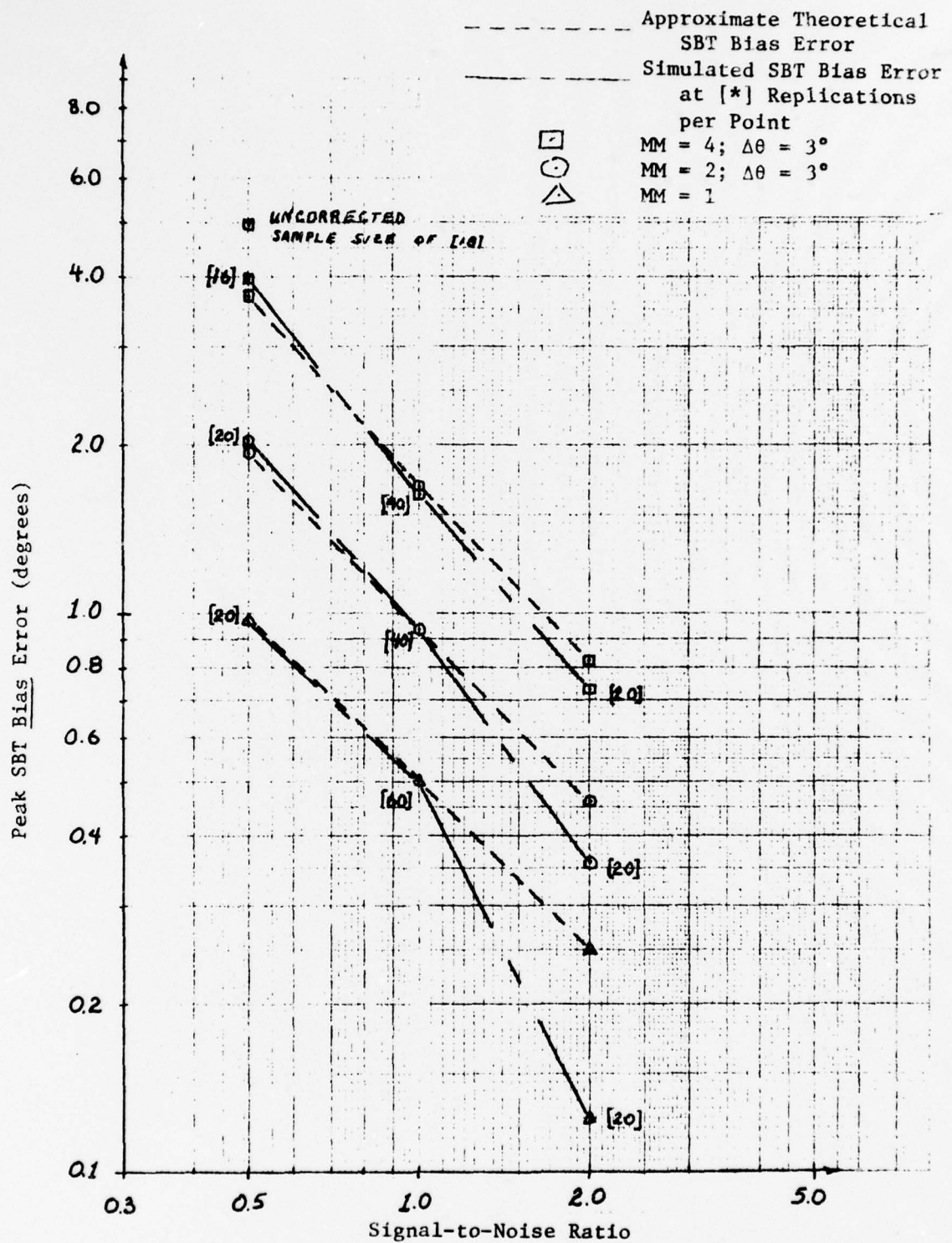


Figure 6.5 - Peak SBT Bias Error vs. SNR;

1) For 1, 2, and 4 closely spaced interferers, the SBT bias error is inversely proportional to the fractional signal-to-noise ratio, SNR.

2) The SBT bias errors are directly proportional to the number, MM, of closely spaced interferers.

These two observations indicate that the peak SBT bias error is, to a good approximation, inversely proportional to the signal-to-total-coherent-

$$\text{noise level, } \frac{S}{(MM \cdot I)} = \frac{\frac{S}{N}}{MM \cdot \frac{I}{N}} .$$

6.4 - Extended Array Size

This section presents the results of extending the array size, LL, to 20 and 40 hydrophones. These results address only the case of a signal-to-noise ratio of 1.0. Several adjustments to the baseline set of parameter values were necessitated by the extension of the array size. These adjustments are required by the smaller resolution beamwidths obtained with the larger apertures. For example, since adjacent, resolvable interferers will affect the array processors almost independently, it is of little interest to study multiple, widely separated (much more than a beamwidth) interferers and since the larger 20- and 40-hydrophone arrays have beamwidths smaller than 9°, the interference separation parameter assumes only the 3 and 6 degree values for this portion of the analysis.

A related aspect of the larger array size is the smaller segment of steering angles over which the SBT output is approximately linear. Figures 6.6 and 6.7 show the approximate theoretical output mean and standard deviation for array sizes of 20 and 40 hydrophones, respectively. Increasing the array size appears to amplify the SBT output extrema and shift them closer to the zero-crossing and hence decrease the angular region of

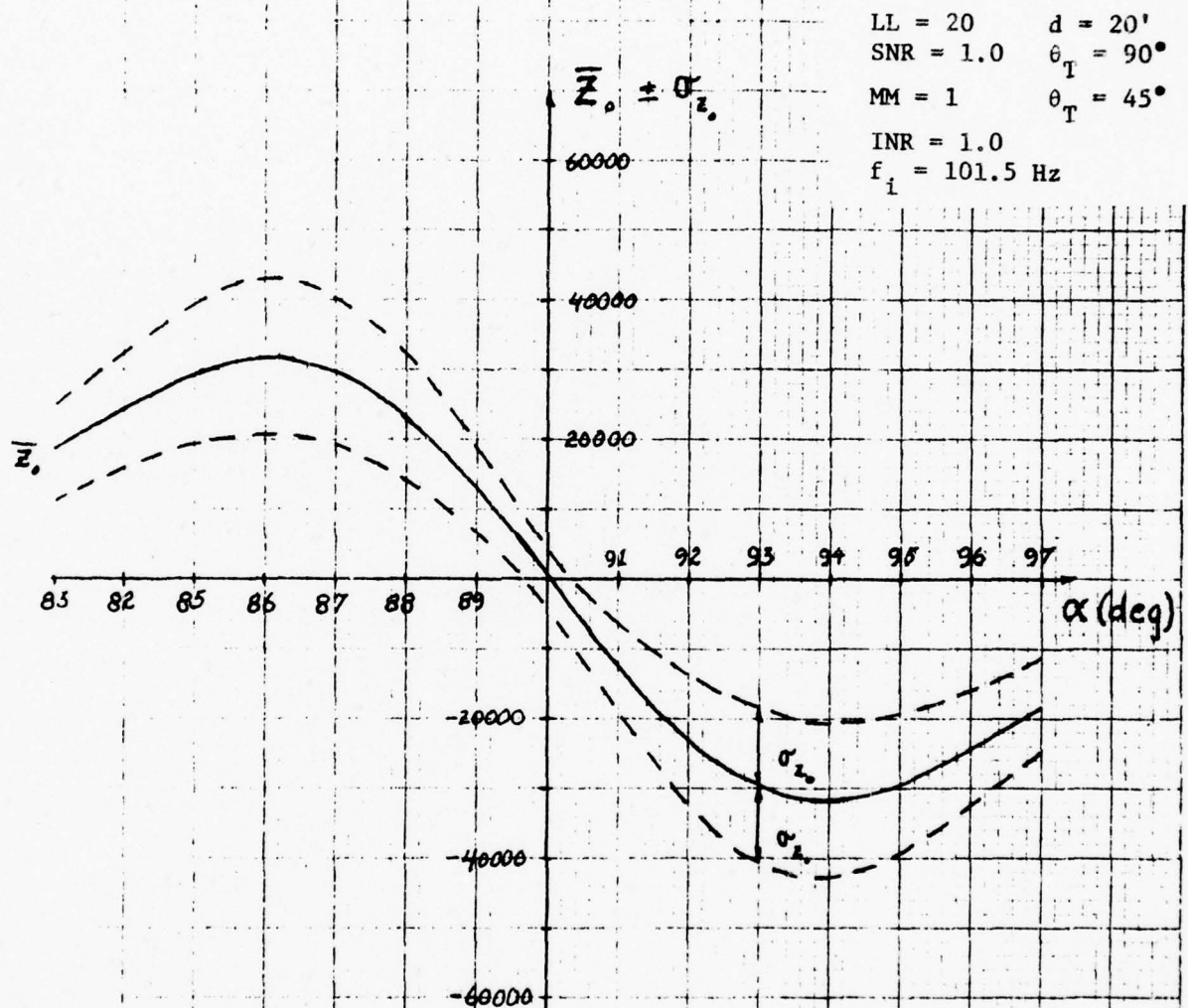


Figure 6.6 - Approximate, Theoretical SBT Mean and Standard Deviation; 20 Hydrophone Array

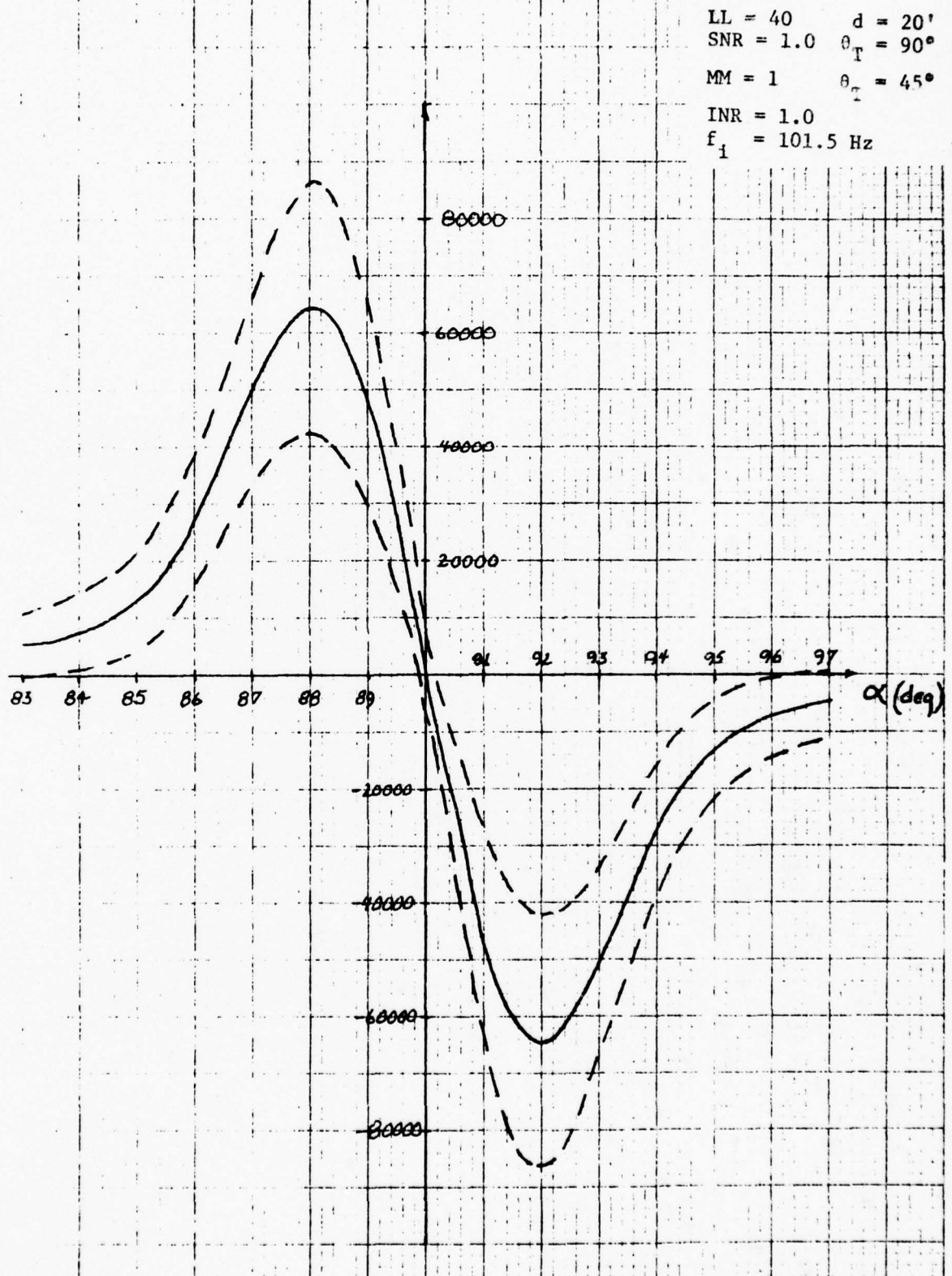


Figure 6.7 - Approximate, Theoretical SBT Mean and Standard Deviation; 40 Hydrophone Array

linearity. For this reason, the simulation estimates were formed from output values in the 88-92 degree region for $LL = 20$ and in the 89-91 degree region for $LL = 40$.

The extreme costs associated with exercising the SBT simulation for large arrays mandate still other parameter changes. The cost of exercising a digital computer simulation results mainly from processor (CPU) run time and core memory usage. Figure 6.8 illustrates the time and memory requirements for exercising the simulation on Catholic University's DEC KL-10 computer. Processing time in CPU minutes is given by the left ordinate while memory usage in kilo-core-seconds is given by the right ordinate. A kilo-core-second is defined as 1024 words of CPU memory used per second of run time. Figure 6.8 reflects the costs required to obtain 20 bearing estimates, at 13 beam positions per estimate for a single value of the mean interference bearing, θ_I . The core memory usage and CPU time are respectively about 100 and 9.5 times greater for 40 hydrophones than for 10 hydrophones. Due to these higher costs, only nine beam positions are used to form each of the 20- and 40-hydrophone bearing estimates. In this investigation, we must, unfortunately, accept the expected increase in bearing error associated with a decrease in the number of points in the LSE line fit. In subsequent investigations, it might be possible to circumvent this trade off by optimizing the simulation software programs and by even employing special, dedicated hardware in some applications.

Other required parameter changes are the mutual interference separations and target-to-interference separations that were addressed by the simulation exercises. Unlike the theoretical metrics, the simulation error metrics are only evaluated for mutual interference separations of 3° and also for only two separations of target and interference (i.e. $|Y|$).

DEC System KL-10 Costs.
Costs Reflect 20 Bearing
Estimates at 13 Beam
Positions per Estimate

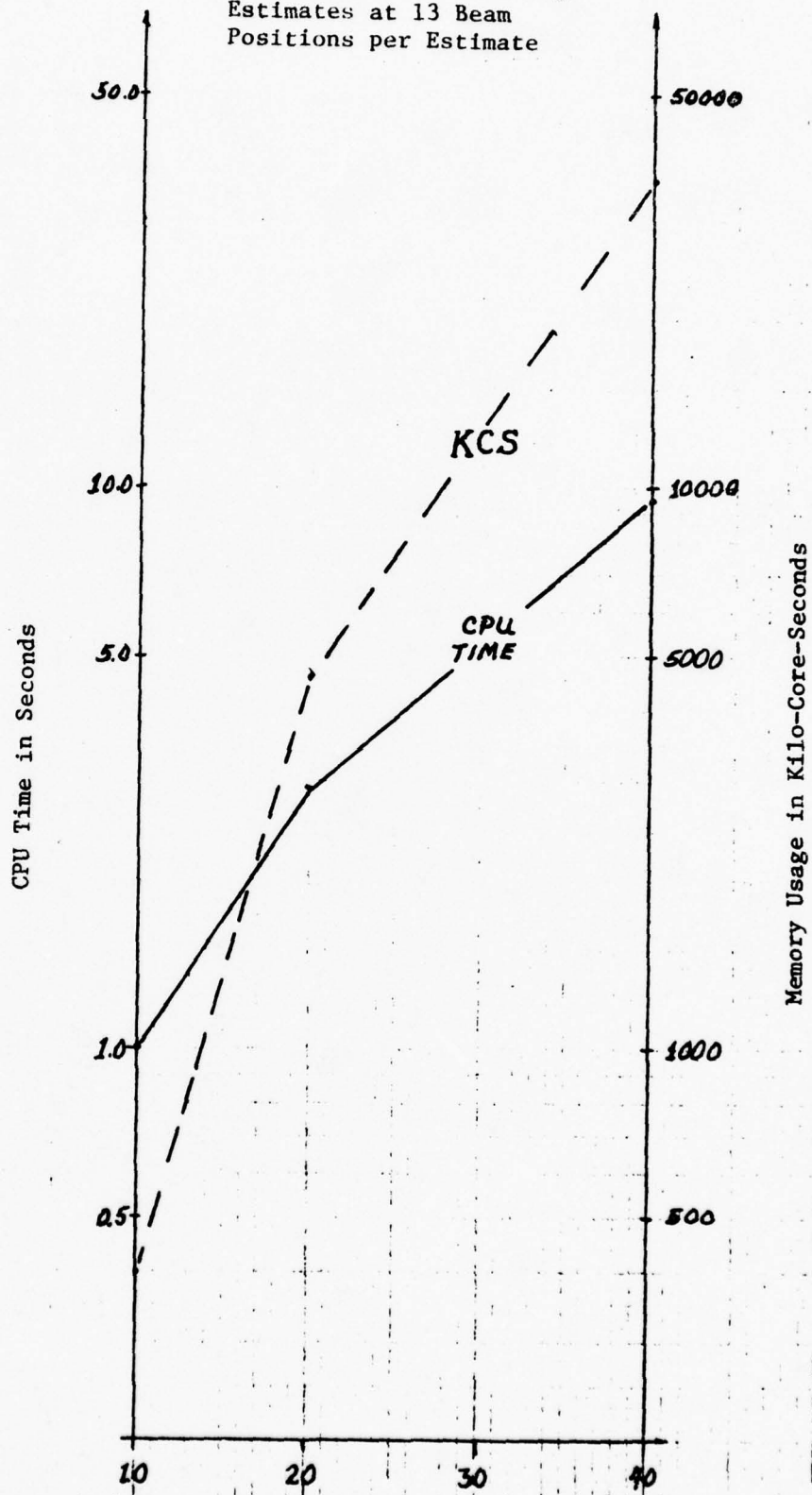


Figure 6.8 - Computational Costs - SBT Simulation

These were the "peak error" interference separations and the case of coincident target and interference. Recall that in the baseline investigation results for remotely positioned interferers (figure 5.5) the SBT standard deviation of estimation error is independent of $\Delta\theta$ and has a small linear dependence on MM. Since similar results are expected for the extended array sizes, the bearing error for remotely positioned interferers was only obtained for the MM = 1 case.

To summarize, the theoretical results are presented for $\Delta\theta$ equal 3° and 6° while the simulation results are presented only for $\Delta\theta = 3^\circ$. Furthermore, each simulation estimate for 20 and 40 hydrophones is formed from the SBT outputs at nine beam positions spanning, respectively, the 88-92 and 89-91 degree sectors of steering angles. The sample size remains at 20 runs per sample.

The estimation standard deviation and bias metrics are presented in figures 1-5 and figures 6-10 of appendix E, respectively. In each figure, the baseline results for a 10-hydrophone array are repeated for comparison with the 20- and 40-hydrophone results. An immediate observation from these figures is the profound effect that the decrease in resolution beamwidth has on both standard deviation and bias error metrics. These effects are the shift of the error peaks in the direction of the target bearing and the "oscillatory" behavior of the metrics for multiple, resolvable interferers. From Cox's previous study of target resolution [7], the optimal and conventional beamwidths have been computed for the parameters of interest and are shown in table 6.1. This table and the results in appendix E indicate that the standard deviation of error peaks for single and multiple, closely spaced interferers occur approximately one resolution beamwidth from the target bearing. Widely spaced interferers should affect the ML

TABLE 6.1
RESOLUTION BEAMWIDTHS FOR EXTENDED
ARRAY LENGTHS [7]

	Beamformer Configuration (# Sensors)	Resolution Beamwidth	Phase Separation, $ Y $ ⁵
Optimal Beamformer	10	10°	0.44
	20	4.6°	0.20
	40	1.96°	0.09
Conventional Beamformer	10	14.2°	0.63
	20	7.1°	0.32
	40	3.55°	0.16

⁵The tabulated $|Y|$ is the phase separation between the target (at $\theta_p = 90^\circ$) and an interference cluster centered at one resolution beamwidth to either side of it.

and SBT processors independently and result in multiple, equally spaced peaks in the standard deviation of error metrics. This "picket fence" effect is indeed observed in figure E.5 for $LL = 40$. When each interferer acts independently of adjacent interferers, the error metric will be equal in magnitude and separated by $\Delta\theta$. The most remote error peak (i.e. the largest $|Y|$ location) should occur for

$$\theta_I = \theta_T \pm \left(BW_{RES} + (MM - 1) \cdot \frac{\Delta\theta}{2} \right),$$

where BW_{RES} is the resolution beamwidth. Ideally, these standard deviation extrema should occur for $\Delta\theta = 6^\circ$ and $LL = 40$ at the positions indicated by the small arrows in figure E.5. It is seen that the actual extrema locations and the predicted locations (i.e. the arrows) are in excellent agreement for $LL = 40$ and $\Delta\theta = 6^\circ$. However, $\Delta\theta$ is not quite large enough to produce standard deviation of error peaks of equal magnitudes.

As mentioned earlier, the peak SBT bias error for larger array sizes (see figures E.5 through E.10) is not only smaller in magnitude but also occurs closer to the true target bearing. Unlike the standard deviation metrics, it is quite difficult to perceive the underlying relationship between the location and "shape" of the peak bias-error and the resolution power of the SBT processor. One phenomena worth noting, however, is the effect of very widely spaced interferers on the SBT bias error. The resolution beamwidth of the 40-hydrophone array is small enough to cause the appearance of multiple local extrema for $\Delta\theta = 6^\circ$ (see figures E.8 and E.10). These peaks illustrate the "push-pull" effect that directional noise has on the bearing estimation bias. As an interferer closes on the target from remote bearings, the target bearing estimate is increasingly

"pulled" or biased, in the direction of the interferer. When the point of peak bias is reached, the interferer is effectively "pushing" the bearing estimate back toward the target. In figures E.8 and E.10 each interferer in the clusters of 2 and 4 interferers are seen to exert a "push-pull" effect on the bearing estimates as shown, respectively, by the two and four local maxima (minima for $Y < 0$). These local maxima indicate that at some Y -separation each interferer acts as the primary cause of estimation bias. It is unclear from the magnitudes of these local maxima to just what extent each interferer is the primary cause of bias error. Other than these basic qualitative statements, little can be said concerning the relationship between peak bias error location and the array resolution beamwidth.

The simulation standard deviation metric is again larger than the approximate, theoretical metric. It is also noted that there is some discrepancy between the simulation and theoretical bias metrics for small bias magnitudes. In the previous section, a similar discrepancy occurred at low bias magnitudes but appeared to decrease in severity as the bias magnitude increased (i.e. figure D.12, $\text{SNR} = 2.0$). It is believed that these discrepancies are similar -- both most likely resulting from the simulation bearing resolution limit and the small ($N = 20$) sample size.

We can again obtain a better idea of the effects of extended array size on bearing estimation error by examining the standard deviation of error for remote, peak and coincident interferers and the peak bias error as functions of the array size. The standard deviation metrics for remotely positioned interferers is shown in figure 6.9 as a function of the extended range of array sizes. Since the error metrics appear linear in logarithmic

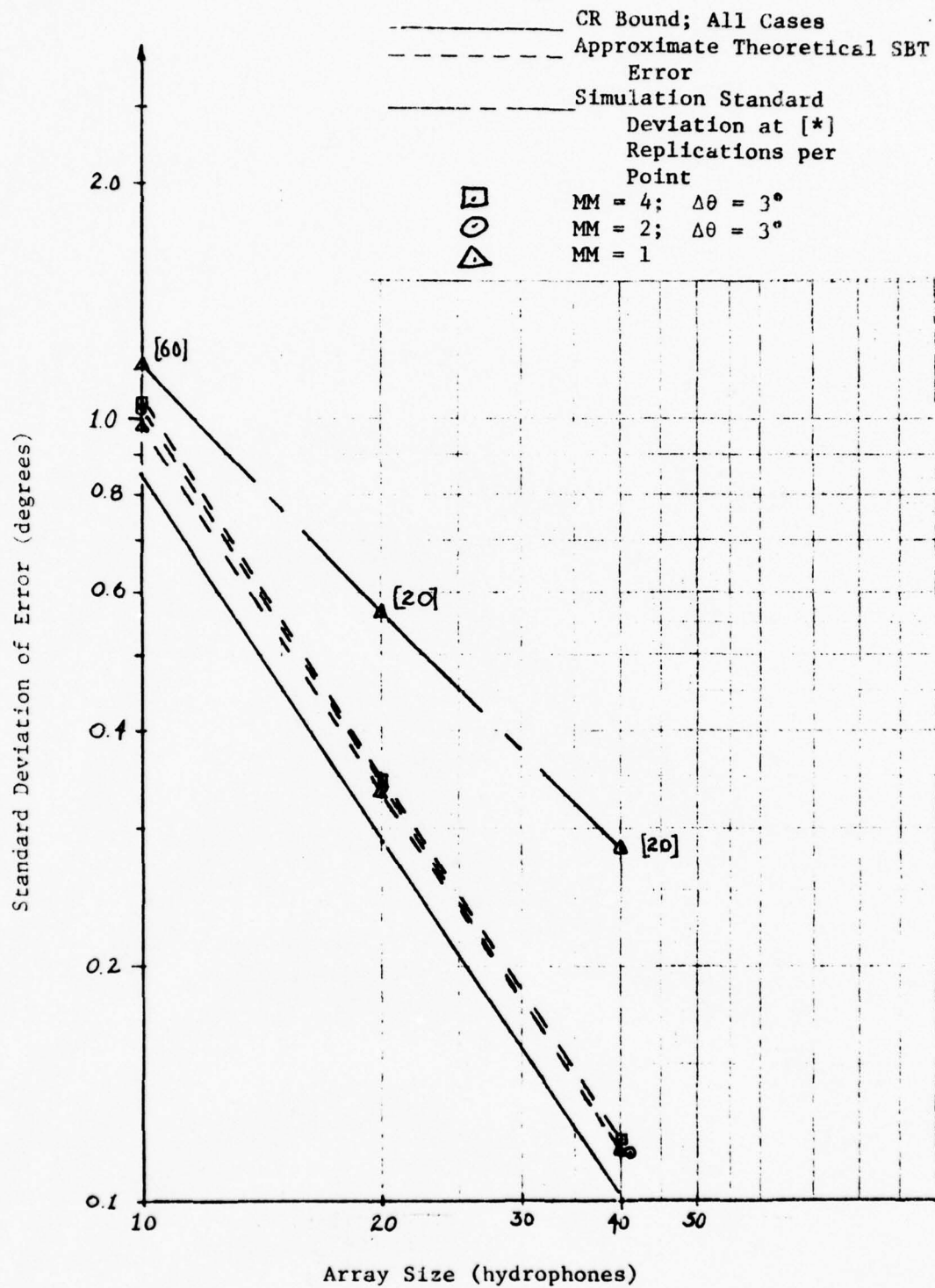


Figure 6.9 - Standard Deviation of Error; Remotely Positioned Interference

coordinates, the standard deviation metrics are exponential functions of LL. Furthermore, the slopes of the theoretical metrics indicate that the standard deviation of the bearing estimates varies approximately in inverse proportion with the $3/2$ power of array size, LL. On the other hand, the slope of the simulation metric is -1 indicating a simple, inverse proportionality. In a previous paper [19], MacDonald and Schultheiss addressed the SBT bearing estimation performance in the presence of an incoherent noise field. They indicate that in isotropic noise the standard deviation of bearing error for high SNR will vary as a function of $LL^{-3/2}$ [19, p. 42, equation 38]. Consequently, since it has been shown that remotely positioned interferers have little effect on the estimation standard deviation (e.g., see figure 5.5 and the relative isotropic-noise error magnitudes in figure E.1), we must conclude that $LL^{-3/2}$ dependence indicated by the theoretical metrics is correct and that the simulation metric behavior is misleading.

Recall that there was an abrupt increase in the simulation-target discrepancy in section 6.1 when SNR was increased from 1.0 to 2.0 (see figure 6.2). The behavior of the simulation metric shown in figure 6.9 reflects a similar phenomena, i.e. the larger arrays provide a higher gain, or coherent signal level, and as before cause a larger discrepancy. The smaller slope of the simulation metric is attributed to a limit on bearing resolution by the simulated estimation algorithm. Note that there is a smaller sample size (20 runs) and fewer beam positions per estimate (9) for $LL = 20$ and 40 than for $LL = 10$.

A new twist in the simulation - theoretical discrepancy occurs in figure 6.10 where the peak standard deviation is shown as a function of array size. At $LL = 20$ hydrophones, the simulation metric seems to imply

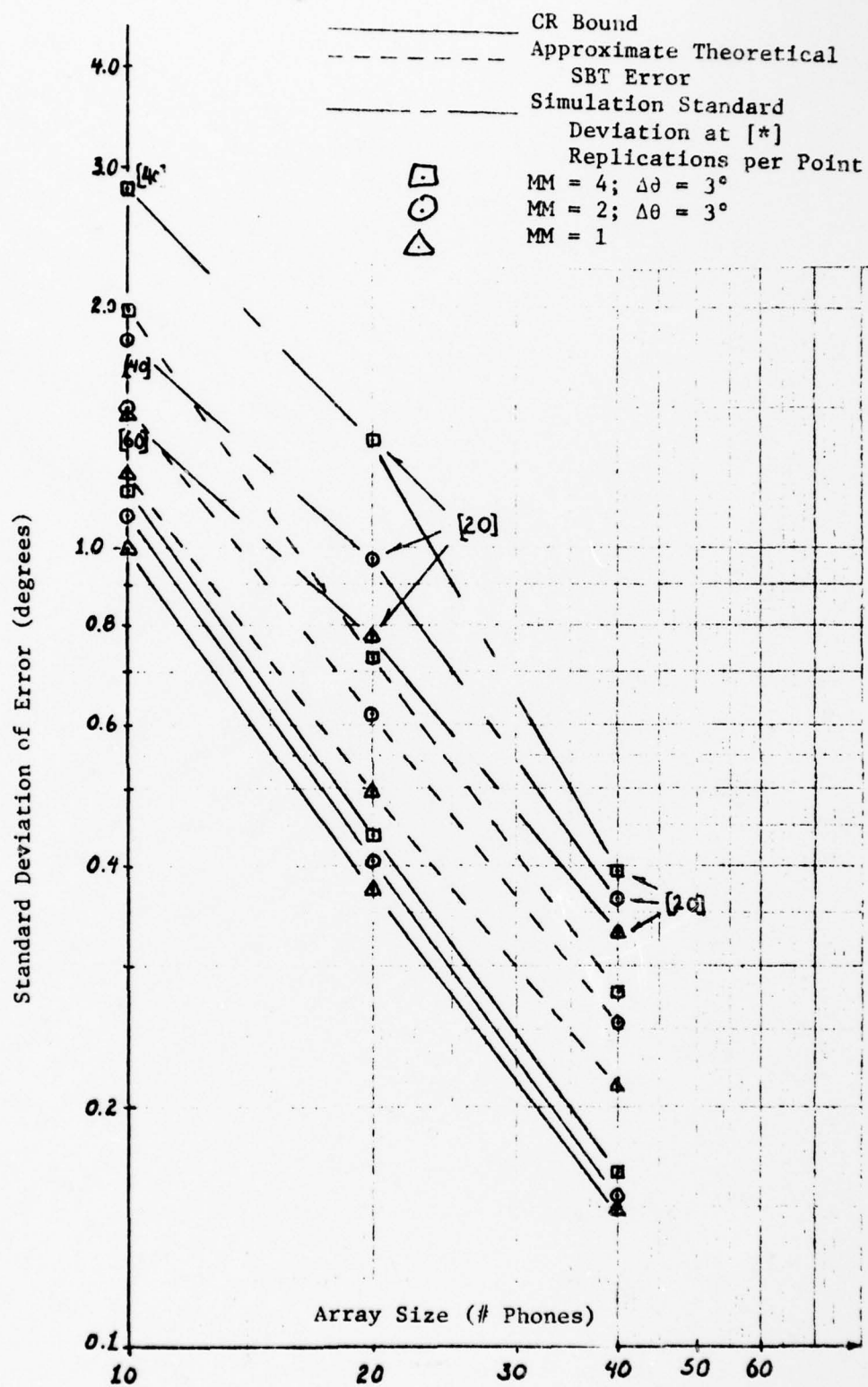


Figure 6.10 - Peak Standard Deviation of Error;
 Intermediate Separation

a slope of -1 while at $LL = 40$ this slope has increased and the simulation metric essentially mirrors the theoretical trend.

The theoretical metrics are all similar in their LL -dependency, which has decreased from $LL^{-1.5}$ that we observed for the remote interferers to $LL^{-1.37}$ in this case -- a small but notable change. Note also that the peak error is dependent on number and separation of interferers. This contrasts with little or no dependence on MM and $\Delta\theta$ shown by these metrics for remotely positioned interferers.

For the case of coincident target and interference, the standard deviation of error metrics are shown in figure 6.11. The CR bound is again seen to be higher than the theoretical SBT metric for some LL values and a difference in the slopes of the two SBT metrics is again apparent. A new observation is the tendency of the standard deviation of error metrics to increase as the number of closely spaced interferers increases. For one coincident interferer, the error is proportional to $LL^{-3/2}$ while for 4 "coincident" interferers it is approximately proportional to LL^{-1} . Thus, there is a slower improvement in estimation accuracy with increasing array size for larger number of interferers.

As a final indicator of the effects of anisotropic noise, consider the behavior of the peak SBT bias relative to array size as summarized in figure 6.12. These results indicate a large improvement in bias error for larger array sizes. A fourfold increase in the number of hydrophones shows that the theoretical bias metrics decrease by factors of between 3 and 5 while the simulation metrics decrease by factors between 9 and 13. As in the other cases, this theoretical-simulation bias discrepancy is attributed to the sample size and the LSE line fit.

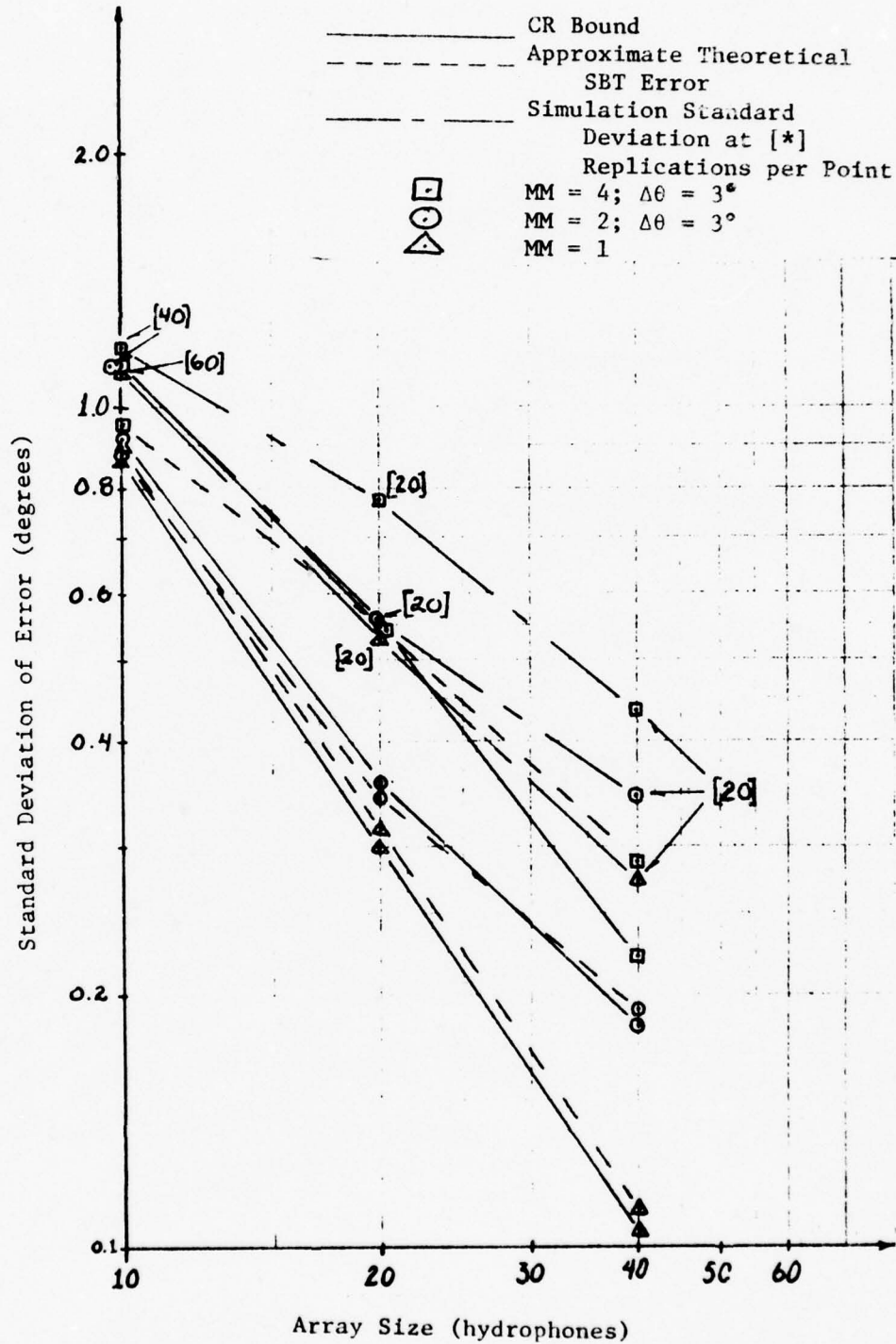


Figure 6.11 - Standard Deviation of Error;
 Coincident Interference

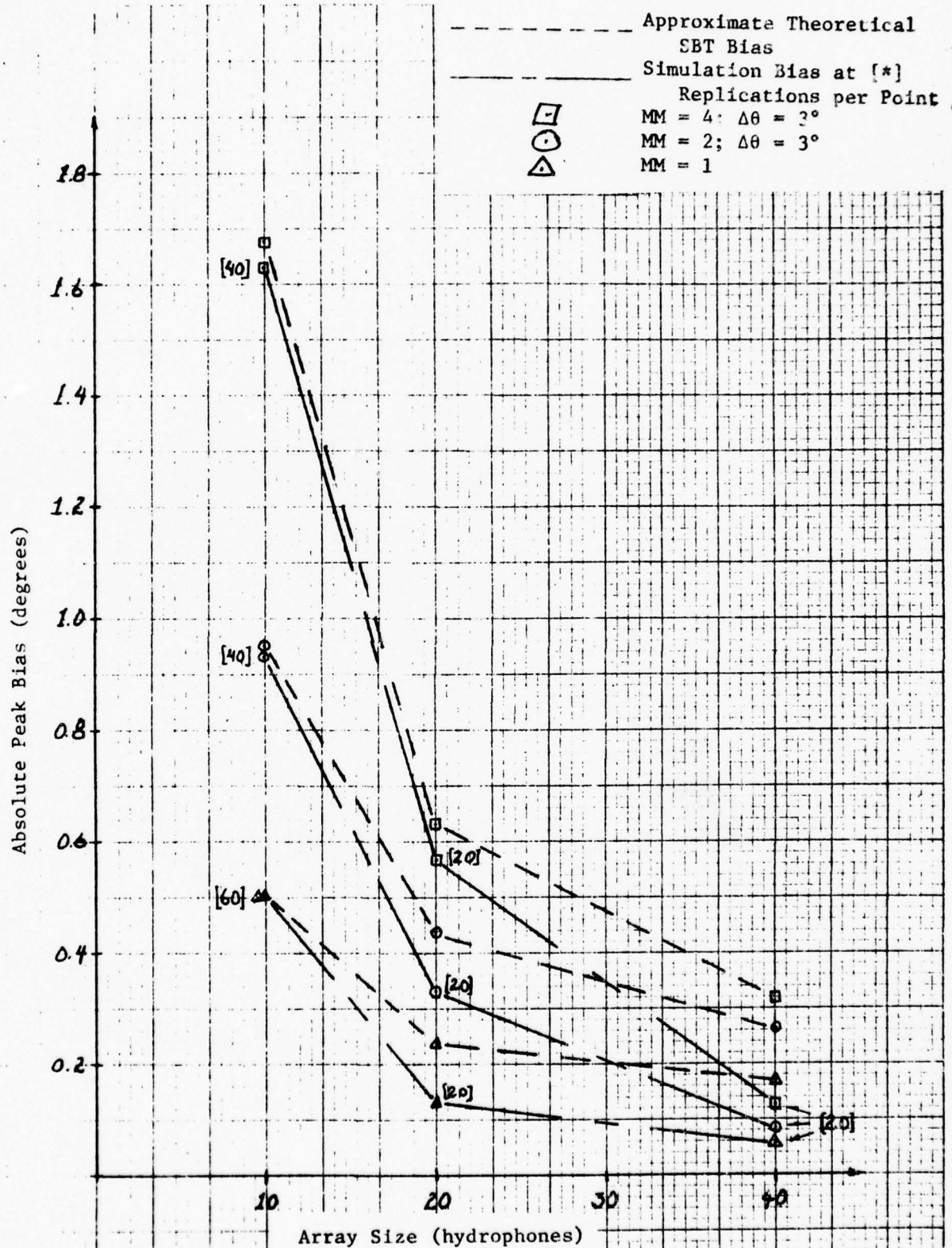


Figure 6.12 - SBT Bias Error Metrics;
Absolute Peak Value

CHAPTER VII

CONCLUSIONS

7.1 - Summary

In many source bearing estimation problems, highly anisotropic noise fields occur as a rule rather than an exception. Such problems generate interest in the performance of both optimal and sub-optimal, fixed-design, sonar array processors. Non-adaptive optimal processors represent a design goal while simplicity and economy motivate the use of fixed-design, sub-optimal processors. Consequently, this research has investigated the effects of highly anisotropic noise fields on several performance metrics for the maximum-likelihood (non-adaptive) estimator and the conventional, split-beam tracker. This study has addressed target tracking problems where the signal-to-total-interference ratio is large ($S/MI > 1$) and where true target bearings are approximately broadside.

We have considered the performance of the optimal bearing estimator from the standpoint of the maximum likelihood estimation criterion. The performance of the maximum likelihood estimator is characterized in terms of a bound on the standard deviation of estimation error, thus avoiding problems associated with solutions to the maximum likelihood equation. A particularly pleasing metric for target tracking problems is the Cramer-Rao bound. Chapter 2 sought to derive a theoretical expression for the Cramer-Rao bound which is expressable in terms of the inverse noise covariance matrix. Although the algebraic inversion of the covariance matrix of highly anisotropic noise is intractable, numerical matrix inversion algorithms permit evaluation of this expression. The Cramer-Rao bound is derived

for a stationary, Gaussian signal and noise model. All propagating components of the acoustic field are assumed to be plane wave fronts arising from sources located in the far-field of the receiving array. The noise field consists of isotropic, uncorrelated ambient noise and MM directional interferences.

The effects of the same anisotropic noise field on bearing estimation by the split-beam tracker (SBT) is examined theoretically in chapter 3. The sub-optimal SBT estimates a source bearing from the cross-correlation lag time of two split beam outputs. The steering angle at which the processor output crosses zero identifies the bearing estimate. Chapter 3 develops a theoretical SBT output expression and derives further expressions for the mean and variance of the SBT output. Under restrictive assumptions on the steering-angle dependence of the SBT output mean and variance, an approximate expression for the bearing estimation variance is derived.

In the absence of experimental bearing estimation results, a digital SBT simulation is developed to provide statistical measures -- the sample mean and variance -- of SBT performance. The SBT is simulated in the frequency domain to avoid potential problems arising from digital models of certain temporal operations (e.g. time differentiation). This approach is facilitated by elimination of the Fourier transformer requirement through direct generation of the Fourier random deviates. Consequently, the SBT processor algorithm is available from the results of chapter 3. The bearing estimation algorithm is configured as the zero-crossing of the LSE line fit to the outputs at ISTEER beam positions around the target bearing.

Chapter 5 identifies the CR bound as the sole performance metric of the optimal (ML) estimator. Also defined are simulation and approximate,

theoretical measures of SBT estimation bias and standard deviation. These optimal and sub-optimal performance metrics are evaluated for a baseline set signal, noise and array parameters. The functional dependence of the performance measures on target-to-interference separation is presented for 1, 2, and 4 interferers with mutual interference separations of 3, 6, and 9 degrees. For a more restricted set of interference parameter values, the performance results are obtained for extended SNR and array size parameters. Chapter 6 presents and analyzes the performance metrics for an SNR of 0.5 and 2.0 (baseline - 1.0) and subsequently for array sizes of 20 and 40 hydrophones (baseline - 10 hydrophones).

The major contributions of this research are described below:

- 1) The Cramer-Rao bound on the variance of any unbiased estimator as derived in chapter 2 is a new contribution to the literature. This result is applicable to completely arbitrary (complex), total-noise covariance matrices \underline{K}_N and requires only the assumptions of linear receiving array and stationary, Gaussian processes. It is thus more general and widely applicable than existing results.
- 2) Although it is a fairly straightforward procedure, the extension of the theoretical and simulation SBT error expressions in chapters 3 and 4 to include multiple uni-directional interferers is believed to be original with this dissertation. These expressions permit further study into the effects of changes such as in array geometry and degrees of anisotropy. With slight modification, it should also be easy to address arbitrary (spatially distributed) interference fields.
- 3) The numerical results presented in chapters 5 and 6 are, to our knowledge, the first quantitative study of the effects of multiple

interferers on passive sonar bearing estimation. Previous known studies have been restricted to single interferers and a special, random-parameter, multi-interferer case.

7.2 - Conclusions

The numerical results presented in chapters 5 and 6 illustrate that performance levels obtainable in the presence of highly anisotropic noise fields are complex functions of the degree of noise anisotropy. The degree of noise field anisotropy ranges between two extremes. At one extreme is the case of multiple coincident interferers acting as a single interference with a level of $MM \cdot I$. The other extreme is MM , widely separated interferers each affecting the estimation performance independently (at different bearings, of course). The transition between different phenomena at each extreme accounts for the complex behavior of the bearing estimation performance metrics. Specifically we can make the following conclusions:

- 1) All three standard deviation metrics exhibit similar behavior in each of three distinct regions of target-to-interference separation. For remotely positioned interference clusters (figure 5.5), the Cramer-Rao bound is unaffected by the directional interference thus indicating a complete interference rejection by the optimal processor. The SBT interprets an increase in the number of remote interferers as a slight increase in equivalent isotropic noise level. Again, the separation of interferers is irrelevant. At intermediate separations of the target and interference-cluster a peak, or relative maxima, is observed for all standard deviation metrics. This peak occurs when the target and closest interference are approximately one resolution beamwidth apart. The degradation of the SBT performance over the optimal estimator in

this intermediate region is primarily affected by the interference separation, $\Delta\theta$ (see figure 5.6). In other words, the performance loss of the SBT relative to the CR bound increases dramatically with increases in the total interference power received from bearings approximately one resolution beamwidth on either side of the source bearing. When the target and interference cluster are coincident, the effect of decreasing interference separation is again dramatic. For small separations, the SBT interprets an interference cluster in this region as a component of the source field. The effect is an increase in the received coherent field and a corresponding decrease in standard deviation of error (often below the CR bound). As $\Delta\theta$ increases, the amount of interference power concentrated one beamwidth to either side of the source bearing increases and hence the standard deviation of error increases as $\Delta\theta$ increases (figure 5.7). The same phenomena affects the CR bound but at a slower rate.

- 2) Multiple interfering noise sources bias the source bearing estimates of the SBT in the direction of the interference cluster. Peak bias error occurs when the closest interference is within one resolution beamwidth of the source. Peak SBT bias increases linearly with decreasing interference separation and appears to be directly proportional to the number of interferers (figure 5.11).
- 3) In the presence of multiple interfering noise sources, the ML and SBT standard deviation metrics are approximately inversely proportional to the square-root of SNR (figures 6.2 - 6.4). For isotropic noise, the same $(\text{SNR})^{-\frac{1}{2}}$ dependence occurs [19] and, hence, the degree of noise anisotropy is seen to affect only the overall random error magnitude and

not its functional dependence on SNR. The peak SBT bias error is inversely proportional to SNR and directly proportional to the number of closely spaced interferers (figure 6.5). Consequently, the peak SBT bias is approximately inversely proportional to the signal-to-total-interference ratio, $S/MM \cdot I$, arriving within a resolution beamwidth of the target.

- 4) The ML and SBT standard deviations of error for multiple, remotely positioned interferers (like the error for isotropic noise [19]) vary inversely with $3/2$ power of array size (figure 6.9). The peak standard deviation metrics decrease slower with increasing array size, varying in proportion to $LL^{-1.37}$ (figure 6.10). For coincident target and interference cluster, the array size dependence ranges from $LL^{-3/2}$ to about LL^{-1} showing a weakening dependence on LL as the number of interferers increases (see figure 6.11). Also, the SBT bias metrics exhibit a dramatic decrease with higher resolution (larger LL) -- the improvement being most significant with the larger numbers of interferers.
- 5) With few exceptions, the theoretical and simulation measures of SBT performance consistently exhibit similar behavior although the simulation standard deviation is typically higher than the theoretical measure. In those cases where a bias metric discrepancy is suggested, the simulation bias tends to be lower than its theoretical counterpart. Four possibilities are suggested in section 5.3 as contributing causes of this discrepancy.

7.3 - Recommendations for Further Work

A natural extension of this research would investigate the effects of multiple, high-level interferers and distributed (possibly non-Gaussian), anisotropic noise. Since it is apparent that frozen-design, sub-optimal

processors cannot tolerate nearby high-level interference, nulling or interference-cancelling sub-optimal processors and adaptive, maximum-likelihood estimators must be examined. Although considerable research has been done on optimal, adaptive estimation, we are aware of only Macdonald's [18] study of sub-optimal processor structures in the presence of a single, high-level interference. Also of interest is the possibility of improving processor discrimination against multiple, coherent interferences (high and low level) with three-dimensional, planar, and non-uniform linear array geometries. Several authors (e.g. [18], [19], [5]) have examined the performance of non-uniform linear (usually symmetric) passive sonar arrays for the isotropic and single-interference cases.

The methodology of this investigation could also be expanded to include the effects of multiple, non-stationary interferers and non-stationary signals. Propagating components are often non-stationary due to multipath transmissions and platform dynamics. Noise transients and sonar countermeasures are also sources of non-stationary interference. Such an investigation might prove fruitful for certain cases of non-stationarity (e.g. non-stationary noise processes describable as locally stationary [3]).

The Cramer-Rao bound was derived in chapter 2 under the tacit assumption that the source bearing was the only unknown parameter in the signal-plus-noise model. This is, of course, untrue in practice. It would be interesting to examine the behavior of the CR bound for the case of multiple, unknown parameters. This is especially so in light of the sub-optimal processor's assumed ignorance of the directional noise parameters. Such an investigation would require derivations (such as in chapter 2) of the J^2 elements of the Fisher's information matrix [33]

where J is the number of unknown signal, noise and interference parameters. The CR bound on the variance of any unbiased estimator of the j th unknown parameter is, by definition, the $(jj)^{\text{th}}$ element of the inverse Fisher's information matrix.

Another possible area of investigation might address active sonar processor performance in the presence of multiple interferences. Here, source range and range-rate are also unknown, but required parameters. Although the directional noise sources are commonly signal dependent in this case (target-like scatterers), sonar countermeasures possibly constitute signal-independent interference. Background noise transients may also represent directional, signal-independent interference.

APPENDIX A

DERIVATION OF THE LOG-LIKELIHOOD RATIO

Equation (2-9) defines the Fourier characterization of the total, received data vector as

$$\vec{\bar{X}}_D = \left[X_1(j\omega_0), X_2(j\omega_0), \dots, X_L(j\omega_0), X_1(j\omega_1), \dots, X_L(j\omega_N) \right]' \quad (A-1)$$

$$\text{where } X_\ell(j\omega_1) \triangleq \int_0^T x_\ell(t) e^{-j\omega_1 t} dt \quad (A-2)$$

and $x_\ell(t)$ is the real waveform received by the ℓ th hydrophone over the interval $[0, T]$. The definition in (A-2) of the components of $\vec{\bar{X}}_D$ as linear transformations of the real, Gaussian temporal processes suggests that $X_\ell(j\omega_1)$ is also a Gaussian random process. The components of $\vec{\bar{X}}_D$ are by definition, however, complex random processes. The formal definition of a complex, Gaussian process [6] requires that (1) the real and imaginary parts of the complex process be jointly Gaussian and (2) the covariance matrix of the real and imaginary parts be expressible in an anti-symmetric, block-matrix form. By the definition (A-2), the real and imaginary parts of $X(j\omega_1)$ are jointly, Gaussian when $x_\ell(t)$ is a Gaussian process. The second requirement also follows from the definitions in (A-1) and (A-2). The interested reader is referred to chapter 2 of the dissertation of W. Bangs [2] for a detailed proof of the validity of this requirement. Specifically, Bangs proves that

$$E \left\{ \text{Re} \left[\vec{\bar{X}}_D \right] \cdot \text{Re} \left[\vec{\bar{X}}_D' \right] \right\} = E \left\{ \text{Im} \left[\vec{\bar{X}}_D \right] \cdot \text{Im} \left[\vec{\bar{X}}_D' \right] \right\}$$

and

$$E \left\{ \text{Re} \left[\vec{X}_D \right] \cdot \text{Im} \left[\vec{X}_D \right] \right\} = -E \left\{ \text{Im} \left[\vec{X}_D \right] \cdot \text{Re} \left[\vec{X}_D \right] \right\}$$

where $\text{Re} [\cdot]$ and $\text{Im} [\cdot]$ denote the real and imaginary parts and where \vec{X}_D is defined in (A-1).

Since the data vector \vec{X}_D satisfies the requirements of a complex, vector Gaussian random process, its pdf can be shown to be [6]

$$p(\vec{X}_D | H_p) = \left(\pi |K_{H_p}| \right)^{-1} \exp \left\{ -\vec{X}_D^* K_{H_p}^{-1} \vec{X}_D \right\} \quad (\text{A-3})$$

where \vec{X}_D is assumed to have a zero-mean,

$p = 0$ or 1 ,

H_1 denotes the signal plus noise hypothesis,

H_0 denotes the noise only hypothesis,

K_{H_p} is the covariance matrix of \vec{X}_D under H_p and,

$|K_{H_p}|$ is the determinant of K_{H_p} .

The covariance matrices are defined as

$$K_{H_p} = E \left\{ \vec{X}_D \vec{X}_D^* | H_p \right\} \quad (\text{A-4})$$

where, from (A-1) and (A-2), an arbitrary element of K_{H_p} is

$$E \left\{ X_m(j\omega_1) X_n^c(j\omega_k) \right\} = \int_0^T dt \int_0^T du E \left\{ x_m(t) x_n(u) \right\} e^{-j(\omega_1 t - \omega_k u)} \quad (\text{A-5})$$

Since $x(t)$ is assumed to be zero mean and stationary we can define the cross-correlation between phones as

$$R_{mn}(\tau) = R_{mn}(t-u) = E \left\{ x_m(t) x_n(u) \right\}$$

and rewrite (A-5) as

$$E \left\{ X_m(j\omega_1) X_n^c(j\omega_u) \right\} = \int_0^T d\tau R_{mn}(\tau) e^{-j\omega_1 \tau} \int_0^T e^{-j(\omega_1 - \omega_k)u} du \quad (A-6)$$

When T is much greater than the correlation time of $x_m(t)$ then the second integral in (A-6) can be approximated as T times the Kronecker delta

$$\delta_{ik} = \begin{cases} 1 & i = k \\ 0 & i \neq k \end{cases}$$

and the first integral approximately equals the cross-power spectral density between the m and n th phones. Hence, we can write

$$E \left\{ X_m(j\omega_1) X_n^c(j\omega_k) \right\} = T X_{mn}(\omega_1) \delta_{ik} \quad (A-6)$$

where $X_{mn}(\omega_1)$ is the cross-power spectral density at ω_1 .

Equation (A-6) allows us to express the $L \times N$ covariance matrix \underline{K}_{H_p} in the following block-diagonal form

$$\underline{K}_{H_p} = \begin{bmatrix} \underline{K}_{H_p}'(\omega_0) & \underline{0} & \dots & \underline{0} \\ \underline{0} & \underline{K}_{H_p}'(\omega_1) & & \underline{0} \\ \vdots & & \ddots & \\ \underline{0} & \underline{0} & \dots & \underline{K}_{H_p}'(\omega_N) \end{bmatrix} \quad (A-7)$$

where $\underline{0}$ is an $L \times L$ null matrix.

$\underline{K}_{H_p}'(\omega_i) = E \left\{ \vec{X}(\omega_i) \vec{X}^*(\omega_i) \right\}$ is the $L \times L$ cross-covariance matrix at the i th frequency, and

$\vec{X}(\omega_i)$ is the vector of L components of X_D corresponding to ω_i .

The block diagonal form of the total covariance matrix in (A-7) is the objective of the Fourier characterization of the received data given by equations (A-1) and (A-2).

With \vec{X}_D rewritten in the form

$$\vec{X}_D = \left[\vec{X}'(\omega_0), \vec{X}'(\omega_1), \vec{X}'(\omega_2), \dots, \vec{X}'(\omega_N) \right]' \quad (\text{A-8})$$

and K_{H_p} in the block diagonal form of (A-7), it is easy to show that the probabilities defined in (A-3) become

$$P(\vec{X}_D | \theta_T) = \left(\pi \prod_{i=1}^N |K_{H_p}'(\omega_i)| \right)^{-1} \exp \left\{ - \sum_{i=1}^N \vec{X}'(\omega_i) K_{H_p}'^{-1}(\omega_i) \vec{X}(\omega_i) \right\} \quad (\text{A-9})$$

The log-likelihood ratio is by definition,

$$\ell(\vec{X}_D | \theta_T) = \ell_n \left\{ \frac{P(\vec{X}_D | H_1, \theta_T)}{P(\vec{X}_D | H_0)} \right\}$$

and upon substitution of (A-9) becomes

$$\begin{aligned} \ell(\vec{X}_D | \theta_T) &= \ell_n \left(\prod_{i=1}^N \frac{|K_{H_0}'|}{|K_{H_1}'|} \right) - \sum_{i=1}^N \left\{ \vec{X}'(\omega_i) K_{H_1}'^{-1} \vec{X}(\omega_i) - \vec{X}'(\omega_i) K_{H_2}'^{-1} \vec{X}(\omega_i) \right\} \\ &= \sum_{i=1}^N \ell_n \left\{ \frac{|K_{H_0}'|}{|K_{H_1}'|} - \vec{X}'(\omega_i) K_{H_1}'^{-1} \vec{X}(\omega_i) + \vec{X}'(\omega_i) K_{H_0}'^{-1} \vec{X}(\omega_i) \right\} \quad (\text{A-10}) \end{aligned}$$

where, for simplicity, the frequency subscripts have been suppressed and the "prime" notation used in defining the submatrices in (A-7) has been dropped.

Evaluation of the inverse of K_{H_1} is facilitated by the following matrix identity for matrices of the form

$$\underline{A} = \underline{b} \underline{b}^* + \underline{C} :$$

$$\underline{A}^{-1} = \underline{C}^{-1} - \frac{\underline{C}^{-1} \underline{b} \underline{b}^* \underline{C}^{-1}}{1 + \underline{b}^* \underline{C}^{-1} \underline{b}} \quad (\text{A-11})$$

Equation (A-11) is easily verified after a minor amount of algebraic manipulation. Recall from equation (2-20) that the data covariance under hypothesis H_1 is

$$\underline{K}_{H_1} = TS \underline{a} \underline{a}^* + \underline{K}_N \quad (\text{A-12a})$$

and, when no signal is present,

$$\underline{K}_{H_0} = \underline{K}_N \quad (\text{A-12b})$$

where \underline{K}_N is the covariance matrix (at the implied frequency) of the Fourier characterization of the total received noise vector. Combining (A-11) and (A-12a),

$$\begin{aligned} \underline{K}_{H_1}^{-1} &= \underline{K}_N^{-1} - \frac{TS \underline{K}_N^{-1} \underline{a} \underline{a}^* \underline{K}_N^{-1}}{1 + TS \underline{a}^* \underline{K}_N^{-1} \underline{a}} \\ &= \underline{K}_N^{-1} - \sigma_T^2 \underline{K}_N^{-1} \underline{a} \underline{a}^* \underline{K}_N^{-1} \end{aligned} \quad (\text{A-13})$$

where $\sigma_T^2 \triangleq \frac{TS}{1 + TS \underline{a}^* \underline{K}_N^{-1} \underline{a}}$

Substituting (A-12b) and (A-13) into (A-10), yields

$$\ell(x_D | \theta_T) = \sum_{i=1}^N \left\{ \ell_n \frac{|\underline{K}_{H_0}|}{|\underline{K}_{H_1}|} + \sigma_T^2 \underline{X}^* \underline{K}_N^{-1} \underline{a} \underline{a}^* \underline{K}_N^{-1} \underline{X} \right\} \quad (\text{A-14})$$

The ratio of matrix determinants in (A-14) is evaluated by using the matrix identity

$$\frac{1}{|\underline{A}|} = |\underline{A}^{-1}|$$

and equation (A-13):

$$\begin{aligned} \frac{|\underline{K}_{H_0}|}{|\underline{K}_{H_1}|} &= |\underline{K}_{H_0}| \cdot |\underline{K}_H^{-1}| \\ &= |\underline{K}_N| \cdot \left| \underline{K}_N^{-1} - \sigma_T^2 \underline{K}_N^{-1} \frac{1}{a} \frac{1}{a}^* \underline{K}_N^{-1} \right| \\ &= \left| \underline{I} - \sigma_T^2 \frac{1}{a} \frac{1}{a}^* \underline{K}_N^{-1} \right| \end{aligned} \quad (\text{A-15})$$

The m, n - element of the matrix $\frac{1}{a} \frac{1}{a}^* \underline{K}_N^{-1}$ is

$$\begin{aligned} \frac{1}{a} \frac{1}{a}^* \underline{K}_N^{-1} \quad m,n &= \sum_{p=1}^L e^{-j(m-p)\Delta} \underline{K}_N^{pn} \quad m,n = 1, 2, \dots, L \\ &= e^{-j(m\Delta)} \sum_{p=1}^L e^{+j(p\Delta)} \underline{K}_N^{pn} \end{aligned} \quad (\text{A-16})$$

where $\Delta = \omega_k \frac{d}{c} \cos \theta_T$, $k = 0, 1, \dots, N$ and

\underline{K}_N^{pn} is the p, n -element of \underline{K}_N^{-1} .

Since the row-index m in (A-16) appears only as an exponent, the determinant in (A-15) can be further reduced, since the addition of a constant times the r th row of any matrix to the s th row of that matrix does not change the value of its determinant. Hence, if each element of the first row of $\underline{I} - \sigma_T^2 \frac{1}{a} \frac{1}{a}^* \underline{K}_N^{-1}$ is multiplied by $-e^{-j(r-1)\Delta}$ and added to the corresponding elements in the r th row for $r = 2, 3, \dots, L$, the following expression is obtained:

$$\frac{|K_{H_0}|}{|K_{H_1}|} = \begin{vmatrix} 1-e^{-j\Delta}C_1 & -e^{-j\Delta}C_2 & -e^{-j\Delta}C_3 & \dots & -e^{-j\Delta}C_L \\ -e^{-j\Delta} & 1 & 0 & \dots & 0 \\ -e^{-j2\Delta} & 0 & 1 & \dots & 0 \\ \vdots & \vdots & \vdots & \ddots & \vdots \\ -e^{-j(L-1)\Delta} & 0 & 0 & \dots & 1 \end{vmatrix} \quad (\text{A-17})$$

where $C_s = \sigma_T^2 \sum_{p=1}^L e^{+j(p\Delta)} K_N^{ps}$

In a similar fashion, we can multiply the sth column of (A-17) by $e^{-j(s-1)\Delta}$ and add it to the first column for each $s = 2, 3, \dots, L$ without changing the value of the determinant:

$$\frac{|K_{H_0}|}{|K_{H_1}|} = \begin{vmatrix} 1 - \sum_{s=1}^L e^{-j(s\Delta)} C_s & -e^{-j\Delta}C_2 & -e^{-j\Delta}C_3 & \dots & -e^{-j\Delta}C_L \\ 0 & 1 & 0 & \dots & 0 \\ 0 & 0 & 1 & \dots & 0 \\ \vdots & \vdots & \vdots & \ddots & \vdots \\ 0 & 0 & 0 & \dots & 0 \end{vmatrix} \quad (\text{A-18})$$

Expansion of the determinant down the 1st column yields

$$\begin{aligned}
 \frac{\left| \underline{K}_{H_0} \right|}{\left| \underline{K}_{H_1} \right|} &= 1 - \sum_{s=1}^L e^{-j(s\Delta)} C_s \\
 &= 1 - \sigma_T^2 \sum_{s=1}^L \sum_{p=1}^L e^{-js\Delta} e^{+jp\Delta} \underline{K}_N^{ps} \\
 &= 1 - \sigma_T^2 \sum_{s=1}^L \sum_{p=1}^L e^{+jp\Delta} \underline{K}_N^{ps} e^{-js\Delta} \\
 &= 1 - \sigma_T^2 \underline{a}^* \underline{K}_N^{-1} \underline{a} \\
 &= \frac{\sigma_T^2}{TS} \left[1 + TS \underline{a}^* \underline{K}_N^{-1} \underline{a} - TS \underline{a}^* \underline{K}_N^{-1} \underline{a} \right] \\
 &= \frac{\sigma_T^2}{TS}
 \end{aligned} \tag{A-19}$$

Substitution of (A-19) into (A-14) yields the desired expression for the log-likelihood ratio

$$\ell \left(\underline{X}_D | \theta_T \right) = \sum_{i=1}^N \ell_n \left\{ \left(\frac{\sigma_T^2}{TS} \right) + \sigma_T^2 \underline{X}^* \underline{K}_N^{-1} \underline{a} \underline{a}^* \underline{K}_N^{-1} \underline{X} \right\} \tag{A-20}$$

where

$$\sigma_T^2 = \frac{TS}{1 + TS \underline{a}^* \underline{K}_N^{-1} \underline{a}}$$

$S = S(\omega_1)$ is the signal power spectral density at ω_1 ,

\underline{K}_N^{-1} is the inverse total-noise covariance matrix at ω_1 ,

T is the observation interval,

\underline{a} is the target delay vector at ω_1 , and

\underline{X} is the L -dimensional received-data vector also at the frequency ω_1 .

Equation (A-20) appears as equation (10) in chapter 2 of the text.

APPENDIX B

DERIVATION OF EQUATION (2-21)

The CR bound requires the expected value of the second derivative of the log-likelihood ratio at the arbitrary frequency ω_1 within the bandwidth of the observation vector random process, $\vec{X}(\omega_1)$:

$$\begin{aligned} \frac{\partial^2 \ell_1}{\partial \mu^2} &= \frac{\partial^2}{\partial \mu^2} \ln \frac{\sigma_T}{TS} + \frac{\partial^2 \sigma_T}{\partial \mu^2} \frac{1}{a} * \underline{K}_N^{-1} \frac{1}{X} \frac{1}{X} * \underline{K}_N^{-1} \frac{1}{a} \\ &+ 2 \frac{\partial \sigma_T}{\partial \mu} \frac{1}{a} * \underline{A} * \underline{K}_N^{-1} \frac{1}{X} \frac{1}{X} * \underline{K}_N^{-1} \frac{1}{a} + 2 \frac{\partial \sigma_T}{\partial \mu} \frac{1}{a} * \underline{K}_N^{-1} \frac{1}{X} \frac{1}{X} * \underline{K}_N^{-1} \underline{A} \frac{1}{a} \\ &+ \sigma_T \frac{1}{a} * \underline{A} \underline{A} * \underline{K}_N^{-1} \frac{1}{X} \frac{1}{X} * \underline{K}_N^{-1} \frac{1}{a} + \sigma_T \frac{1}{a} * \underline{K}_N^{-1} \frac{1}{X} \frac{1}{X} * \underline{K}_N^{-1} \underline{A} \underline{A} \frac{1}{a} \\ &+ 2 \sigma_T \frac{1}{a} * \underline{A} * \underline{K}_N^{-1} \frac{1}{X} \frac{1}{X} * \underline{K}_N^{-1} \underline{A} \frac{1}{a} \end{aligned} \quad (B-1)$$

From equation (20) of chapter 2 the expectation of the matrix $\vec{X} \cdot \vec{X}^*$ is

$$E \left\{ \frac{1}{X} \frac{1}{X}^* \right\} = TS \frac{1}{a} \frac{1}{a}^* + \underline{K}_N \quad (B-2)$$

The expectation of the second term in (B-1) is

$$\begin{aligned} \frac{\partial^2 \sigma_T}{\partial \mu^2} \frac{1}{a} * \underline{K}_N^{-1} E \left(\frac{1}{X} \frac{1}{X}^* \right) \underline{K}_N^{-1} \frac{1}{a} &= \frac{\partial^2 \sigma_T}{\partial \mu^2} \frac{1}{a} * \underline{K}_N^{-1} \left[TS \frac{1}{a} \frac{1}{a}^* + \underline{K}_N \underline{K}_N^{-1} \frac{1}{a} \right] \\ &= TS \frac{\partial^2 \sigma_T}{\partial \mu^2} \frac{1}{a} * \underline{K}_N^{-1} \frac{1}{a} \frac{1}{a} * \underline{K}_N^{-1} \frac{1}{a} + \frac{\partial^2 \sigma_T}{\partial \mu^2} \frac{1}{a} * \underline{K}_N^{-1} \frac{1}{a} \\ &= \frac{\partial^2 \sigma_T}{\partial \mu^2} \frac{1}{a} * \underline{K}_N^{-1} \frac{1}{a} \left(\frac{TS}{\sigma_T} \right) \end{aligned} \quad (B-3)$$

The expected value of the sum of the 3rd and 4th terms of (B-1) is

$$\begin{aligned}
 & 2 \frac{\partial \sigma_T^2}{\partial \mu} \left\{ \underline{a}^* \underline{A}^* \underline{K}_N^{-1} E \left\{ \underline{X} \underline{X}^* \right\} \underline{K}_N^{-1} \underline{a} + \underline{a}^* \underline{K}_N^{-1} E \left\{ \underline{X} \underline{X}^* \right\} \underline{K}_N^{-1} \underline{A} \underline{a} \right\} \\
 &= 2 \frac{\partial \sigma_T^2}{\partial \mu} \left\{ TS \left[\underline{a}^* \underline{A}^* \underline{K}_N^{-1} \underline{a} \underline{a}^* \underline{K}_N^{-1} \underline{a} + \underline{a}^* \underline{K}_N^{-1} \underline{a} \underline{a}^* \underline{K}_N^{-1} \underline{A} \underline{a} \right] \right. \\
 &\quad \left. + \underline{a}^* \underline{A}^* \underline{K}_N^{-1} \underline{a} + \underline{a}^* \underline{K}_N^{-1} \underline{A} \underline{a} \right\} \\
 &= 2 \frac{\partial \sigma_T^2}{\partial \mu} \left\{ \left(1 + TS \underline{a}^* \underline{K}_N^{-1} \underline{a} \right) \cdot \left[\underline{a}^* \underline{A}^* \underline{K}_N^{-1} \underline{a} + \underline{a}^* \underline{K}_N^{-1} \underline{A} \underline{a} \right] \right\} \\
 &= 2 \frac{\partial \sigma_T^2}{\partial \mu} \left(\frac{TS}{\sigma_T} \right) \underline{a}^* \left[\underline{A}^* \underline{K}_N^{-1} + \underline{K}_N^{-1} \underline{A} \right] \underline{a} \quad (B-4)
 \end{aligned}$$

Similarly, we take the expectation of the sum of the 5th and 6th terms of (B-1):

$$\begin{aligned}
 & \sigma_T^2 \underline{a}^* \underline{A}^* \underline{A}^* \underline{K}_N^{-1} E \left\{ \underline{X} \underline{X}^* \right\} \underline{K}_N^{-1} \underline{a} + \sigma_T^2 \underline{a}^* \underline{K}_N^{-1} E \left\{ \underline{X} \underline{X}^* \right\} \underline{K}_N^{-1} \underline{A} \underline{A} \underline{a} \\
 &= \sigma_T^2 \left\{ TS \left[\underline{a}^* \underline{A}^* \underline{A}^* \underline{K}_N^{-1} \underline{a} \underline{a}^* \underline{K}_N^{-1} \underline{a} + \underline{a}^* \underline{K}_N^{-1} \underline{a} \underline{a}^* \underline{K}_N^{-1} \underline{A} \underline{A} \underline{a} \right] \right. \\
 &\quad \left. + \underline{a}^* \underline{A}^* \underline{A}^* \underline{K}_N^{-1} \underline{a} + \underline{a}^* \underline{K}_N^{-1} \underline{A} \underline{A} \underline{a} \right\} \\
 &= \sigma_T^2 \left[1 + TS \underline{a}^* \underline{K}_N^{-1} \underline{a} \right] \cdot \left[\underline{a}^* \underline{A}^* \underline{A}^* \underline{K}_N^{-1} \underline{a} + \underline{a}^* \underline{K}_N^{-1} \underline{A} \underline{A} \underline{a} \right] \\
 &= (TS) \cdot \left[\underline{a}^* \underline{A}^* \underline{A}^* \underline{K}_N^{-1} \underline{a} + \underline{a}^* \underline{K}_N^{-1} \underline{A} \underline{A} \underline{a} \right] \quad (B-5)
 \end{aligned}$$

The last term of (B-1), upon taking its expectation, becomes

$$\begin{aligned}
& 2 \sigma_T^2 \frac{\vec{a}}{a}^* \underline{A}^* \underline{K_N}^{-1} E \left\{ \vec{X} \vec{X}^* \right\} \underline{K_N}^{-1} \underline{A} \vec{a} \\
&= 2 \sigma_T^2 \left\{ \frac{\vec{a}}{a}^* \underline{A}^* \underline{K_N}^{-1} (TS \frac{\vec{a}}{a} \underline{a}^*) \underline{K_N}^{-1} \underline{A} \vec{a} + \frac{\vec{a}}{a}^* \underline{A}^* \underline{K_N}^{-1} \underline{A} \vec{a} \right\} \\
&= 2 TS \sigma_T^2 \left| \frac{\vec{a}}{a}^* \underline{A}^* \underline{K_N}^{-1} \underline{a} \right|^2 + 2 \sigma_T^2 \frac{\vec{a}}{a}^* \underline{A}^* \underline{K_N}^{-1} \underline{A} \vec{a} \quad (B-6)
\end{aligned}$$

Substituting (B-3), (B-4), (B-5), and (B-6) into (B-1) yields, for the expected value of the second derivative of ℓ_1 ,

$$\begin{aligned}
E \left\{ \frac{\partial^2 \ell_1}{\partial \mu^2} \right\} &= \frac{\partial^2}{\partial \mu^2} \ell_n \left(\frac{\sigma_T^2}{TS} \right) + \frac{\partial^2 \sigma_T^2}{\partial \mu^2} \frac{\vec{a}}{a}^* \underline{K_N}^{-1} \underline{a} \left(\frac{TS}{\sigma} \right) \\
&+ 2 \left(\frac{\partial \sigma_T^2}{\partial \mu} \right) \frac{TS}{\sigma_T^2} \frac{\vec{a}}{a}^* \left[\underline{A}^* \underline{K_N}^{-1} + \underline{K_N}^{-1} \underline{A} \right] \underline{a} \\
&+ (TS) \cdot \left[\underline{a}^* \underline{A}^* \underline{A}^* \underline{K_N}^{-1} \underline{a} + \underline{a}^* \underline{K_N}^{-1} \underline{A} \underline{A} \underline{a} \right] \\
&+ 2 TS \sigma_T^2 \left| \frac{\vec{a}}{a}^* \underline{A}^* \underline{K_N}^{-1} \underline{a} \right|^2 + 2 \sigma_T^2 \frac{\vec{a}}{a}^* \underline{A}^* \underline{K_N}^{-1} \underline{A} \vec{a} \quad (B-7)
\end{aligned}$$

The underlined terms of equation (B-7) can be combined for further simplification:

$$\begin{aligned}
& TS \left[\underline{a}^* \underline{A}^* \underline{A}^* \underline{K_N}^{-1} \underline{a} + \underline{a}^* \underline{K_N}^{-1} \underline{A} \underline{A} \underline{a} \right] + 2 \sigma_T^2 \frac{\vec{a}}{a}^* \underline{A}^* \underline{K_N}^{-1} \underline{A} \vec{a} \\
&= \sigma_T^2 \left\{ 2 \underline{a}^* \underline{A}^* \underline{K_N}^{-1} \underline{A} \underline{a} + \left(1 + TS \underline{a}^* \underline{K_N}^{-1} \underline{a} \right) \left[\underline{a}^* \underline{A}^* \underline{A}^* \underline{K_N}^{-1} \underline{a} + \underline{a}^* \underline{K_N}^{-1} \underline{A} \underline{A} \underline{a} \right] \right\} \\
&= 2 \sigma_T^2 (TS) \cdot \left(\underline{a}^* \underline{K_N}^{-1} \underline{a} \right) \text{Re} \left[\underline{a}^* \underline{K_N}^{-1} \underline{A} \underline{A} \underline{a} \right] \\
&+ \sigma_T^2 \left\{ \underline{a}^* \underline{A}^* \left[\underline{A}^* \underline{K_N}^{-1} + \underline{K_N}^{-1} \underline{A} \right] \underline{a} + \underline{a}^* \left[\underline{A}^* \underline{K_N}^{-1} + \underline{K_N}^{-1} \underline{A} \right] \underline{A} \underline{a} \right\} \quad (B-8)
\end{aligned}$$

Finally, substituting (B-8) into (B-7) yields the desired result -- equation (2-21) in chapter 2.

APPENDIX C

DERIVATION OF CLOSED FORM EXPRESSION FOR DOUBLE SUMMATION IN EQUATION (4-28)

The first double-summation in equation (4-28) is quickly evaluated

as,

$$\begin{aligned} \sum_{\ell=1}^{\frac{L}{2}} \sum_{p=\frac{L}{2}+1}^L (\ell - p) &= \frac{L}{2} \sum_{\ell=1}^{\frac{L}{2}} \ell - \frac{L}{2} \sum_{p=\frac{L}{2}+1}^L p \\ &= \frac{L}{2} \left\{ \sum_{\ell=1}^{\frac{L}{2}} \ell - \sum_{r=1}^{\frac{L}{2}} r + \frac{L}{2} \right\} \\ &= \frac{L}{2} \sum_{r=1}^{\frac{L}{2}} - \frac{L}{2} = -\frac{L}{8} \end{aligned} \quad (C-1)$$

A similar, but longer, process is followed for the second double summation in (4-28):

$$\begin{aligned} \sum_{\ell=1}^{\frac{L}{2}} \sum_{p=\frac{L}{2}+1}^L (\ell - p) \cos [(\ell - p)\Omega] &= \frac{1}{2} \sum_{\ell=1}^{\frac{L}{2}} \sum_{p=\frac{L}{2}+1}^L (\ell - p) \left\{ e^{j(\ell - p)\Omega} + e^{-j(\ell - p)\Omega} \right\} \\ &= \frac{1}{2} \sum_{\ell=1}^{\frac{L}{2}} \sum_{r=1}^{\frac{L}{2}} \left(\ell - r - \frac{L}{2} \right) \left[e^{+j(\ell - r - \frac{L}{2})\Omega} + e^{-j(\ell - r - \frac{L}{2})\Omega} \right] \\ &= \frac{1}{2} e^{-j\frac{L}{2}\Omega} \left\{ \sum_{\ell} \ell e^{+j\ell\Omega} \sum_r e^{-jr\Omega} - \sum_{\ell} e^{j\ell\Omega} \sum_r r e^{-jr\Omega} - \frac{L}{2} \sum_{\ell} e^{j\ell\Omega} \sum_r e^{-jr\Omega} \right\} \\ &\quad + \frac{1}{2} e^{+j\frac{L}{2}\Omega} \left\{ \sum_{\ell} \ell e^{-j\ell\Omega} \sum_r e^{+jr\Omega} - \sum_{\ell} e^{-j\ell\Omega} \sum_r r e^{+jr\Omega} - \frac{L}{2} \sum_{\ell} e^{-j\ell\Omega} \sum_r e^{+jr\Omega} \right\} \\ &= j \sin \frac{L}{2}\Omega \left[\sum_{\ell} \ell e^{-j\ell\Omega} \sum_r e^{+jr\Omega} - \sum_{\ell} e^{-j\ell\Omega} \sum_r r e^{+jr\Omega} \right] - \frac{L}{2} \cos \frac{L}{2}\Omega \\ &\quad \times \sum_{\ell} e^{j\ell\Omega} \sum_r e^{-jr\Omega} \end{aligned} \quad (C-2)$$

where all summation indices run from 1 to $\frac{L}{2}$.

Due to the equality

$$\sum_{\ell=1}^{\frac{L}{2}} \ell e^{j\ell\Omega} = -j \frac{\partial}{\partial \Omega} \sum_{\ell} e^{j\ell\Omega}, \quad (C-3)$$

there is only one unique summation in (C-2), for which the following identity applies:

$$\begin{aligned} \sum_{\ell} e^{j\ell\Omega} &= \frac{e^{j\Omega} - e^{j\left(\frac{L}{2}+1\right)\Omega}}{1 - e^{j\Omega}} = e^{j\left(\frac{L+2}{4}\right)\Omega} \frac{\sin\left(\frac{L}{2} \cdot \frac{\Omega}{2}\right)}{\sin \frac{\Omega}{2}} \\ &= C e^{j\left(\frac{L+2}{4}\right)\Omega} \end{aligned} \quad (C-4)$$

where we define,

$$C = \frac{\sin\left(\frac{L}{2} \cdot \frac{\Omega}{2}\right)}{\sin\left(\frac{\Omega}{2}\right)} \quad (C-5)$$

Substitution of (C-4) and (C-3) into the bracketed term in (C-2) yields,

$$\begin{aligned} &\left[\sum_{\ell} \ell e^{-j\ell\Omega} \sum_r e^{jr\Omega} - \sum_{\ell} e^{-j\ell\Omega} \sum_r r e^{jr\Omega} \right] = C \left[e^{j\left(\frac{L+2}{2}\right)\Omega} \left(j \frac{\partial C}{\partial \Omega} e^{-j\left(\frac{L+2}{2}\right)\Omega} \right. \right. \\ &\quad \left. \left. + \frac{L+2}{4} C e^{-j\left(\frac{L+2}{4}\right)\Omega} \right) - e^{-j\left(\frac{L+2}{4}\right)\Omega} \left(-j \frac{\partial C}{\partial \Omega} e^{+j\left(\frac{L+2}{4}\right)\Omega} + \left(\frac{L+2}{4}\right) C e^{+j\left(\frac{L+2}{4}\right)\Omega} \right) \right] \\ &= C \left[j \frac{\partial C}{\partial \Omega} + \left(\frac{L+2}{4}\right) C + j \frac{\partial C}{\partial \Omega} - \left(\frac{L+2}{4}\right) C \right] \\ &= 2 j C \frac{\partial C}{\partial \Omega} \end{aligned} \quad (C-6)$$

From (C-5), it is easy to obtain

$$\begin{aligned} \frac{\partial C}{\partial \Omega} &= \frac{\frac{L}{4} \cos\left(\frac{L}{2} \frac{\Omega}{2}\right) \sin\left(\frac{\Omega}{2}\right) - \frac{1}{2} \sin\left(\frac{L}{2} \frac{\Omega}{2}\right) \cos\left(\frac{\Omega}{2}\right)}{\sin^2\left(\frac{\Omega}{2}\right)} \\ &= \frac{1}{2} C \left[\frac{L}{2} \cot\left(\frac{L}{2} \frac{\Omega}{2}\right) - \cot\left(\frac{\Omega}{2}\right) \right] \end{aligned} \quad (C-7)$$

Substitution of (C-7), (C-6), (C-5), and (C-4) into (C-2) results in the following final, closed-form expression for the double summation:

$$\begin{aligned} \sum_{\ell=1}^{\frac{L}{2}} \sum_{p=\frac{L}{2}+1}^L (\ell-p) \left[\cos(\ell-p)\Omega \right] &= -C^2 \sin\left(\frac{L}{2} \Omega\right) \left[\frac{L}{2} \cot\left(\frac{L}{2} \frac{\Omega}{2}\right) - \cot\left(\frac{\Omega}{2}\right) \right] \\ &\quad - \frac{L}{2} C^2 \cos\left(\frac{L}{2} \Omega\right) \\ &= \frac{\sin^2\left(\frac{L}{2} \frac{\Omega}{2}\right)}{\sin^2\left(\frac{\Omega}{2}\right)} \left[\sin\left(\frac{L}{2} \Omega\right) \cot\left(\frac{\Omega}{2}\right) \right. \\ &\quad \left. - \frac{L}{2} \left(\sin\left(\frac{L}{2} \Omega\right) \cot\left(\frac{L}{2} \frac{\Omega}{2}\right) + \cos\left(\frac{L}{2} \Omega\right) \right) \right] \end{aligned} \quad (C-8)$$

APPENDIX D

NUMERICAL RESULTS FOR
EXTENDED SNR VALUES

This appendix presents the bearing estimation error results obtained for extensions of the baseline SNR to 0.5 and 2.0. The three standard deviation of error metrics appear in figures D.1 - D.7 and the two SBT bias error metrics appear in figures D.8 - D.14 as functions of the target-to-interference separation Y , where

$$Y = \left(\frac{2\pi}{T} \right) KK \left(\frac{d}{c} \right) \left(\cos \theta_T - \cos \theta_I \right),$$

θ_I = mean interference bearing,

θ_T = target bearing 90° ,

$T = 0.128$ seconds, $KK = 13$,

$d = 20$ feet, $c = 5000$ ft/sec,

$LL = 10$ hydrophones, $INR = 0.1$.

In figures D.1 - D.7 the following legend applies:

—————	CR Bound on the Standard Deviation of Error of Any Unbiased Bearing Estimator,
-----	Approximate Theoretical SBT Standard Deviation of Error,
$\left. \begin{array}{c} \triangle \\ \circ \end{array} \right\} \text{ and } \left. \begin{array}{c} \triangle \\ \circ \end{array} \right\}$	Simulated SBT Standard Deviation of Error and 90% Confidence Belts (20 replications per sample) for SNR = 0.5 and SNR = 2.0, respectively.

The solid line shown in the bias error results of figures D.8 - D.14 represents the approximate theoretical SBT bias metric while the simulated SBT bias results are depicted as above for the random errors.

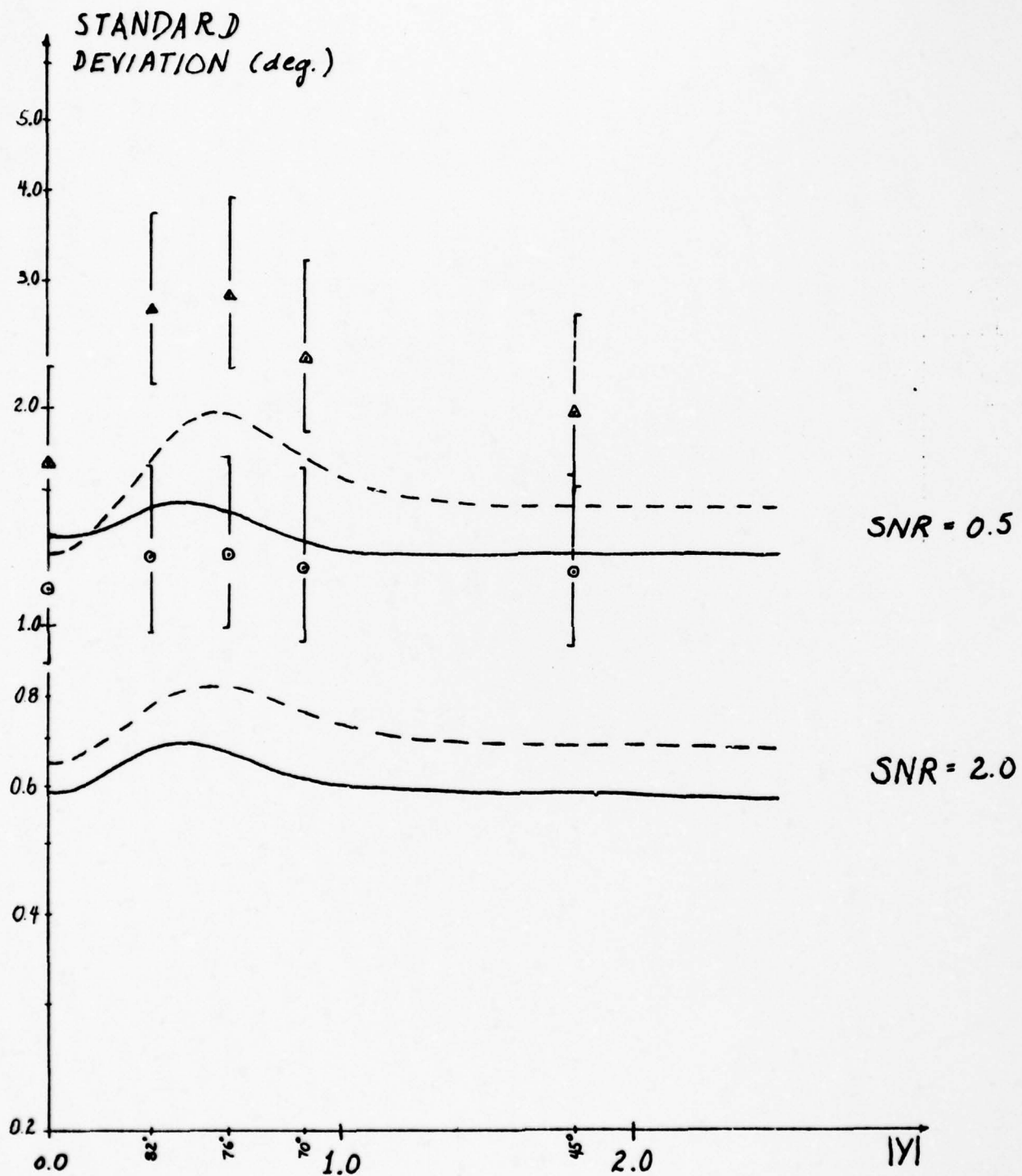


Figure D.1 - Standard Deviation of Error Results for Extended
SNR Values; MM = 1

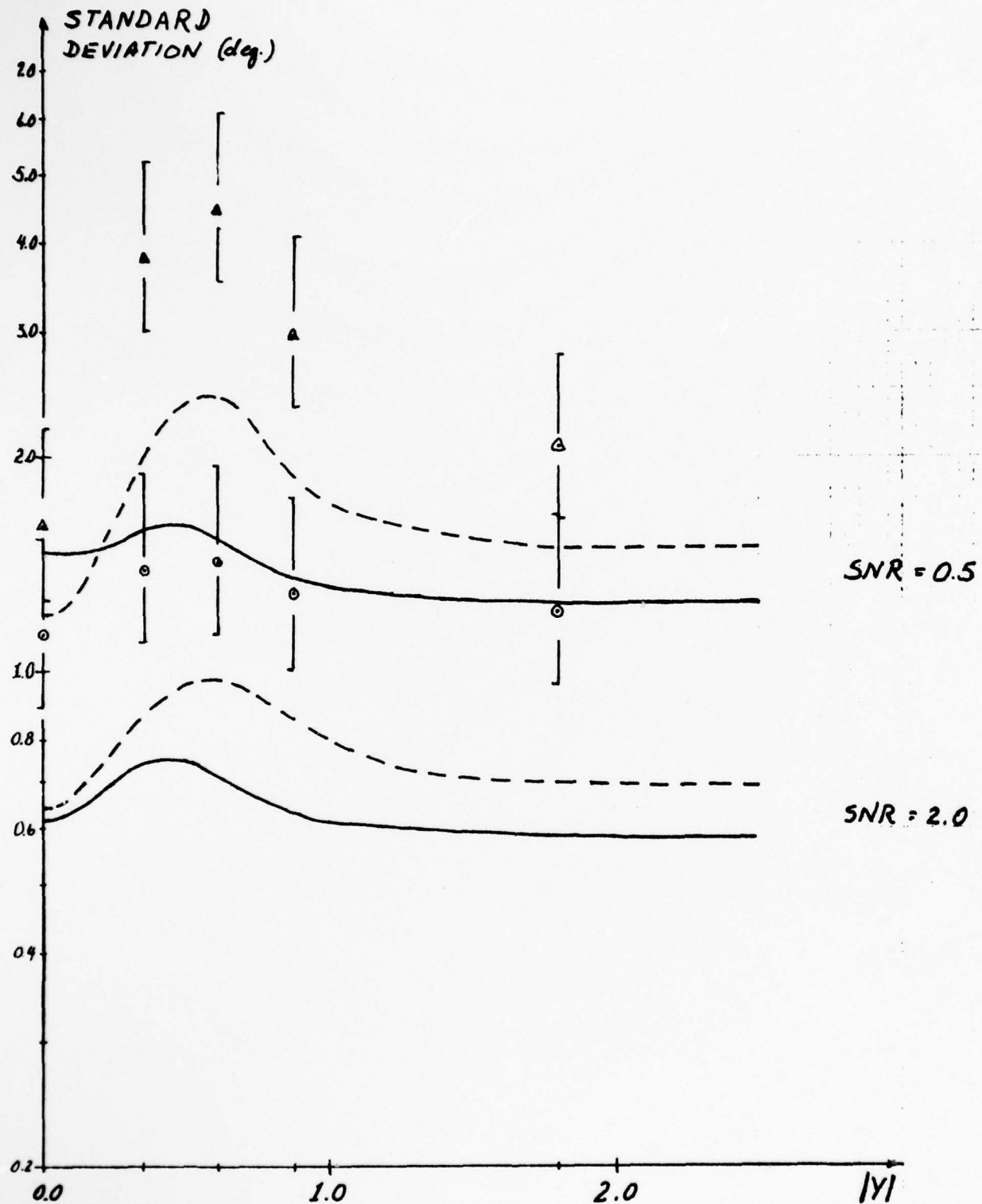


Figure D.2 - Standard Deviation of Error Results for Extended SNR Values; $MM = 2$, $\Delta\theta = 3^\circ$

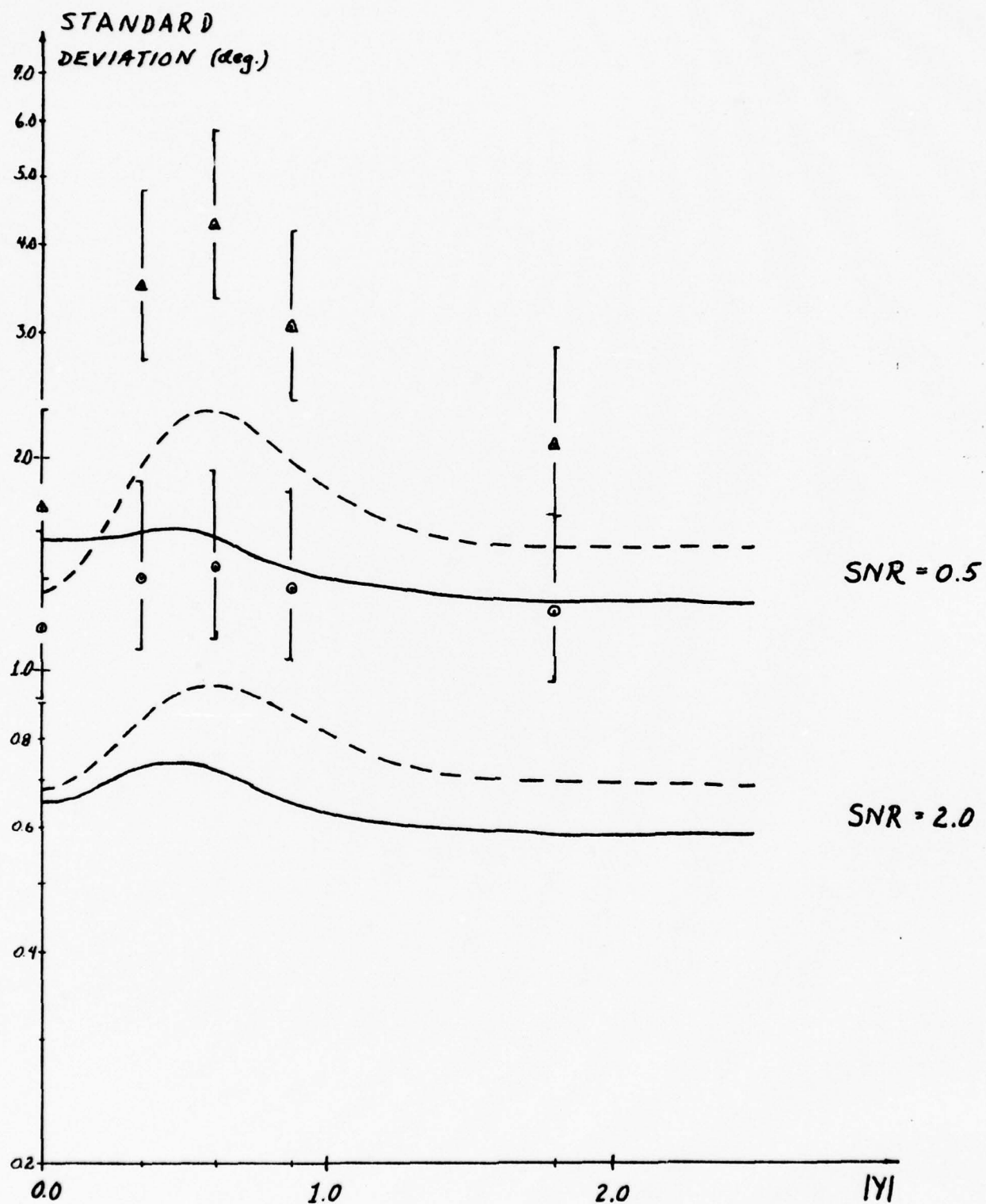


Figure D.3 - Standard Deviation of Error Results for Extended SNR Values; $MM = 2$, $\Delta\theta = 6^\circ$

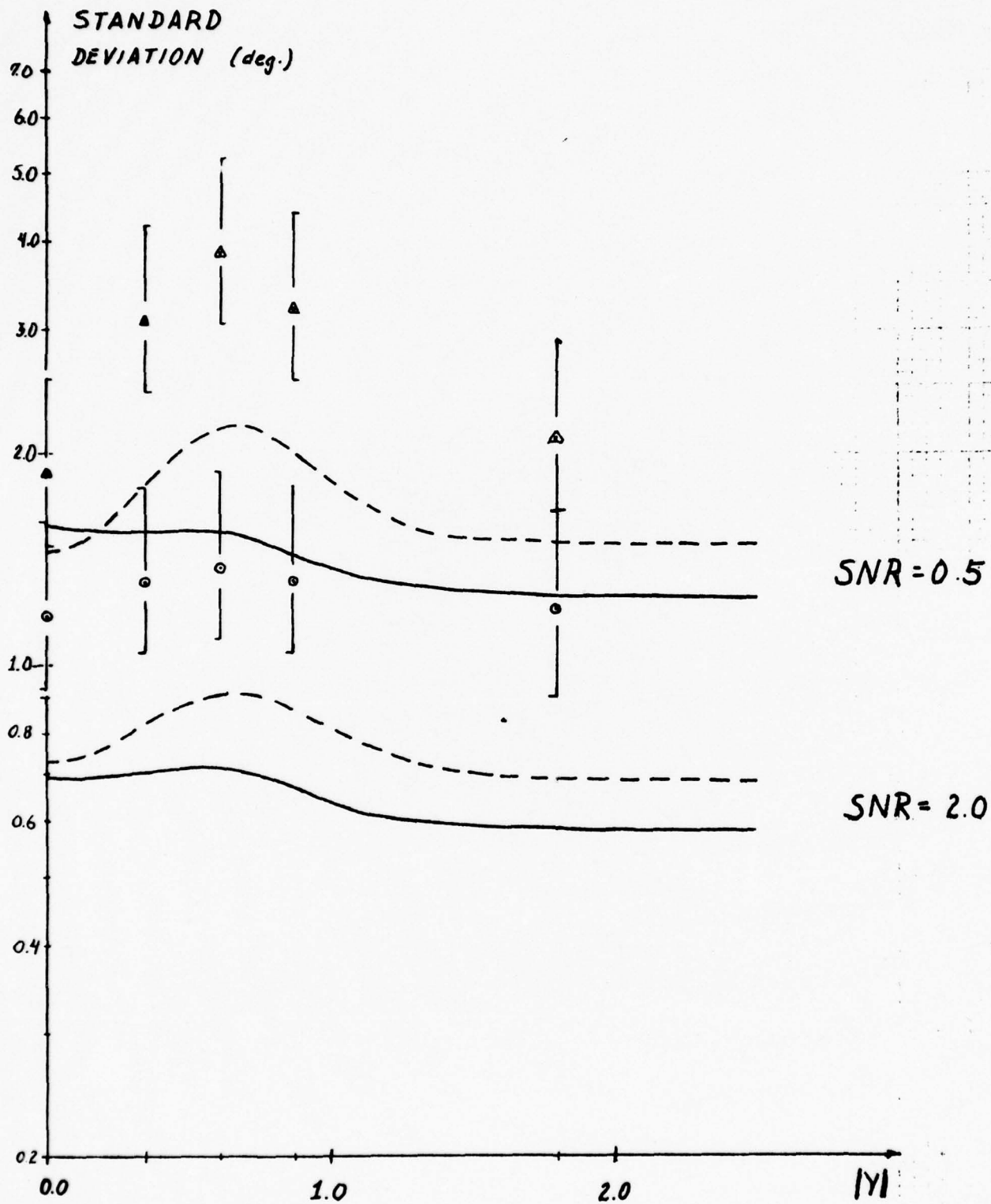


Figure D.4 - Standard Deviation of Error Results for Extended
SNR Values; $MM = 2$, $\Delta\theta = 9^\circ$

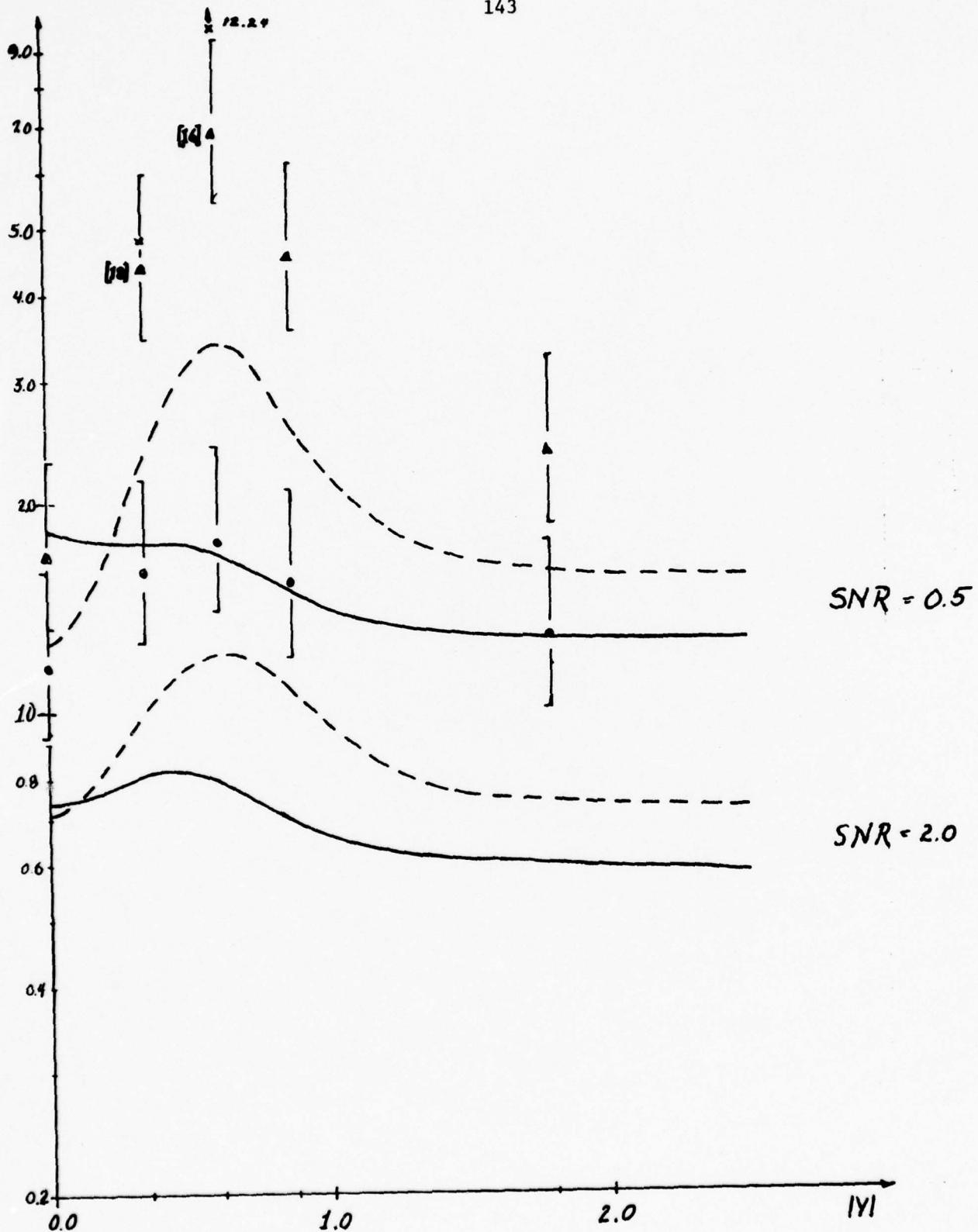


Figure D.5 - Standard Deviation of Error Results for Extended SNR Values; $MM = 4$, $\Delta\theta = 3^\circ$

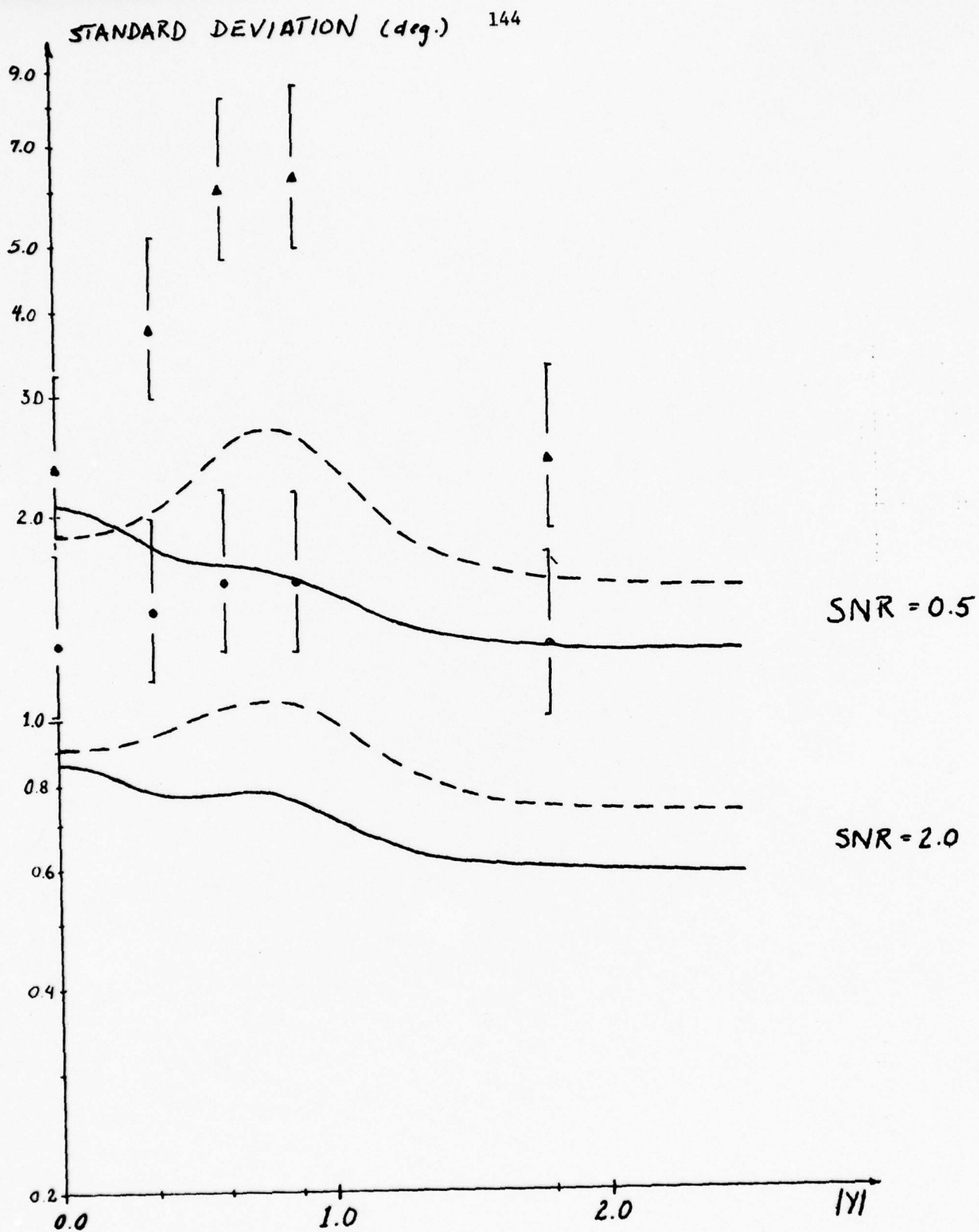


Figure D.6 - Standard Deviation of Error Results for Extended SNR Values; $MM = 4$, $\Delta\theta = 6^\circ$

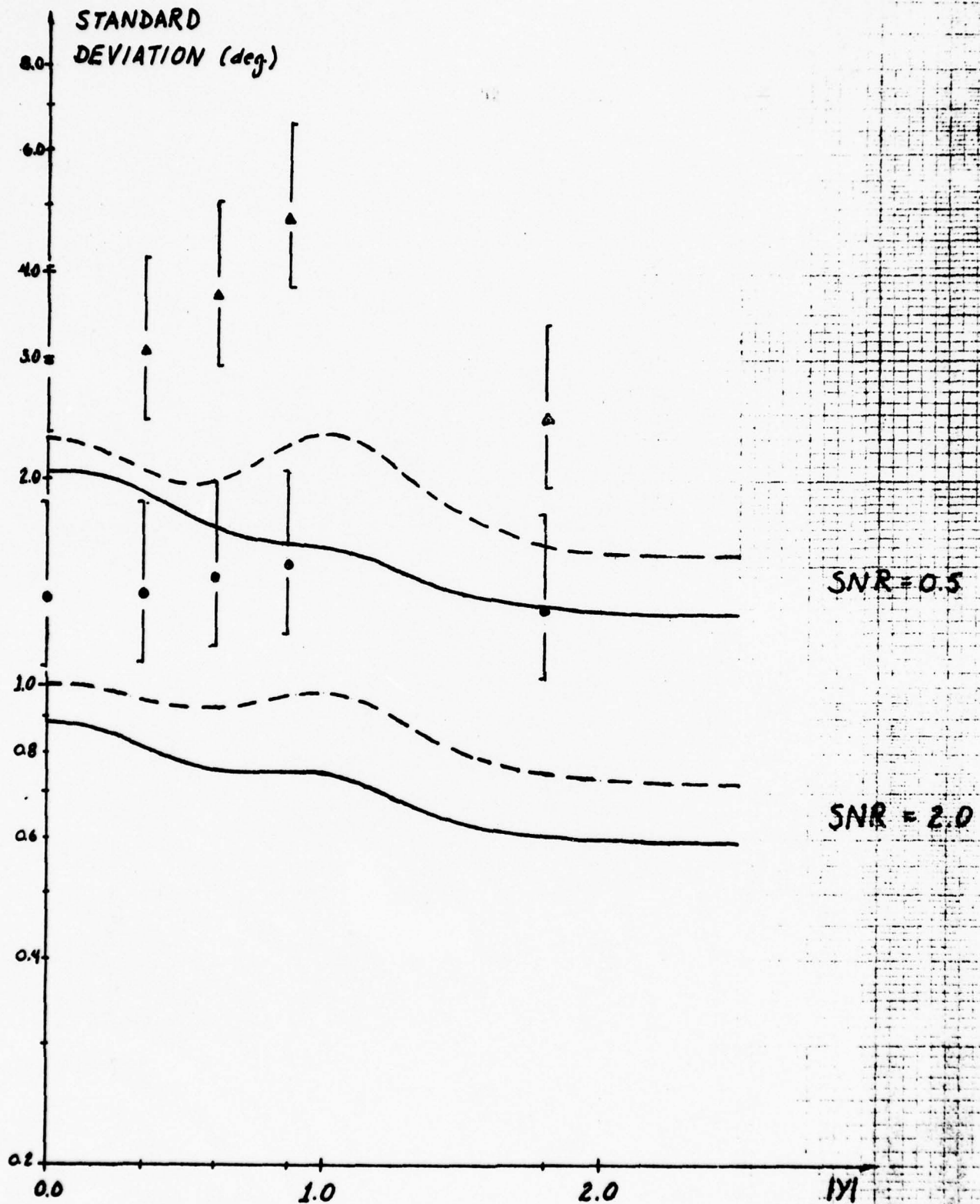
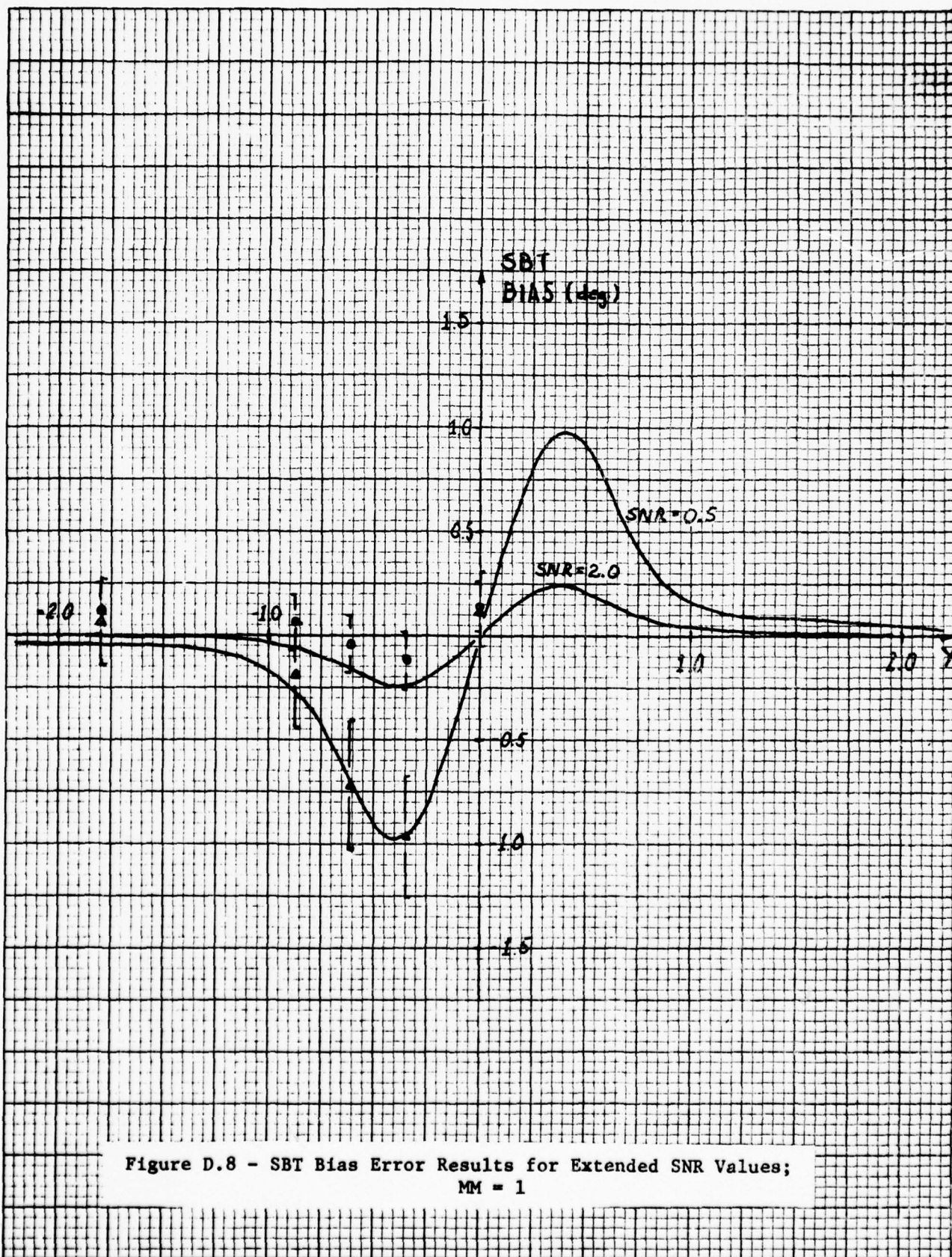
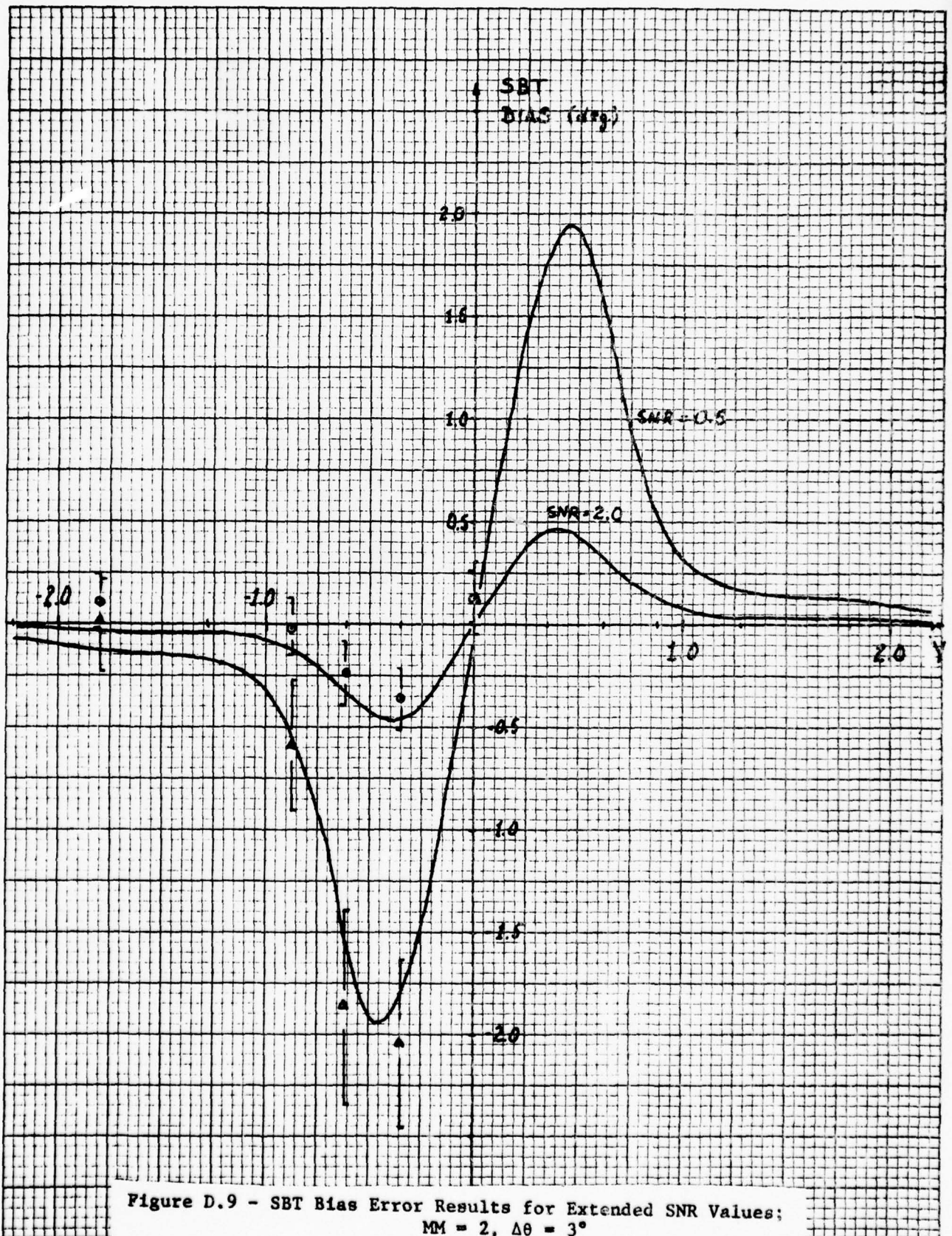
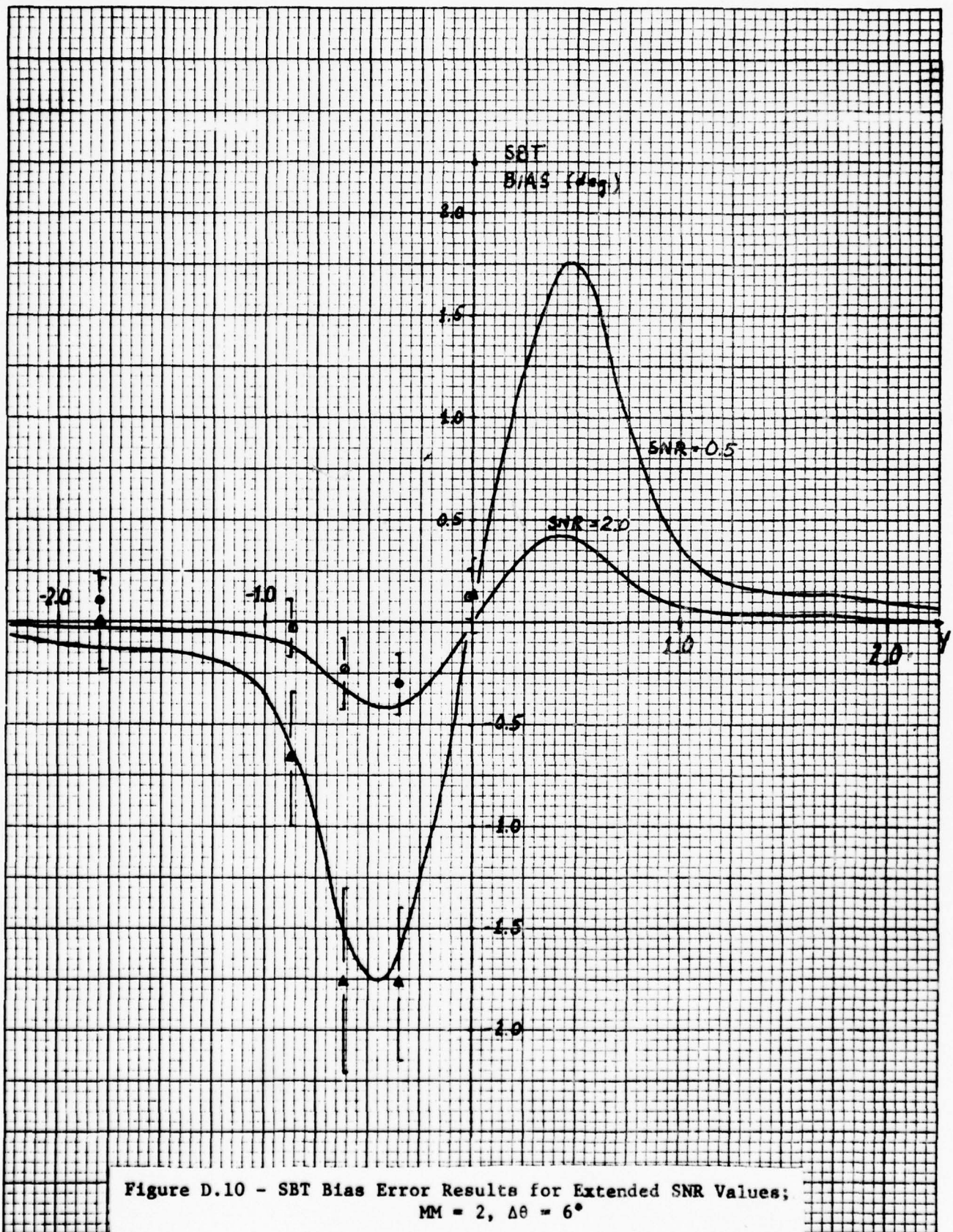
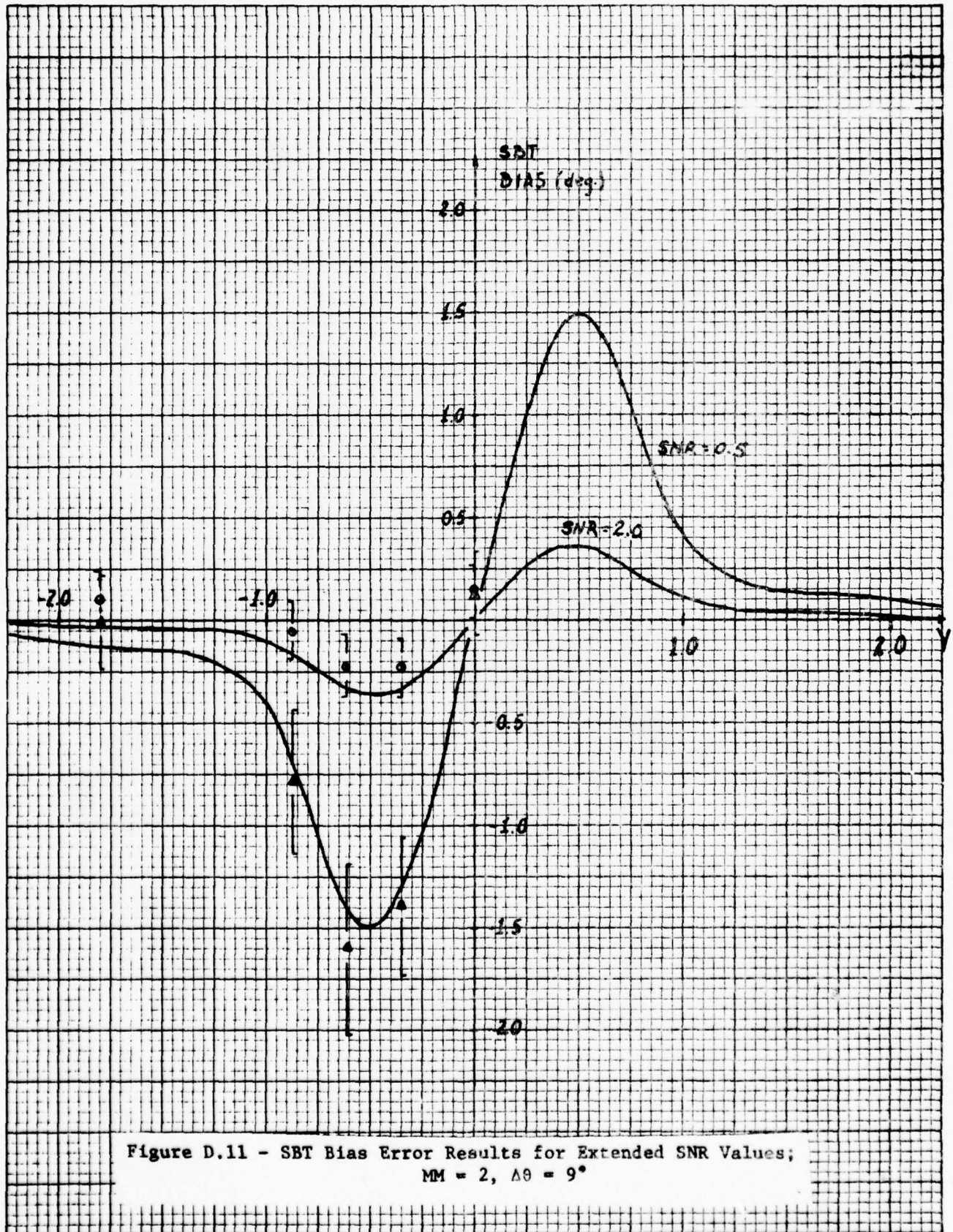


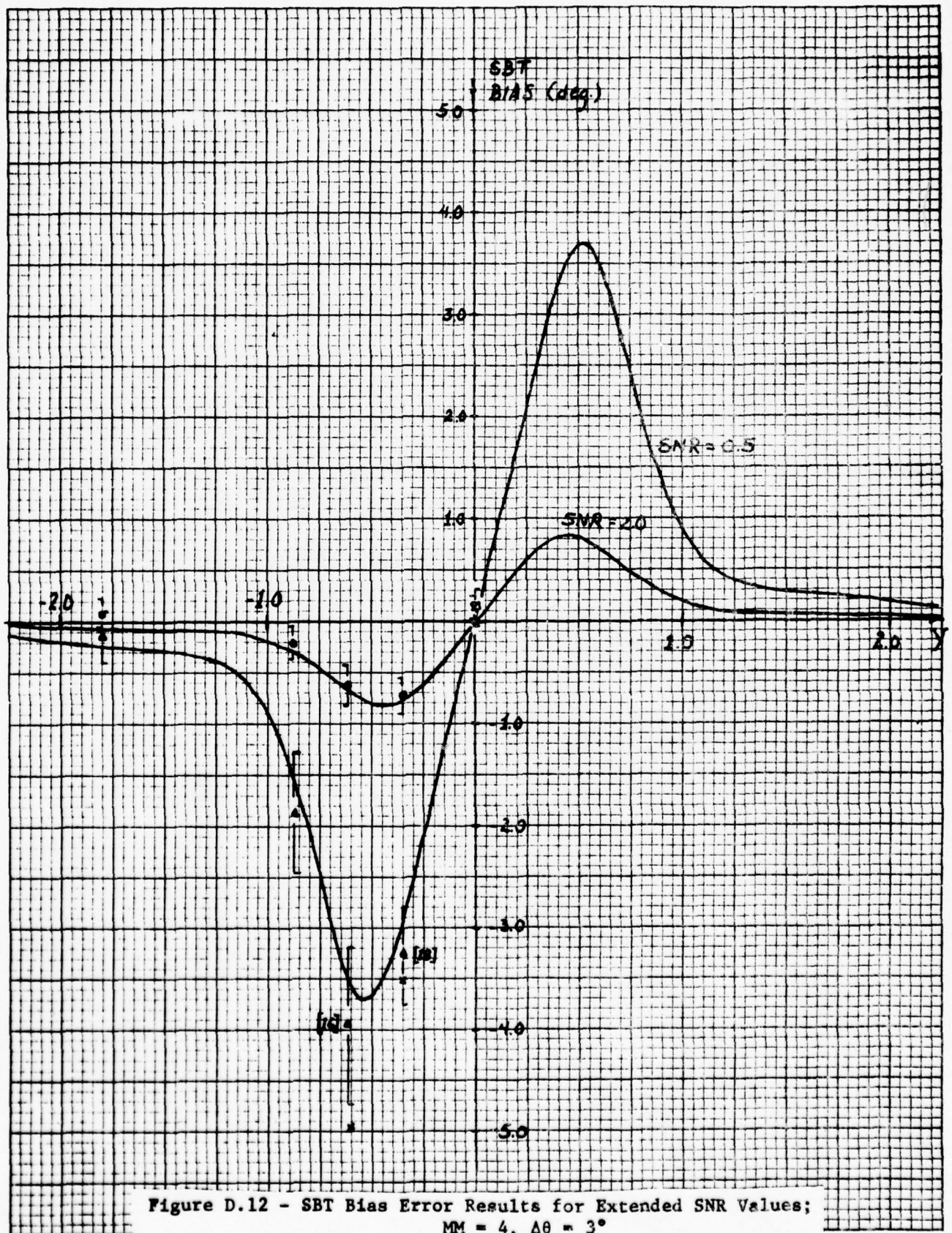
Figure D.7 - Standard Deviation of Error Results for Extended
SNR Values; MM = 4, $\Delta\theta = 9^\circ$

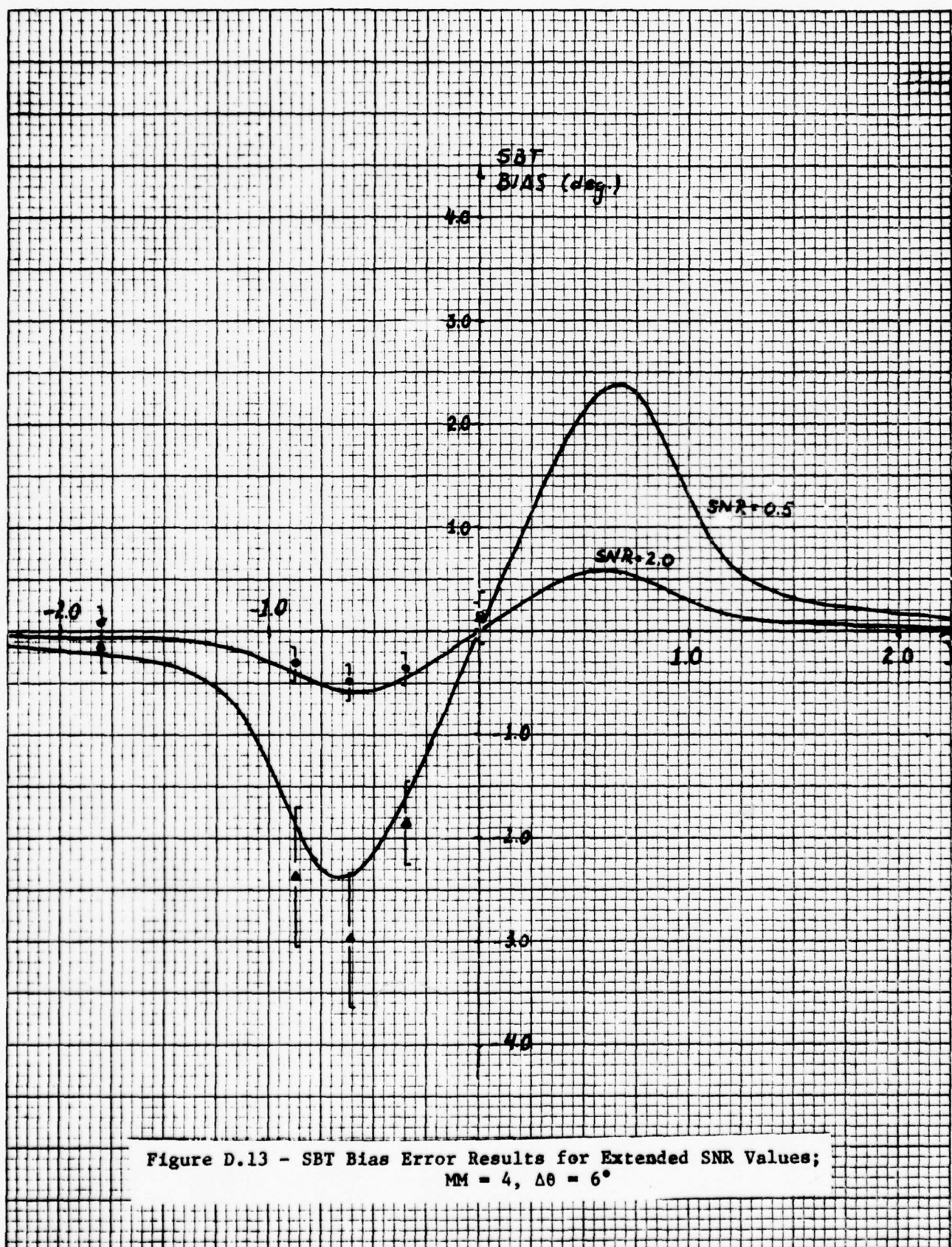


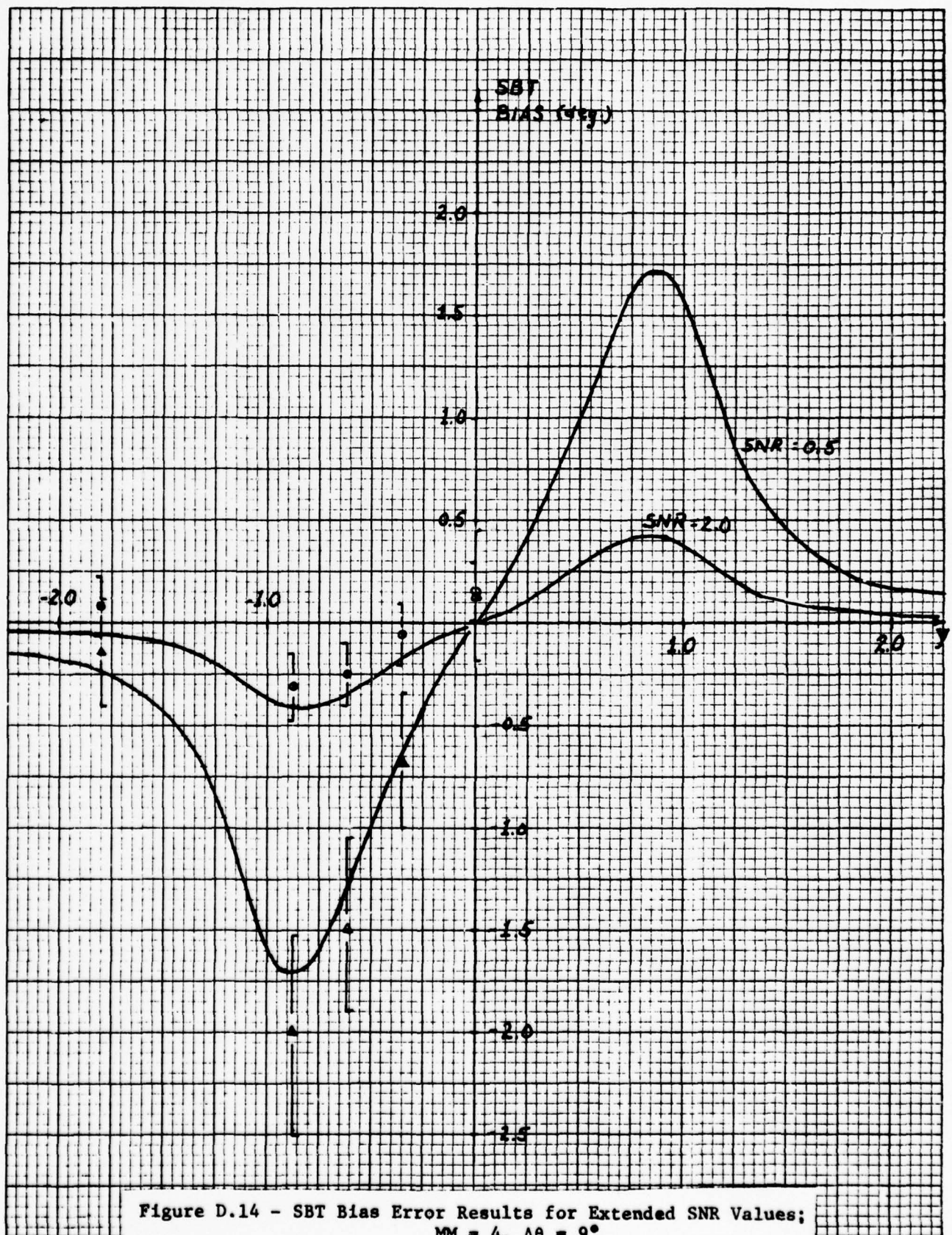












APPENDIX E

NUMERICAL RESULTS FOR
EXTENDED ARRAY SIZES

This appendix presents the bearing estimation error results obtained for extensions of the baseline array size (LL) to 20 and 40 hydrophones. The three standard deviation of error metrics appear in figures E.1 - E.5 and the two SBT bias error metrics appear in figures E.6 - E.10. The appropriate baseline values of the metrics are repeated in figures E.1 - E.10 for comparison. The random and bias errors are presented as functions of the target-to-interference separation, Y , where

$$Y = \left(\frac{2\pi}{T} \right) KK \left(\frac{d}{c} \right) (\cos \theta_T - \theta_I),$$

θ_I = mean interference bearing,

θ_T = target bearing = 90°

T = 0.128 seconds, KK = 13,

d = 20 feet, c = 5000 ft/second

SNR = 1.0, INR = 0.1 .

In figures E.1 - E.5 the following legend applies:

- _____ CR Bound on the Standard Deviation of Error of
Any Unbiased Bearing Estimator,
- Approximate Theoretical SBT Standard Deviation of
Error,
- $\left[\begin{array}{c} \Delta \\ \Delta \end{array} \right]$ Simulated SBT Standard Deviation of Error and
90% Confidence Belts for LL = 10, 20, and 40
hydrophones, respectively. For figures E.1 - E.10
the SBT simulation sample sizes are:

<u>CONFIGURATION</u>	<u>SAMPLE SIZE</u>
LL = 10, MM = 1	60
LL = 10, MM = 2, 4	40
LL = 20, 40	20

The solid line shown in the bias error results of figures E.6 - E.10 represents the approximate theoretical SBT bias metric while the simulated SBT bias results are depicted as above for the random errors.

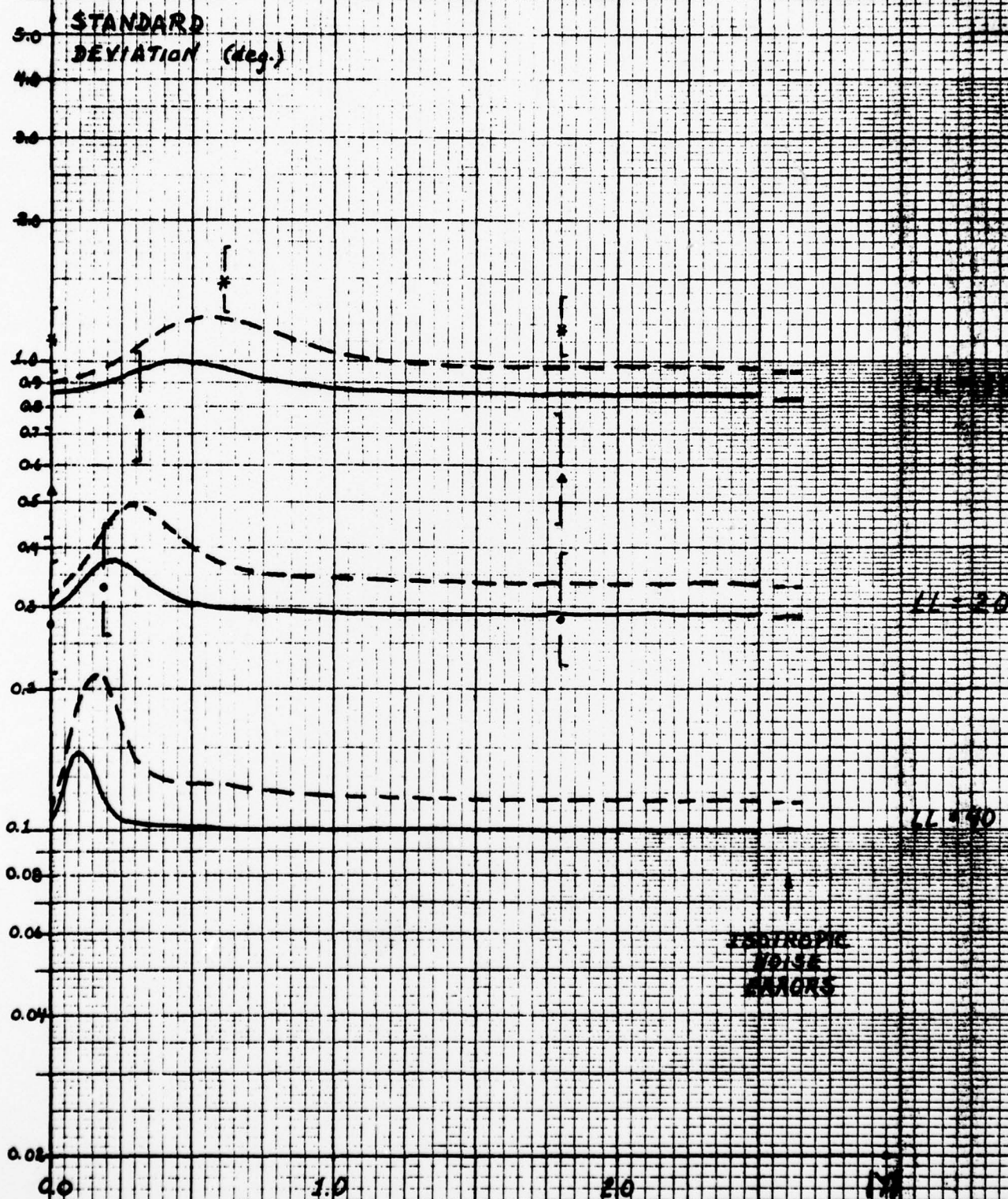
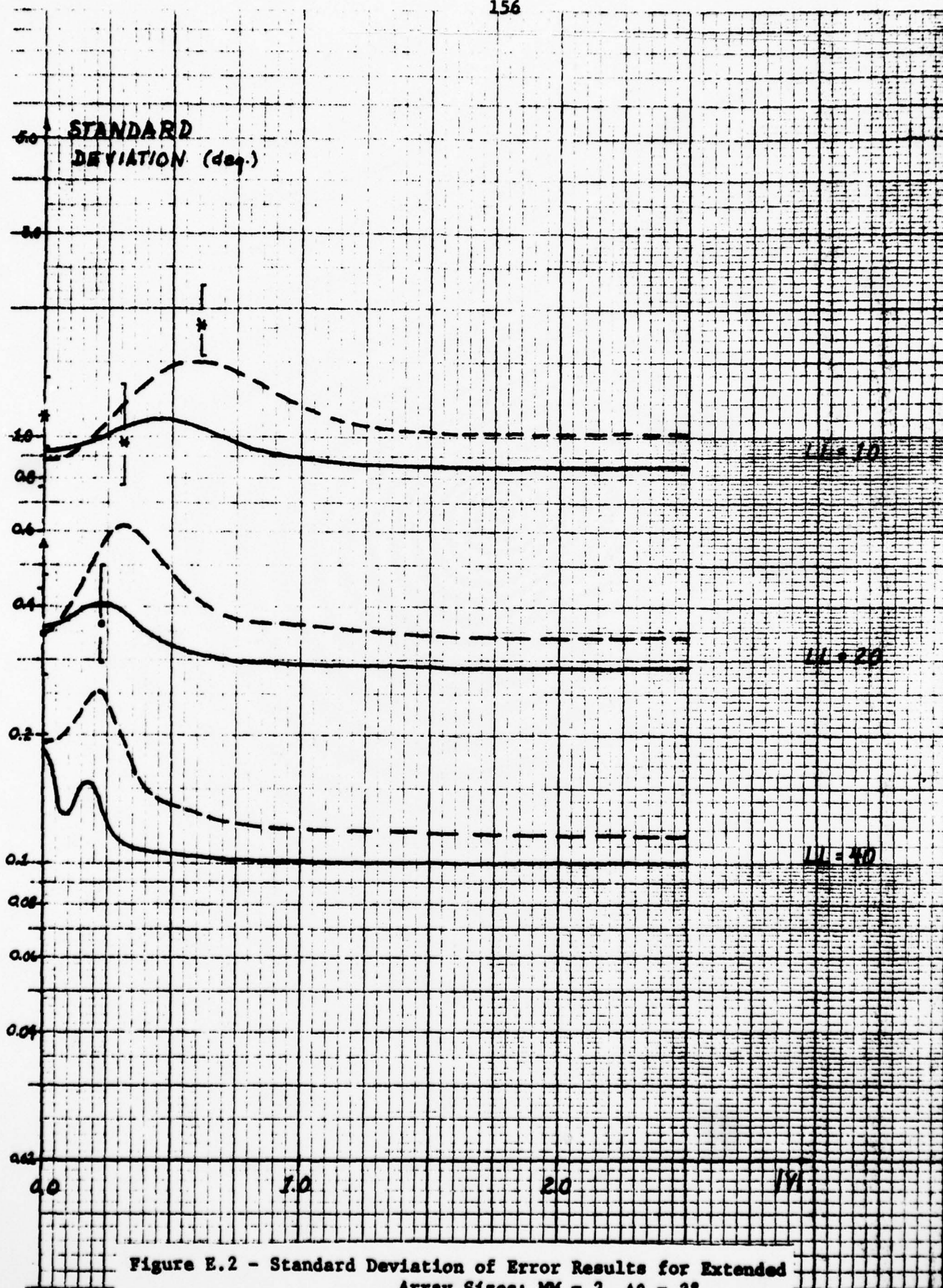


Figure E.1 - Standard Deviation of Error Results for Extended Array Sizes; MM = 1



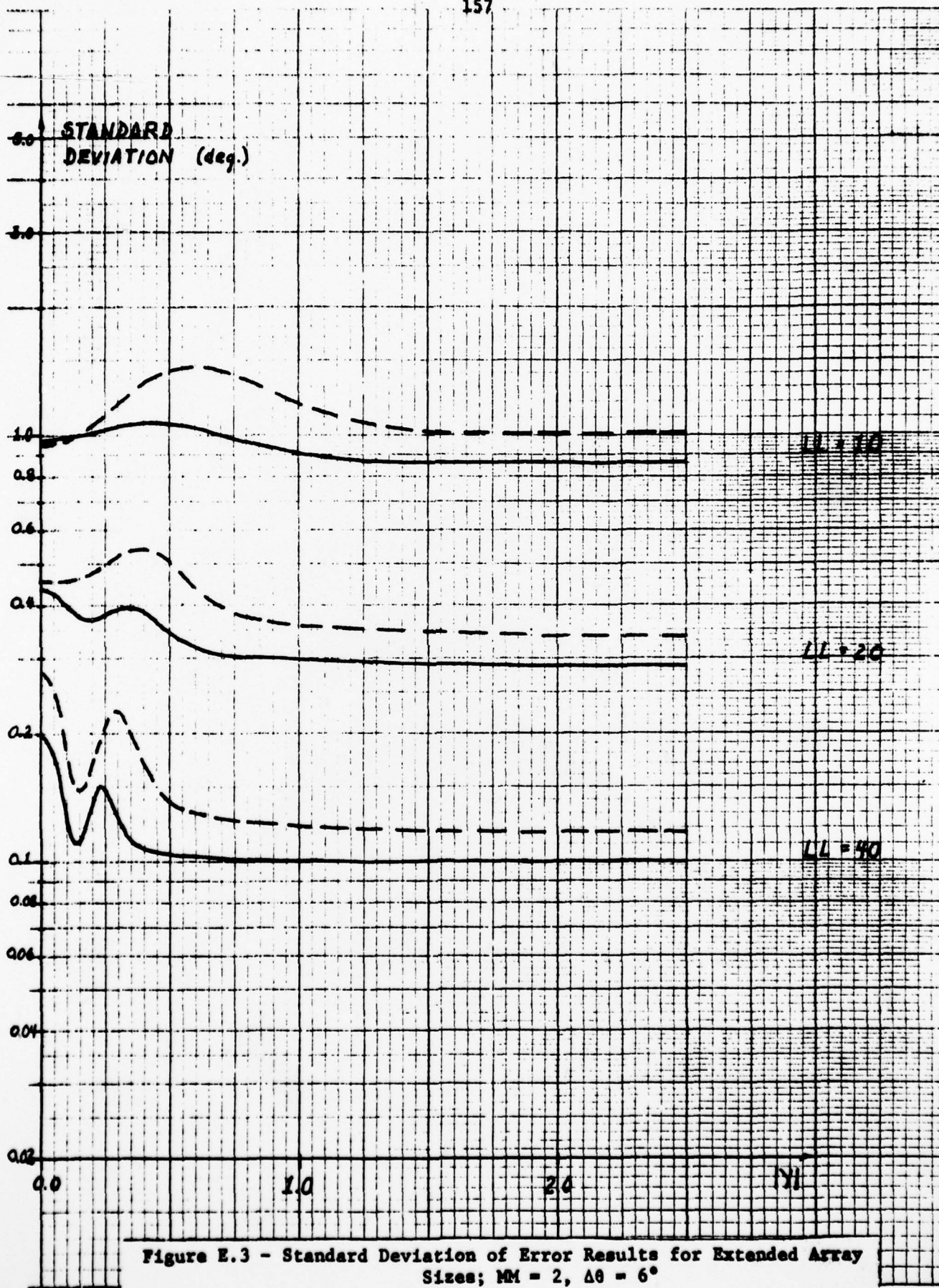


Figure E.3 - Standard Deviation of Error Results for Extended Array Sizes; MM = 2, $\Delta\theta = 6^\circ$

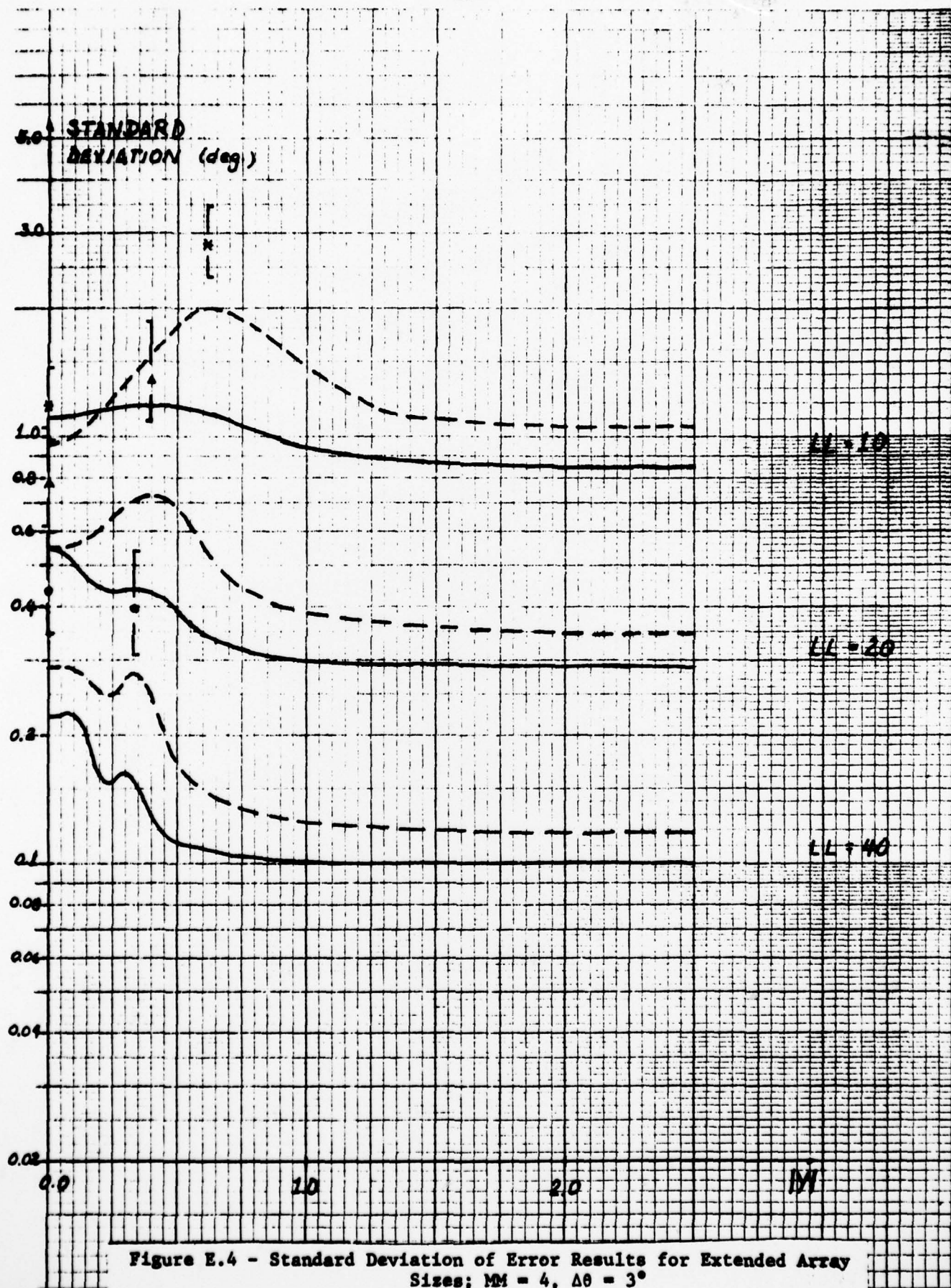
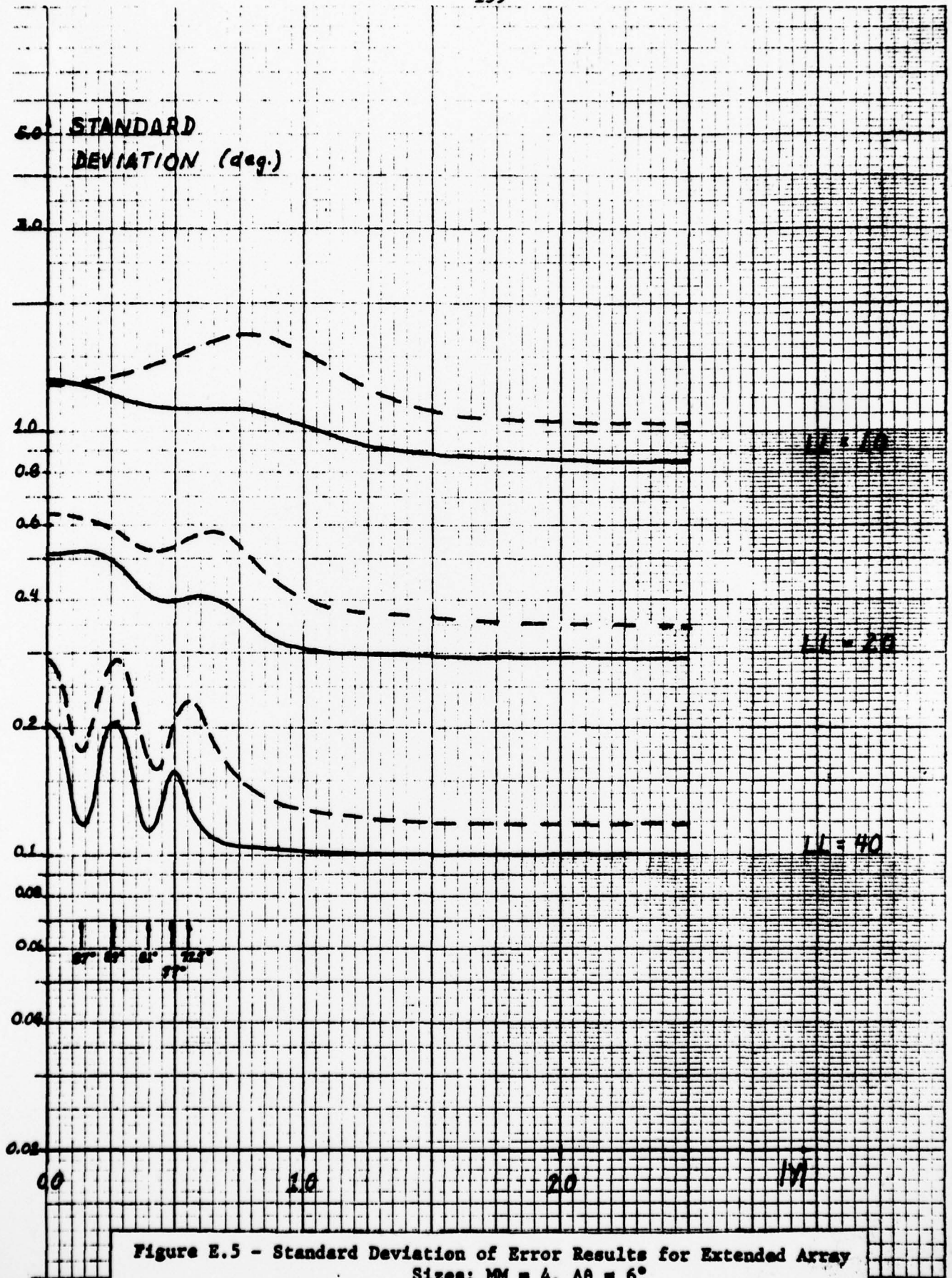
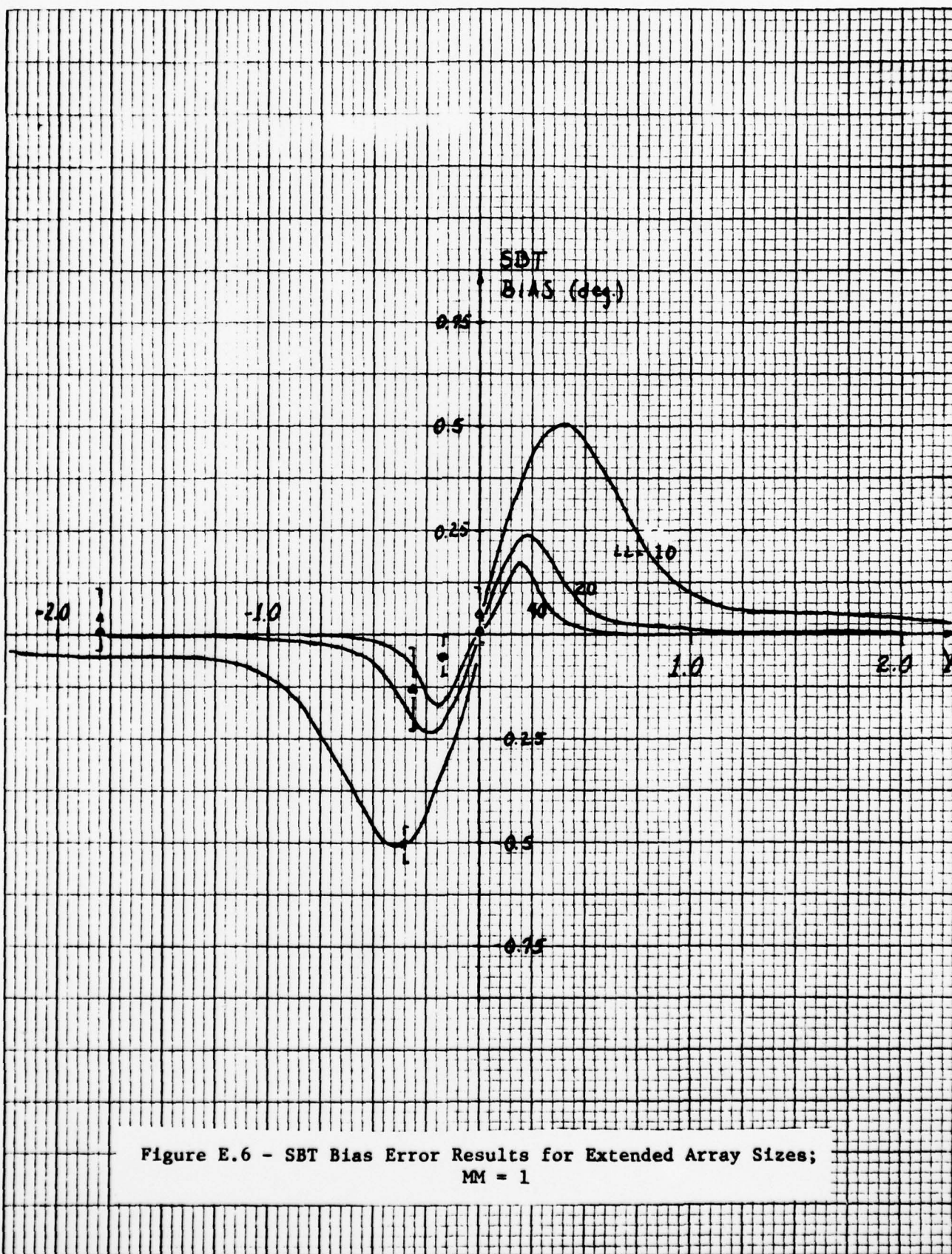
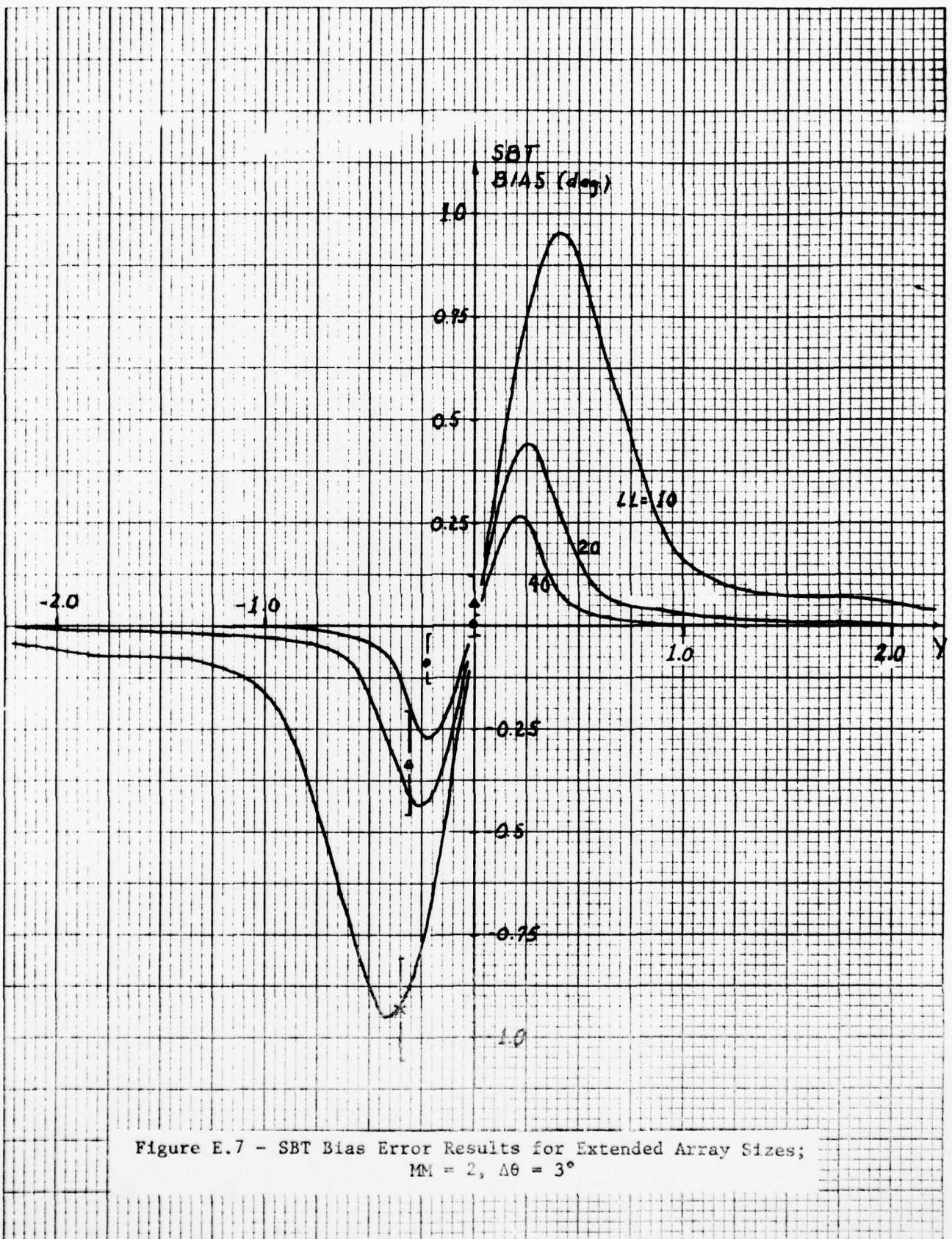
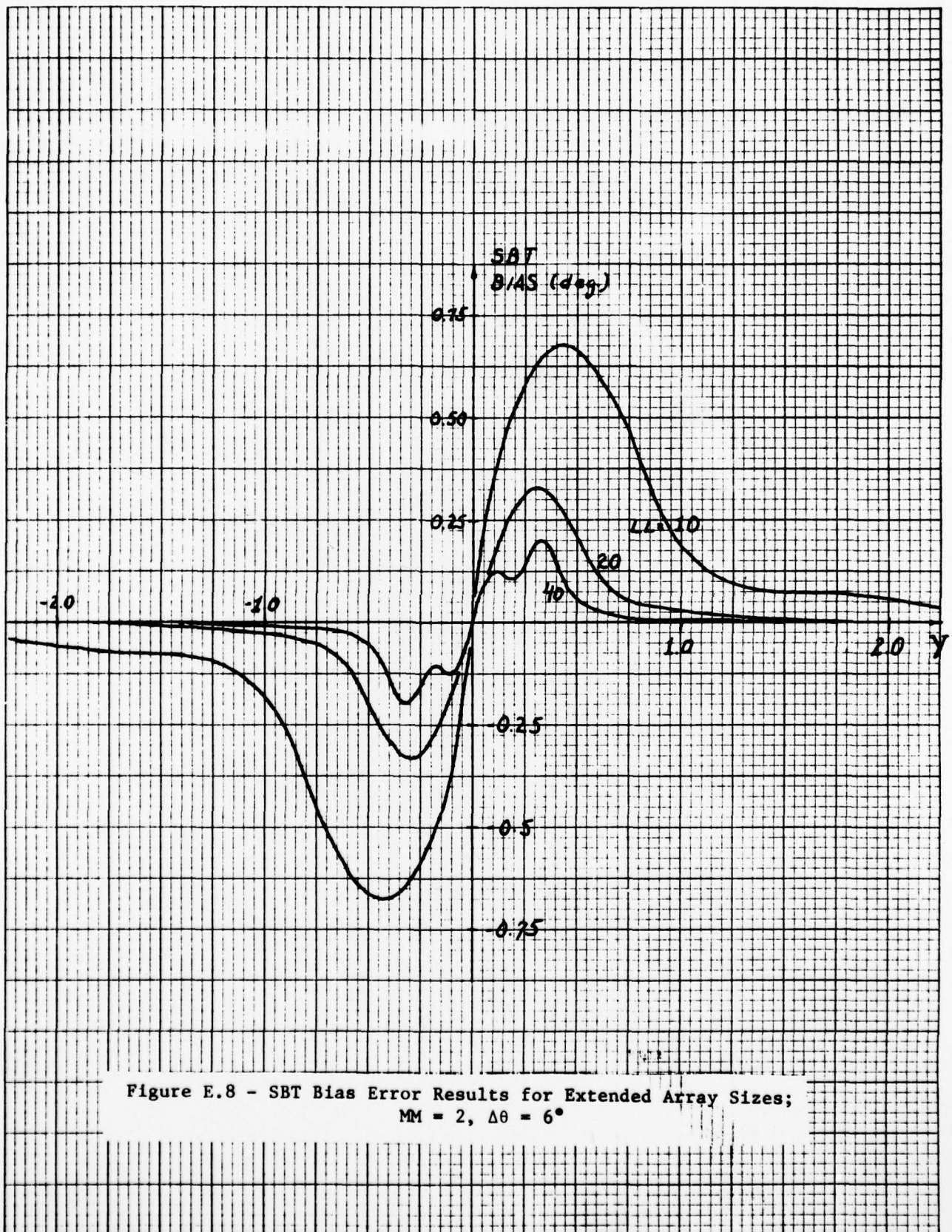


Figure E.4 - Standard Deviation of Error Results for Extended Array Sizes; $MM = 4$, $\Delta\theta = 3^\circ$









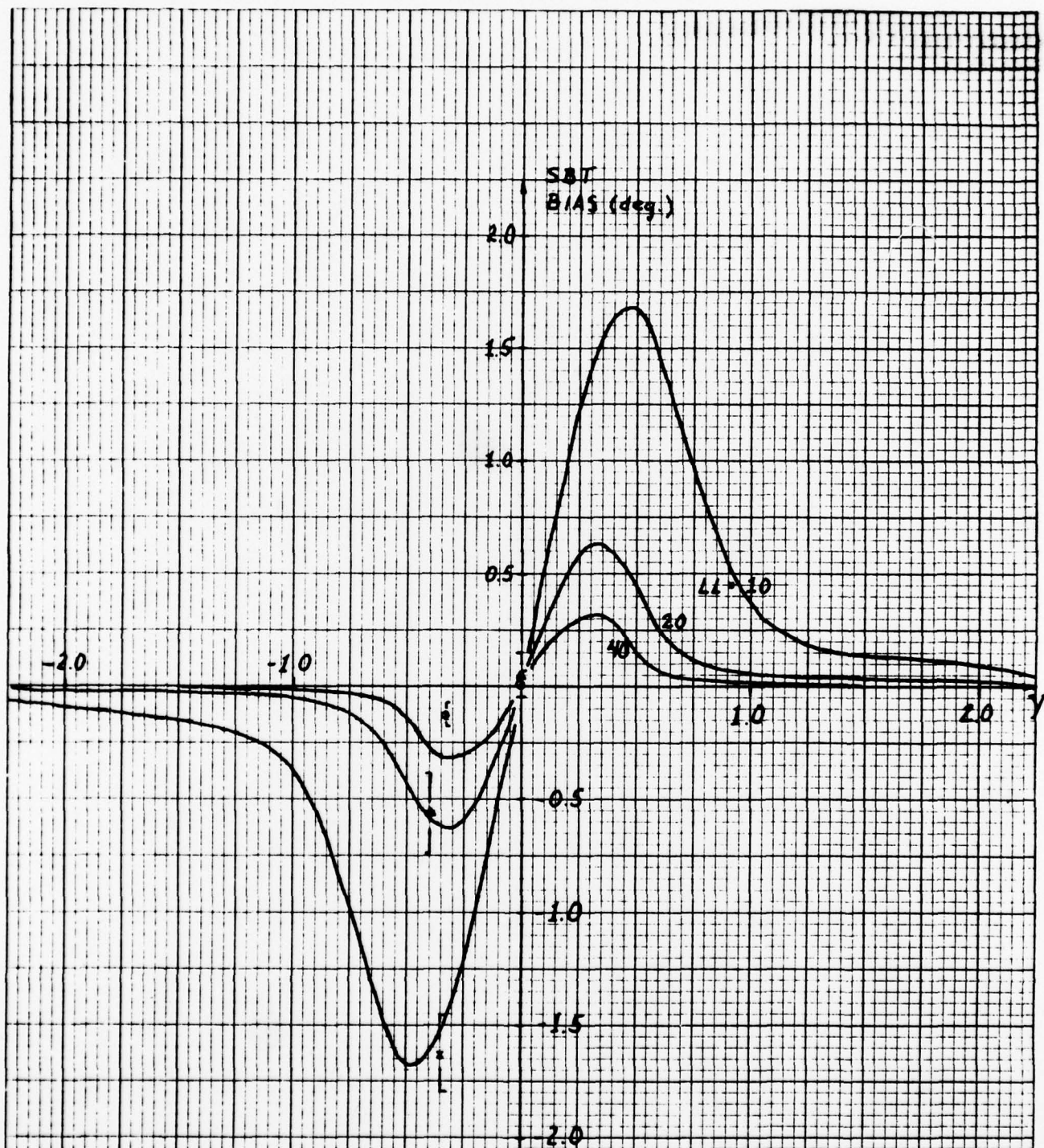
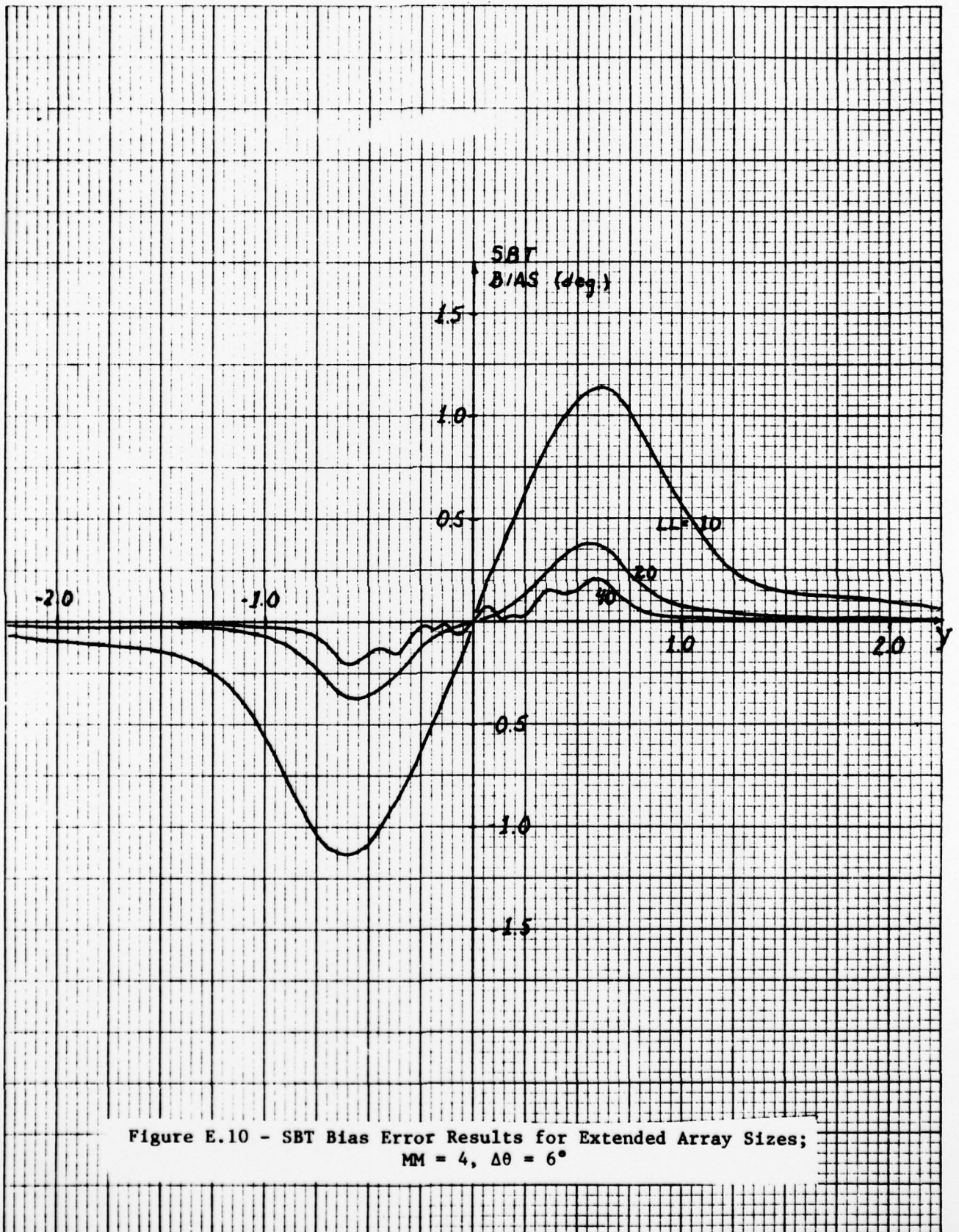


Figure E.9 - SBT Bias Error Results for Extended Array Sizes;
 $MM = 4, \Delta\theta = 3^\circ$



REFERENCES

1. V. C. Anderson, P. Rudnick, "Rejection of a Coherent Arrival at an Array," *Journal of the Acoustical Society of America*, Vol. 45 (2), pp. 406-410, 1969.
2. W. Bangs, "Array Processing with Generalized Beam-Formers," Ph.D. Dissertation, Yale University, 1971.
3. J. S. Bendat, A. G. Piersol, Random Data: Analysis and Measurement Procedures, Wiley-Interscience, New York, N. Y., 1971.
4. L. E. Brennan, J. D. Mallett, "Efficient Simulation of External Noise Incident on Arrays," *IEEE Transaction on Antennas and Propagation*, Vol. AP-24 (5), pp. 470-741, September 1976.
5. G. C. Carter, "Time Delay Estimation," NUSC TR 5335, Naval Underwater Systems Center, New London, Connecticut, April 1976.
6. H. Cox, "Interrelated Problems in Estimation and Detection I and II," *Proc. NATO Advanced Study Institute on Signal Processing with Emphasis on Underwater Acoustics*, Enschede, The Netherlands, August 1968.
7. H. Cox, "Resolving Power and Sensitivity to Mismatch of Optimum Array Processors," *Journal of the Acoustical Society of America*, Vol. 54 (3), pp. 771-785, 1973.
8. W. J. Dixon, F. J. Massey, Jr., Introduction to Statistical Analysis, McGraw-Hill, New York, N. Y., 1957.
9. I. N. El-Behery, R. H. MacPhie, "Maximum-Likelihood Estimation of Source Parameters from Time-Sampled Outputs of a Linear Array," *Journal of the Acoustical Society of America*, Vol. 62 (1), pp. 125-134, 1977.
10. J. N. Franklin, Matrix Theory, Prentice-Hall, Englewood Cliffs, N. J., 1968.
11. L. J. Griffiths, "A Simple Adaptive Algorithm for Real-Time Processing in Antenna Arrays," *Proceedings of the IEEE*, Vol. 57 (10), pp. 1696-1704, October 1969.
12. W. R. Hahn, "Optimum Signal Processing for Passive Sonar Range and Bearing Estimation," *Journal of the Acoustical Society of America*, Vol. 58 (1), pp. 201-207, 1975.

13. W. R. Hahn, "Optimum Estimation of a Delay Vector Caused by a Random Field Propagating Across an Array of Noisy Sensors," Naval Ordnance Laboratory, AD-751555, White Oak, Maryland, June 1972.
14. E. M. Hofstetter, D. F. Delong, Jr., "Detection and Parameter Estimation in an Amplitude Comparison Monopulse Radar," IEEE Transactions on Information Theory, Vol. IT-15 (1), pp. 22-30, January 1969.
15. M. J. Jacobson, "Space-Time Correlation in Spherical and Circular Noise Fields," Journal of the Acoustical Society of America, Vol. 34, pp. 971-978, 1962.
16. E. G. Kelliher, "An Adaptive Linear MMSE Matrix Filter Algorithm Using Updated Incorrect A-Prior Signal Knowledge," Ph.D. Dissertation, Catholic University, 1972.
17. T. Kooij, "Adaptive Array Processors for Sensitivity Constrained Optimization," Ph.D. Dissertation, Catholic University, 1977.
18. V. MacDonald, "Optimum Bearing Estimation with Passive Sonar Systems," Ph.D. Dissertation, Yale University, 1971.
19. V. MacDonald, P. M. Schultheiss, "Optimum Passive Bearing Estimation In a Spatially Incoherent Noise Environment," Journal of the Acoustical Society of America, Vol. 46 (1), pp. 37-43, 1969.
20. T. P. McGarty, "Azimuth-Elevation Estimation Performance of a Spatially Dispersive Channel," IEEE Transactions on Aerospace and Electronics Systems, Vol. AES-10 (1), pp. 58-69, January 1974.
21. T. P. McGarty, "The Effect of Interfering Signals on the Performance of Angle of Arrival Estimates," IEEE Transactions on Aerospace and Electronic Systems, Vol. AES-10 (1), pp. 70-77, January 1974.
22. L. E. Miller, "Signal Detection and Bearing Estimation Capabilities of Multiplicative Array Processors," Ph.D. Dissertation, Catholic University, 1973.
23. T. H. Naylor, J. L. Balintfy, B. S. Burdick, K. Chu, Computer Simulation Techniques, John Wiley & Sons, New York, N. Y., 1966.
24. A. V. Oppenheim, R. W. Schaffer, Digital Signal Processing, Prentice-Hall, Englewood Cliffs, New Jersey, 1975.
25. L. L. Scharf, P. H. Moose, "Information Measures and Performance Bounds for Array Processors," IEEE Transactions on Information Theory, Vol. IT-22 (1), pp. 11-21, January 1976.

26. P. M. Schultheiss, "Passive Sonar Detection in the Presence of Interference," *Journal of the Acoustical Society of America*, Vol. 43 (3), pp. 418-425, 1968.
27. L. P. Seidman, "Bearing Estimation Error with a Linear Array," *IEEE Transactions on Audio and Electroacoustics*, Vol. AU-19 (2), pp. 147-157, June 1971.
28. P. Swerling, "Maximum Angular Accuracy of a Pulsed Search Radar," *Proceedings of the Institute of Radio Engineers*, pp. 1145-1155, September 1956.
29. J. B. Thomas, T. R. Williams, "On the Detection of Signals in Nonstationary Noise by Product Arrays," *Journal of the Acoustical Society of America*, Vol. 31 (4), pp. 453-462, April 1959.
30. W. F. Trench, "An Algorithm for the Inversion of Finite Toeplitz Matrices," *Journal of the Society of Industrial and Applied Mathematics*, Vol. 12 (3), pp. 515-522, September 1964.
31. H. Urkowitz, "The Accuracy of Maximum Likelihood Angle Estimates in Radar and Sonar," *IEEE Transactions on Military Electronics*, Vol. MIL-8 (1), pp. 39-45, January 1964.
32. H. L. Van Trees, "A Unified Theory for Optimum Array Processing," Report No. 4160866, A. D. Little, Inc., August 1966.
33. H. L. Van Trees, Detection, Estimation and Modulation Theory, Part 1, John Wiley & Sons, New York, N. Y., 1968.
34. H. L. Van Trees, Detection, Estimation and Modulation Theory, Part 3, John Wiley & Sons, New York, N. Y., 1971.
35. B. Widrow, P. E. Mantey, L. J. Griffiths, B. B. Goode, "Adaptive Antenna Systems," *Proceedings of the IEEE*, Vol. 55 (12), pp. 2145-2159, December 1967.
36. J. Witt, "An Investigation of the Bearing Accuracy of Two Passive Multi-Channel Array Algorithms in the Presence of Correlated Noise," Ph.D. Dissertation, Catholic University, 1977.